

## ABSTRACT

Title of Dissertation: **ADVANCED REACTION ENGINEERING FOR THE NONOXIDATIVE VALORIZATION OF METHANE**

Sichao Cheng, Doctor of Philosophy, 2023

Dissertation directed by: Professor Dongxia Liu  
Department of Chemical and Biomolecular Engineering

Non-oxidative methane conversion (NMC) represents a promising pathway that directly transforms methane into higher hydrocarbons such as ethane, ethylene, acetylene, aromatics, and hydrogen in a single-step synthesis. This process holds particular appeal due to its potential for remote operation and its status as a carbon-neutral process, given that it does not produce carbon dioxide in the product effluent. As such, NMC could serve as a viable alternative to existing multi-step, energy-intensive processes like the Fischer-Tropsch synthesis and liquid petroleum gas production. Despite its potential, NMC faces significant challenges. The thermodynamic stability of methane, attributed to its strong C-H bonds, poses a considerable obstacle. Other challenges include low selectivity towards desired products, rapid catalyst deactivation, and kinetic hindrance, all of which complicate the process. As of now, these challenges have prevented the development of a commercially viable NMC process.

This dissertation aims at overcoming these hurdles to unlock the full potential of NMC, paving the way for a more efficient and sustainable method of methane conversion from the

perspective of both catalyst design and reaction engineering. The impact of hydrogen activation on NMC using a hydrogen-permeable  $\text{SrCe}_{0.8}\text{Zr}_{0.2}\text{O}_{3-\delta}$  (SCZO) perovskite oxide material over the iron/silica catalyst was explored. The SCZO oxide, with its mixed ionic and electronic conductivity, facilitates  $\text{H}_2$  activation into protons and electrons. The SCZO's ability to absorb  $\text{H}_2$  in-situ lowers its local concentration, promoted the improvement of NMC reaction thanks to the Le Chatelier's principle. To further improve the NMC reaction performance, an innovative autothermal catalytic wall reactor (ACWR) designed for self-sustaining NMC with high hydrocarbon product yield (>21%  $\text{C}_2$  & >27% Aromatics) and minimal coke formation. The system, potentially powered by combusting the sole co-product  $\text{H}_2$ , offers a self-sustained and negative neutral operation of NMC. Further operando studies via Spatial Resolved Capillary Inlet Mass Spectrometry (SpaciMS) have demonstrated that the increased local concentration and the volcanic axial concentration profile of ethylene within the ACWR highlight its effectiveness in comparison to traditional reactor designs. With the detection of a higher ethylene concentration near the reactor wall, SpaciMS studies have also provided experimental evidence that ethylene is a surface product of the  $\text{Fe}/\text{SiO}_2$  catalyst. A novel Pulsed Heating and Quenching (PHQ) thermochemical synthesis technique was applied to methane pyrolysis to demonstrate high selectivity to valuable  $\text{C}_2$  products. The technique's salient features include rapid activation of reactants at high temperatures for increased rates and conversions, and precise control over the heating process, enhancing the selectivity of desired products.

ADVANCED REACTION ENGINEERING FOR THE NONOXIDATIVE VALORIZATION  
OF METHANE

by

Sichao Cheng

Dissertation submitted to the Faculty of the Graduate School of the  
University of Maryland, College Park, in partial fulfillment  
of the requirements for the degree of  
Doctor of Philosophy  
2023

Advisory Committee:

Professor Dongxia Liu, Chair  
Professor Chen Zhang, Co-chair  
Professor Kyu Yong Choi  
Professor Amy J. Karlsson  
Professor Yifei Mo

© Copyright by  
Sichao Cheng  
2023

## Acknowledgements

To my beloved parents, this dissertation is dedicated.

First and foremost, I express my deepest gratitude to my committee chair, Prof. Dongxia Liu. Her passion for research and systematic problem-solving skills have been a beacon of inspiration throughout my doctoral journey. Her open-mindedness has broadened my academic horizons, enabling exploration into various aspects of catalysis and fostering collaborations with esteemed groups. This has not only enriched my perspective on our work but also paved the way for innovative approaches. Her constant support and belief in my capabilities have been the foundation of my academic pursuits and future career.

I extend heartfelt gratitude to a constellation of esteemed professionals who have significantly influenced my PhD journey. Professor Liangbing Hu and Dr. Qi Dong from the University of Maryland Center for Materials Innovation have been instrumental in shaping my research trajectory through our collaboration, marked by mutual trust and insightful discussions. Professor Dionisios G. Vlachos from the University of Delaware Delaware Energy Institute has provided invaluable support in CFD, microkinetic, COMSOL simulations, and machine learning, enriching our research narratives. I am also grateful to Professor Chen Zhang from the University of Maryland's Sustainable Separation Lab for his expertise in membrane science. My sincere appreciation goes to my entire PhD committee—Professors Kyu Yong Choi, Chen Zhang, Amy J. Karlsson, and Yifei Mo—for their unwavering commitment and invaluable time. I extend my thanks to the lab members in Dr. Dongxia Liu's group—Zixiao Liu, Ali Kamali, Emily Schulman, and Lu Liu—for their collaboration and support.

I acknowledge the significant contributions to my dissertation from Su Cheun Oh, Qi Dong, and Konstantinos Alexopoulos, whose work in various chapters has been pivotal. This academic journey has been possible through generous funding from the Department of Energy, Office of Fossil Energy (DE-FE0031877), and the ORISE Fellowship from the U.S. Army Research Laboratory.

Last part of this acknowledgements will go to my family. My heartfelt gratitude goes to my wife, Yuan Zhang, for her enduring support and encouragement throughout this journey. Although I always have felt I was the one helping her out most of the time in the lab, but her patience and love have been a source of strength. I wish to express my deepest gratitude to my parents, whose unwavering support has been my beacon through the darkest times of my life. Without their enduring presence, the resilience and accomplishments that now mark my journey would have remained beyond my grasp. As traditional Chinese parents, they may not often voice their love loudly, but their actions have silently fueled my drive to reach higher and achieve greater milestones. Their subtle yet profound influence has been the cornerstone of my progress and achievements.

# Table of Contents

Acknowledgements.....	ii
Table of Contents.....	iv
List of Tables.....	vii
List of Figures.....	viii
List of Abbreviations.....	xv
<b>Chapter 1: Introduction.....</b>	<b>1</b>
1.1 Methane, a strategic building block for petrochemicals.....	1
1.2 Advances in methane conversion processes to value added petrochemicals.....	3
1.3 Indirect methane conversion processes to higher hydrocarbons.....	4
1.4 Direct methane conversion processes to higher hydrocarbons.....	5
1.5 Direct nonoxidative methane conversion processes to higher hydrocarbons.....	8
1.5.1 Challenges in NMC reaction.....	9
1.5.2 Development of NMC reaction catalysts.....	11
1.5.2.1 Metal/zeolite catalysts for NMC.....	11
1.5.2.2 Single atom catalysts for NMC.....	13
1.5.2.3 Semiconductor based catalysts for NMC.....	14
1.5.3 Autothermal Reactor for NMC reaction.....	15
1.5.4 Electrified Reactor for NMC reaction.....	17
1.6 Thesis Overview.....	19
<b>Chapter 2: Understanding the Impact of Hydrogen Activation by SrCe<sub>0.8</sub>Zr<sub>0.2</sub>O<sub>3-δ</sub> Perovskite Membrane Material on Direct Non-Oxidative Methane Conversion.....</b>	<b>21</b>
2.1 Introduction.....	21
2.2 Experiments.....	24
2.2.1 Synthesis of membrane and catalyst material.....	24
2.2.2 Material characterization.....	25
2.2.3 Catalytic NMC reactions.....	27
2.3 Results and discussion.....	28
2.3.1 Physicochemical properties of SCZO perovskite and Fe/SiO <sub>2</sub> catalyst.....	28
2.3.2 NMC in the absence of H <sub>2</sub> co-feed in methane stream.....	30
2.3.2.1 NMC over Fe/SiO <sub>2</sub> catalyst or SCZO oxide.....	31
2.3.2.2 NMC over a mixture of Fe/SiO <sub>2</sub> catalyst and SCZO oxide.....	33
2.3.3 NMC in the absence of H <sub>2</sub> co-feed in methane stream.....	35
2.3.3.1 NMC over Fe/SiO <sub>2</sub> catalyst or SCZO oxide with H <sub>2</sub> co-feed.....	35
2.3.3.2 NMC over a mixture of Fe/SiO <sub>2</sub> catalyst and SCZO oxide with H <sub>2</sub> co-feed.....	37
2.3.4 Characterization of spent Fe/SiO <sub>2</sub> catalyst and SCZO oxide materials.....	39
2.3.4.1 Raman spectroscopy.....	39
2.3.4.2 Temperature programmer oxidation (TPO).....	41
2.3.4.3 X-ray photoelectron spectroscopy.....	44
2.4 Conclusion of chapter 2.....	48
<b>Chapter 3: Sharpening Spatial Temperature of Autothermal Catalytic Wall Reactor for Selective Nonoxidative Coupling of Methane.....</b>	<b>49</b>
3.1 Introduction.....	49
3.2 Experimental Preparation and Test Procedure.....	51

3.2.1	Reactor Structure .....	51
3.2.2	Reactor fabrication.....	52
3.2.2.1	Coating of NMC catalyst onto the inner reactor wall surface .....	52
3.2.2.2	Coating of fuel combustion catalyst onto the external surface of the reactor wall.....	53
3.2.3	Reactor fabrication.....	54
3.2.3.1	NMC reaction in the fix-bed and blank reactors.....	54
3.2.3.2	NMC reaction in the ACWR and single layer Fe/SiO <sub>2</sub> CWR .....	55
3.2.4	Catalyst characterization.....	56
3.3	Results and Discussion .....	56
3.3.1	Control experiments for ACWR.....	56
3.3.2	NMC Performance of ACWR.....	59
3.3.3	Coke analysis and evaluation of catalytic layer uniformity .....	63
3.3.4	Simulation of gas velocity profile and radial temperature profiles of ACWER using COMSOL.....	67
3.3.5	Potential CO <sub>2</sub> emission free ACWR for NMC reaction .....	73
3.4	Conclusion of Chapter 3 .....	77
<b>Chapter 4: A Spatially Resolved Analysis on Selective Nonoxidative Coupling of Methane in Autothermal Catalytic Wall Reactor .....</b>		<b>79</b>
4.1	Introduction.....	79
4.2	Experiments .....	82
4.2.1	Catalyst synthesis.....	82
4.2.2	Fabrication of Autothermal Catalytic Wall Reactor and Catalytic Wall Reactor .....	83
4.2.3	Spatially resolved capillary-inlet mass spectroscopy system (SpaciMS)...	84
4.3	Results and Discussion .....	86
4.3.1	Performance of spatially resolved standard catalytic wall reactor.....	86
4.3.2	Spatially resolved autothermal catalytic wall reactor analysis .....	88
4.4	Conclusion of chapter 4 .....	92
<b>Chapter 5: Programmable heating and quenching for efficient methane pyrolysis .....</b>		<b>94</b>
5.1	Introduction.....	94
5.2	Experiments preparation and test procedure.....	97
5.2.1	Materials and instruments .....	97
5.2.2	Reactor setup.....	98
5.2.3	Product detection for methane pyrolysis.....	103
5.2.4	Temperature acquisition.....	105
5.2.5	Spectroscopic and microscopic characterization .....	106
5.2.6	Modeling details for first-principles-based reactor simulations .....	107
5.3	Results and discussion .....	108
5.3.1	PHQ technique for rapid heating and quenching .....	108
5.3.2	PHQ technique for methane pyrolysis .....	114
5.3.3	Optimizing methane pyrolysis performance .....	118
5.3.4	First-principles-based reactor simulations for methane pyrolysis .....	120
5.4	Conclusion of chapter 5 .....	123
<b>Chapter 6: Conclusions and Future Works .....</b>		<b>125</b>

6.5	Conclusions.....	125
6.6	Future work.....	128
6.6.1	Renewable and scalable ACWR for NMC reaction .....	128
6.6.2	Assembly of electrical catalytic monolith reactor for NMC reaction.....	129
6.6.3	Fabrication of electrified membrane reactor model for chemical synthesis	
	130	
	<b>Bibliography</b> .....	132
	<b>List of Publications</b> .....	142
	Journals: .....	142
	Patents: .....	143
	Book Chapters:.....	144
	Presentations: .....	144
	Awards: .....	144

## List of Tables

**Table 2.1.** Ratio of D band to G band determined from Raman spectroscopy analysis for Fe/SiO<sub>2</sub> catalyst, SCZO perovskite oxide and 5 wt.% SCZO oxide mixed with 95 wt.% Fe/SiO<sub>2</sub> catalyst after 3.5 hours NMC reaction at 1273 K and at different H<sub>2</sub> co-feed concentrations.

**Table 3.1.** Contact time analysis for reaction gases in the catalytic wall reactor.

**Table 3.2.** Standard enthalpy of formation and heat capacity parameters of reactant and products in the NMC and methane combustion reaction.

**Table 5.1.** Geometrical parameters used in the numerical model.

**Table 5.2.** Electrical parameters used for heating the carbon paper at various conditions.

## List of Figures

**Figure 1.1.** Overview of reaction pathways for methane conversion to higher hydrocarbons process.

**Figure 1.2.** Elemental compositions of OCM catalysts with  $\text{Yield}_{\text{C}_2} > 25\%$  reported in the literature. All the catalysts were tested in a fixed-bed reactor in the co-feed mode under atmospheric pressure at temperatures from 943 to 1223 K.  $p(\text{CH}_4)/p(\text{O}_2) = 1.7\text{--}9.0$ , and contact times from 0.2 to 5.5 s. Reproduced with permission from reference<sup>1</sup>. Copyright 2011 Wiley-VCH.

**Figure 1.3.** Equilibrium conversion of NMC reaction from methane to benzene.

**Figure 2.1.** SEM images showing morphologies of Fe/SiO<sub>2</sub> catalyst (A) and SCZO perovskite oxide (B) particles. (C) and (D) are the XRD data and N<sub>2</sub> adsorption-desorption isotherms of both materials.

**Figure 2.2.** H<sub>2</sub>-TPD profiles (A) and XPS spectra of O1s photoelectron lines (B) of Fe/SiO<sub>2</sub> catalyst and SCZO perovskite oxide materials.

**Figure 2.3.** CH<sub>4</sub> conversion and product selectivity of NMC over Fe/SiO<sub>2</sub> catalyst (A) and SCZO perovskite oxide (B) materials. (1273 K temperature, 101.325 kPa pressure, 3200 mLg<sup>-1</sup>h<sup>-1</sup> space velocity, molar ratio of N<sub>2</sub>/CH<sub>4</sub> = 1/9, N<sub>2</sub> used as internal standard).

**Figure 2.4.** CH<sub>4</sub> conversion and product selectivity in NMC reaction over Fe/SiO<sub>2</sub> catalyst and SCZO perovskite oxide mixture with different sample arrangement format in the reactor: (A) SCZO packed on top of Fe/SiO<sub>2</sub>, (B) SCZO packed below Fe/SiO<sub>2</sub>, and (C) SCZO and Fe/SiO<sub>2</sub> well mixed. (Mass ratio of SCZO to Fe/SiO<sub>2</sub> = 1:2, 1273 K temperature, 101.325 kPa pressure, 2133 mLg<sup>-1</sup>h<sup>-1</sup> space velocity, molar ratio of N<sub>2</sub>/CH<sub>4</sub> = 1/9, N<sub>2</sub> used as internal standard).

**Figure 2.5.** CH<sub>4</sub> conversion and product selectivity in NMC over Fe/SiO<sub>2</sub> catalyst (A) and SCZO perovskite oxide (B) in a fixed-bed reactor at different hydrogen co-feed concentrations. (1273 K temperature, 101.325 kPa pressure, 3200 mLg<sup>-1</sup>h<sup>-1</sup> space velocity, molar ratio of N<sub>2</sub>/CH<sub>4</sub> = 1/9, N<sub>2</sub> used as internal standard, ToS of 1 hour).

**Figure 2.6.** CH<sub>4</sub> conversion and product selectivity in NMC reaction over Fe/SiO<sub>2</sub> catalyst and SCZO perovskite oxide mixture with different sample arrangement: (A) SCZO packed on top of Fe/SiO<sub>2</sub>, (B) SCZO packed below Fe/SiO<sub>2</sub>, and (C) SCZO and Fe/SiO<sub>2</sub> well mixed. (Mass ratio of SCZO to Fe/SiO<sub>2</sub> = 1:2 in (A) and (B) and 5:95 in (C), 1273 K temperature, 101.325 kPa pressure, 2133 mLg<sup>-1</sup>h<sup>-1</sup> (A) and (B) and 3200 mLg<sup>-1</sup>h<sup>-1</sup> (C) space velocities, molar ratio of N<sub>2</sub>/CH<sub>4</sub> = 1/9, N<sub>2</sub> used as internal standard, ToS of 1 hour).

**Figure 2.7.** Raman spectra of coke formed on spent Fe/SiO<sub>2</sub> catalyst (A), SCZO perovskite oxide (B) and Fe/SiO<sub>2</sub> catalyst mixed with 5 wt.% SCZO perovskites (C),

respectively, in NMC reaction in a fixed-bed reactor at different hydrogen co-feed concentrations after ToS of 3.5 hr.

**Figure 2.8.** CO<sub>2</sub> and CO evolution peaks in TPO profiles of spent Fe/SiO<sub>2</sub> catalyst (A and D), SCZO perovskite oxide (B and E), and 5wt.% SCZO in Fe/SiO<sub>2</sub> (C and F) at different H<sub>2</sub> co-feed concentrations after ToS of 3.5 h in NMC reactions.

**Figure 2.9.** XPS spectra of C1s (A), O1s (B), Si2p (C), Ce3d (D), Sr3d (E) and Zr3d (F) of fresh SCZO (red), fresh FeSiO<sub>2</sub> (black), spent FeSiO<sub>2</sub> mixed with SCZO in 2:1 mass ratio (green), spent FeSiO<sub>2</sub> mixed with 5 wt.% SCZO (blue), spent FeSiO<sub>2</sub> mixed with 5 wt.% SCZO under 10% H<sub>2</sub> co-feed (purple) and spent FeSiO<sub>2</sub> mixed with 5 wt.% SCZO under 20% H<sub>2</sub> co-feed (dark yellow), respectively.

**Schematic 3.1.** Schematics of autothermal millisecond catalytic wall reactor that couples endothermic NMC and exothermic fuel combustion on reactor wall surfaces. Sharp axial reactor temperature gradient and the use of H<sub>2</sub> byproduct as combustion fuel realize high hydrocarbon yield, negligible coke, and self-sustainability.

**Schematic 3.2.** Schematic drawing of the ACWR system coupling NMC and fuel oxidation reactions.

**Figure 3.1.** (a) Photo of autothermal ACWR with Fe/SiO<sub>2</sub> and Pt/Al<sub>2</sub>O<sub>3</sub> coated zones for coupling NMC and fuel combustion reactions; (b) morphology of Fe/SiO<sub>2</sub> catalyst region in inner tube surface of autothermal ACWR; and (c) morphology of Pt/Al<sub>2</sub>O<sub>3</sub> catalyst region on the exterior surface of the reactor wall.

**Figure 3.2.** SEM images showing a cross-section view of ACWR, where Pt/Al<sub>2</sub>O<sub>3</sub> catalyst layer is on the exterior surface of reactor wall and Fe/SiO<sub>2</sub> catalyst layer is fused onto the inner wall surface.

**Figure 3.3.** (a) Cross sectional view of reactor configurations (i) blank; (ii) fixed bed; (iii) CWR and (iv) ACWR. (b) methane conversion and product selectivity in NMC in reactor configurations from (a) in sequence. (Component color Indicators: coke, naphthalene, toluene, benzene, ethane, ethylene, and acetylene) (c) Measured temperature profiles in reactors heated by an electric furnace (top) and fuel combustion (bottom) controlled to the same peak temperature; and (d) NMC performance time-on-stream in ACWR. All data (a-c) was collected under steady state conditions. (NMC reaction: 0.48 L h<sup>-1</sup> gas flow with CH<sub>4</sub>:Ar ratio = 7, 101.325 kPa pressure, 0.375 g Fe/SiO<sub>2</sub> catalyst in fixed-bed reactor, 0.2 g Fe/SiO<sub>2</sub> catalyst in ACWR, Fe concentration = 0.075 wt%; fuel combustion: 145.2 L h<sup>-1</sup> gas flow with CH<sub>4</sub>:Air ratio = 0.1, 101.325 kPa pressure, 0.1 g Pt/Al<sub>2</sub>O<sub>3</sub> catalyst, Pt concentration = 1.0 wt%)

**Figure 3.4.** Effects of gas flow rate and direction on methane conversion and product selectivity in NMC in the ACWR. (a) Temperature profile, (b) methane conversion and product selectivity of varying methane flow rate in the NMC channel at a fixed combustion gas flow rate of 145.2 L h<sup>-1</sup> gas flow (CH<sub>4</sub>:Air ratio = 0.1) under co-current

flow. (c) Temperature profile, (d) methane conversion and product selectivity of varying methane flow rate in the NMC channel at a fixed combustion gas flow rate of  $145.2 \text{ L h}^{-1}$  gas flow ( $\text{CH}_4:\text{Air}$  ratio = 0.1) under counter-current flow. (e) Varying combustion gas flow rate at a fixed NMC gas flow rate of  $0.48 \text{ L h}^{-1}$  gas flow ( $\text{CH}_4:\text{Ar}$  ratio = 7). (f) Maximized NMC performance by adjusting both NMC and fuel combustion flow rates. (Component color Indicators for (b), (d), (e) and (f): ■ coke, ■ naphthalene, ■ toluene, ■ benzene, ■ ethane, ■ ethylene and ■ acetylene)

**Figure 3.5.** Methane conversion and product selectivity of two ACWR manufactured under identical process. (Reaction condition:  $0.48 \text{ L h}^{-1}$  gas flow with  $\text{CH}_4:\text{Ar}$  ratio = 7,  $101.325 \text{ kPa}$  pressure,  $0.2 \text{ g Fe/SiO}_2$  catalyst in ACWR, Fe concentration =  $0.075 \text{ wt}\%$ ; Fuel combustion:  $165 \text{ L h}^{-1}$  gas flow with  $\text{CH}_4:\text{Air}$  ratio = 0.1,  $101.325 \text{ kPa}$  pressure,  $0.1 \text{ g Pt/Al}_2\text{O}_3$  catalyst, Pt concentration =  $1.0 \text{ wt}\%$ )

**Figure 3.6.** Inner tube of ACWR after 6 hours of reaction. (Reaction condition:  $0.48 \text{ L h}^{-1}$  gas flow with  $\text{CH}_4:\text{Ar}$  ratio = 7,  $101.325 \text{ kPa}$  pressure,  $0.2 \text{ g Fe/SiO}_2$  catalyst in ACWR, Fe concentration =  $0.075 \text{ wt}\%$ ; Fuel combustion:  $165 \text{ L h}^{-1}$  gas flow with  $\text{CH}_4:\text{Air}$  ratio = 0.1,  $101.325 \text{ kPa}$  pressure,  $0.1 \text{ g Pt/Al}_2\text{O}_3$  catalyst, Pt concentration =  $1.0 \text{ wt}\%$ )

**Figure 3.7.** TGA curve of coke formed on ACWR after TOS = 6 hrs of NMC reaction. (Reaction condition:  $0.48 \text{ L h}^{-1}$  gas flow with  $\text{CH}_4:\text{Ar}$  ratio = 7,  $101.325 \text{ kPa}$  pressure,  $0.2 \text{ g Fe/SiO}_2$  catalyst in ACWR, Fe concentration =  $0.075 \text{ wt}\%$ ; Fuel combustion:  $165 \text{ L h}^{-1}$  gas flow with  $\text{CH}_4:\text{Air}$  ratio = 0.1,  $101.325 \text{ kPa}$  pressure,  $0.1 \text{ g Pt/Al}_2\text{O}_3$  catalyst, Pt concentration =  $1.0 \text{ wt}\%$ )

**Figure 3.8.** (a) Laser microscope image of  $\text{Pt/Al}_2\text{O}_3$  surface on ACWR the surface size is  $1374 \times 1028 \mu\text{m}$ . (b) Height scan of  $\text{Pt/Al}_2\text{O}_3$  surface. (c) Horizontal scan along the reaction tube. The Ra values of Horizontal line 1,2 and 3 are  $12.3$ ,  $22.5$  and  $13.4 \mu\text{m}$ . (d) Thickness variation of the  $\text{Pt/Al}_2\text{O}_3$  layer surface on Horizontal line 1, 2 and 3 based on the average mean thickness. Color code of (c) and (d) is identical.

**Figure 3.9.** SEM images showing a cross-section view of ACWR, where  $\text{Fe/SiO}_2$  catalyst layer is fused onto the inner wall surface and their thickness is marked in red. The cross-section position of the catalytic wall zone is (A)  $0 \text{ mm}$ , (B)  $35 \text{ mm}$  and (C)  $90 \text{ mm}$ .

**Figure 3.10.** Reactor schematic and parameters of autothermal catalytic wall reactor used for COMSOL simulation. A cocurrent flow is illustrated.

**Figure 3.11.** Axial temperature comparison of steady-state simulation and experiment results at center line of combustion chamber with flow rates of  $145.2$  and  $171.6 \text{ L h}^{-1}$  ( $\text{CH}_4:\text{Air}$  ratio = 0.1). The arrow indicates the cocurrent flow in the NMC chamber. First, the flow was simulated in the NMC channel to understand the time-scale that enables efficient catalytic performance.

**Figure 3.12.** (a) Modeled maximum local gas velocity (left-y axis) and local temperature (right y-axis, red) in the NMC chamber as a function of iron silica catalyst coating thickness. (b) Radial temperature profile across the whole reactor at 130 mm axial position for combustion chamber gas flow of 145.2 L h<sup>-1</sup> (red) and 171.6 L h<sup>-1</sup> (blue). (NMC channel: Ar flow 0.48 L h<sup>-1</sup>, coating thickness 0.55mm; combustion channel CH<sub>4</sub>:Air ratio = 0.1, 101.325 kPa pressure; co-current flow mode.)

**Figure 4.1.** Axial and radial temperature and concentration profile probing via SpaciMS setup for nonoxidative methane conversion in: (A) Single layer Fe/SiO<sub>2</sub> catalyst wall heated with conventional furnace; (B) Autothermal catalytic wall reactor coupled with methane oxidation reaction.

**Figure 4.2.** Autothermal Fe/SiO<sub>2</sub> catalytic wall reactor: (A)(C)(E) Axial temperature profiles at near the reactor inner wall with peak temperature at 1273 K, 1310 K and 1413 K. (B)(D)(F) Axial local concentration of nonoxidative methane conversion products: acetylene, ethylene, and ethane, respectively in autothermal catalytic wall reactor respect to (A), (C) and (E). (■ Acetylene; ● Ethylene; ▲ Ethane; ▼ Benzene; ◆ Toluene; ♠ Naphthalene)

**Figure 4.3.** (A)(C) axial temperature profiles of pre-coked autothermal catalytic wall reactor with peak temperature at 1248 K and 1355 K. (B)(D) Axial local concentration of nonoxidative methane conversion products: acetylene, ethylene, and ethane, respectively in autothermal catalytic wall reactor respect to (A) and (C) (■ Acetylene; ● Ethylene; ▲ Ethane)

**Figure 4.4.** Effects of gas flow rate and direction on methane conversion and product selectivity in NMC in the ACWR. (a) Temperature profile, (b) methane conversion and product selectivity of varying methane flow rate in the NMC channel at a fixed combustion gas flow rate of 145.2 L h<sup>-1</sup> gas flow (CH<sub>4</sub>:Air ratio = 0.1) under co-current flow. (c) Temperature profile, (d) methane conversion and product selectivity of varying methane flow rate in the NMC channel at a fixed combustion gas flow rate of 145.2 L h<sup>-1</sup> gas flow (CH<sub>4</sub>:Air ratio = 0.1) under counter-current flow. (e) Varying combustion gas flow rate at a fixed NMC gas flow rate of 0.48 L h<sup>-1</sup> gas flow (CH<sub>4</sub>:Ar ratio = 7). (f) Maximized NMC performance by adjusting both NMC and fuel combustion flow rates. (Component color Indicators for (b), (d), (e) and (f): ■ coke, ■ naphthalene, ■ toluene, ■ benzene, ■ ethane, ■ ethylene and ■ acetylene)

**Schematic 5.1.** Digital images of the PHQ reactor

**Schematic 5.2.** Schematic drawing of the electrical circuit.

**Schematic 5.3.** Four selected frames from a recorded video during the cooling process of the carbon paper heater.

**Figure 5.1.** Comparison between our PHQ method and conventional continuous heating using a CH<sub>4</sub> pyrolysis model reaction. a, Schematic of a typical temperature

profile by continuous heating. Continuous heating creates a variety of products owing to the lack of temporal tunability over the temperature profile and thus the resulting reaction pathways. b, Schematic of an estimated temperature profile by the PHQ method. PHQ selectively produces value-added C<sub>2</sub> products. The high temperature ensures high conversion, whereas the transient heating duration enables high selectivity. c, Comparison of CH<sub>4</sub> pyrolysis by PHQ in this work and continuous heating reported in the literature<sup>2</sup>. At comparable CH<sub>4</sub> conversions (about 13%), continuous heating of the non-catalytic CH<sub>4</sub> pyrolysis reaction results in coke as the major product (grey) with other minor products (maroon), whereas CH<sub>4</sub> pyrolysis by PHQ showcases its >75% selectivity to C<sub>2</sub> products (red). d, Our metal-catalyst-free PHQ technique (red stars) even outperforms most literature reports of CH<sub>4</sub> pyrolysis reactions with optimized catalysts conducted by continuous heating in terms of the C<sub>2</sub> product selectivity at a wide range of CH<sub>4</sub> conversions<sup>3-10</sup>.

**Figure 5.2.** Operation of the PHQ technique. a, Schematic of the reactor design. The CH<sub>4</sub> molecules pass through the reactor and interact with the heated porous carbon paper to rapidly transform into desirable value-added C<sub>2</sub> products. b, Digital images of the carbon heater in power off (bottom) and power on (top) states, corresponding to the switch from room temperature (about 300 K) to high temperature (about 2,400 K). c, Scanning electron microscopy image of the carbon heater, showcasing the highly porous microstructure and the catalyst-free surface. Scale bar, 50 μm. d, Digital image of the flexible carbon heater. e, The temporal temperature pattern of the carbon heater is tuned by increasing the input electrical power for higher peak temperatures at fixed pulse duration (dashed grey line). Insets are digital images showing the carbon paper being heated to different temperatures. f, The temporal temperature profile of the carbon heater can also be tuned by varying the pulse duration at a fixed peak temperature. Increased pulse duration requires decreased power input to reach the same peak temperature. g, Numerical simulation verifies that the temporal temperature pattern of the gas molecules closely follows that of the carbon heater (0.02 s on, 1.08 s off; T<sub>high</sub> = 1,600 K). The three traces represent the temporal temperature patterns of three spatial positions (in the reactor cross-section) vertically above the middle point on the upper surface of the carbon paper with distances (d) of 0R', 1/16R' and 1/8R'. R' is the closest distance from the middle point on the upper surface of the carbon heater to the edge of the cylindrical quartz tube reactor (R' = R - 1/2D, in which R is the radius of the reactor and D is the thickness of the carbon paper). The insets show the cross-sectional contour maps of the gas temperature distribution when the time on stream equals 0.02 s (when T<sub>high</sub> is reached) and 0.2 s (when most gas molecules are cooled down)

**Figure 5.3.** Peak temperature (T<sub>high</sub>) measurement using a high-speed camera.

**Figure 5.4.** Cross-sectional contour images of the gas temperature distribution when the time on stream equals 0.01 s, 0.02 s, 0.1 s, 0.2 s, 0.5 s, and 1.1 s in a pulse period (0.02 s on, 1.08 s off; T<sub>high</sub> = 1,600 K). The temperature of the gas near the surface of the carbon paper (whose geometry is not optimized) follows closely to that of the heating element.

**Figure 5.5.** Cross-sectional contour images of the gas temperature distribution when the time on stream equals 0.01 s, 0.02 s, 0.1 s, 0.2 s, 0.5 s, and 1.1 s in a pulse period (0.02 s on, 1.08 s off;  $T_{\text{high}} = 1,800$  K). The temperature of the gas near the surface of the carbon paper (whose geometry is not optimized) follows closely to that of the heating element.

**Figure 5.6.** The utility and advantages of our PHQ technique. a, Comparison between (from left to right): (1) non-catalytic  $\text{CH}_4$  pyrolysis using continuous furnace heating at 1,273 K; (2) catalytic  $\text{CH}_4$  pyrolysis with a state-of-the-art Fe/silica catalyst using continuous furnace heating at 1,273 K; (3)  $\text{CH}_4$  pyrolysis with carbon paper using continuous furnace heating at 1,273 K; (4)  $\text{CH}_4$  pyrolysis using PHQ with a  $T_{\text{high}}$  of 2,200 K and pulse duration of 0.055 s over a period of 1.1 s (0.055 s on, 1.045 s off,  $T_{\text{avg.}} < 900$  K). A flow rate of 24 sccm was used for all four reaction conditions. b,  $\text{CH}_4$  conversion increases with  $T_{\text{high}}$  monotonically by PHQ, as demonstrated using a pulse duration of 0.02 s over a period of 1.1 s (0.02 s on, 1.08 s off). Error bars denote standard deviation with the value of  $n \geq 3$ . c, Product selectivity by PHQ at various  $T_{\text{high}}$  values with a fixed pulse duration of 0.02 s on and 1.08 s off. d, Product selectivity by PHQ using various pulse durations at a fixed  $T_{\text{high}}$  of 1,800 K. A flow rate of 4 sccm was used for b–d. The error range for  $\text{C}_2$  product selectivity was found to be  $\pm 3\%$ . e, Bayesian-optimization-based active learning framework to optimize the desired product ( $\text{C}_2\text{H}_4$ ) yield. f, The surrogate model response surface of the  $\text{C}_2\text{H}_4$  yield as a function of  $T_{\text{high}}$  and the pulse duration. The red colour indicates a high  $\text{C}_2\text{H}_4$  yield. The dots represent the sampled experimental data points on the basis of the prediction by the acquisition function. g, The optima and experimental  $\text{C}_2\text{H}_4$  yield in each active learning iteration, corresponding to the experiment numbers.

**Figure 5.7.** methane conversion and  $\text{C}_2$  product selectivity by PHQ as a function of the time on stream.

**Figure 5.8.** Programmable control by the PHQ technique. (a) Programmable control over the peak temperature ( $T_{\text{high}}$ ) from 1,200 K to 2,200 K by PHQ. (b) Programmable control over the pulse duration from 0.02 s to 0.33 s by PHQ.

**Figure 5.9.** Modeling details. (a) The continuous stirred tank reactor setup used to model both the continuous heating and PHQ methods. (b) Temporal temperature profiles used for the steady-state and transient reactors, simulating conventional continuous heating and PHQ, respectively.

**Figure 5.10.** Heat rate profiles for the steady-state and transient reactors, simulating conventional continuous heating and our PHQ method, respectively. The heat of the reaction constitutes only a small portion of the overall heat required to operate the system at the set methane conversion of 5%.

**Figure 5.11.** Modeling of  $\text{CH}_4$  pyrolysis reactions under continuous heating and PHQ. Comparison of the (a) product distribution and (b) energy required by the  $\text{CH}_4$  pyrolysis

reaction between steady-state (simulating continuous heating) and transient (simulating PHQ) operations at an identical CH<sub>4</sub> conversion of 5%. (c) CH<sub>4</sub> conversion and product distribution as a function of astronomic time (i.e., clock time or external time of the system) under isothermal conditions at 1,500 K. (d) Characteristic timescales for each elementary step in the reaction path of CH<sub>4</sub> pyrolysis toward aromatics formation, simulated at 1,500 K. The side species are omitted for clarity. The timescale for the slowest step ( $\tau_{\text{cyclization}} = 0.368$  s) along this reaction path is indicated in red. (e) Reaction pathway analysis for CH<sub>4</sub> pyrolysis by steady-state (blue) and transient (red) operations under isothermal conditions at 1,500 K. The percentages, next to each elementary step, correspond to the net reaction rates normalized by the net reaction rate of the initial dehydrogenation (initial CH<sub>4</sub> activation step) from CH<sub>4</sub> to CH<sub>3</sub>•. For PHQ, the secondary and subsequent reactions after the propargyl radical (C<sub>3</sub>H<sub>3</sub>•) are quenched (the shaded arrows), therefore yielding more C<sub>2</sub> products.

## List of Abbreviations

EIA - U.S. Energy Information Administration

WGSR - water-gas shift reaction

POM - partial oxidation of methane

OCM - oxidative coupling of methane

NMC - non-oxidative methane conversion

MDA - methane dehydroaromatization

MTOAH - methane to olefins, aromatics, and hydrogen

$\cdot\text{CH}_3$  - methyl radical

SACs -single-atom catalysts

STEM-HAADF – high-angle annular dark-field scanning transmission electron microscopy

ACWR - autothermal catalytic wall reactor

CWR - catalytic wall reactor

BET - Brunauer, Emmett and Teller

SEM - scanning electron microscopy

TGA - thermogravimetric analysis

SpaciMS - spatially resolved capillary-inlet mass spectroscopy system

PHQ - programmable heating and quenching

XRD - x-ray diffraction

SCZO -  $\text{SrCe}_{0.8}\text{Zr}_{0.2}\text{O}_{3-\delta}$

TPO - temperature-programmed oxidation

# Chapter 1: Introduction

## *1.1 Methane, a strategic building block for petrochemicals*

In 2022, international unrest such as the war in Ukraine caused severe disruptions in crude oil supplies, leading the US to make an unprecedented withdrawal of nearly 352 million barrels from its Strategic Petroleum Reserve<sup>11,12</sup>. As the world grapples with the volatile pricing and looming depletion of crude oil, the search for more sustainable and accessible resources intensifies<sup>13,14</sup>. Among these alternatives, methane - the primary component of natural gas, methane clathrates, and biogas - is becoming a strong contender<sup>15</sup>.

Methane boasts the highest hydrogen-to-carbon ratio among hydrocarbons, resulting in less carbon dioxide emission when burned compared to traditional fossil fuels like oil and coal. This advantage gives methane a cleaner footprint in the energy sector. The U.S. Energy Information Administration (EIA) states that as of 2022, around 38% of U.S. natural gas consumption was used for electricity generation, with industrial, residential, and commercial heating accounting for approximately 58%<sup>16</sup>. This heavy reliance on natural gas is largely due to its abundant reserves and affordability. Current data suggests that the U.S. possesses about 2,828 trillion cubic feet of technically recoverable natural gas, with a significant proportion sourced from shale formations through innovative extraction techniques such as horizontal drilling and hydraulic fracturing<sup>17</sup>.

However, a sizable percentage of natural gas reserves are situated in remote areas, far from the industrial hubs and population centers commonly associated with

oil extraction.<sup>11</sup> This geographical incongruity exacerbates the challenges and costs associated with delivering gas to end-users. Therefore, gas flaring, the burning of natural gas for reasons of safety, regulatory compliance, and economics, is a common practice<sup>18</sup>. Capturing and utilizing the natural gas associated with oil extraction is often deemed prohibitively expensive, especially when the production sites are small and dispersed. Adding to the complexity, methane is 25 times more potent than carbon dioxide at trapping heat in the atmosphere<sup>19</sup>. It is estimated that more than 140 billion cubic meters of natural gas are burned annually, leading to a global economic loss of over \$40 billion each year<sup>20</sup>. Thus, it's more efficient to convert natural gas into useful products at the source, then transport these end products to consumers, ultimately enhancing efficiency and reducing logistical complexities.

One of the main challenges of converting methane into liquid, olefins, alcohols, and other high-value products lies in activating stable methane<sup>21-25</sup>. Methane, with its nonpolar, symmetrical, and tetrahedral structure, has four strong, localized C-H bonds formed from the overlap of carbon and hydrogen atomic orbitals<sup>26</sup>. This results in a C-H bond strength of 440 kJ/mol. Therefore, using methane in chemical synthesis requires significant energy, specific catalysts, or extreme reaction conditions to overcome the high activation barrier. The considerable energy required to break the bonds often necessitates high reaction temperatures in both homolytic and heterolytic systems. However, these elevated temperatures can trigger uncontrolled secondary or side reactions, resulting in poor product selectivity. Advances in process efficiency and innovations in process chemistry are both key to developing economically viable solutions for converting natural gas into other petrochemical products.

## *1.2 Advances in methane conversion processes to value added petrochemicals*

Despite its abundant availability and cost-effectiveness, methane's use as a chemical feedstock is relatively untapped. Currently, less than 10% of global methane is employed in this capacity<sup>21</sup>. A significant portion of methane is subject to steam reforming reactions, contributing to approximately 50% of the world's hydrogen production, which is primarily used in the synthesis of fertilizers<sup>27</sup>. However, the steam reforming process also generates greenhouse gases, specifically carbon dioxide, as a byproduct of the water-gas shift reaction (WGSR).

Furthermore, there has been considerable research interest in the conversion of methane into higher hydrocarbons to fully leverage its carbon content. In Figure 1.1, selected indirect and direct pathways of the methane conversion to higher hydrocarbon process are presented. Indirect pathways entail multi-stage methods to convert methane into end products via an intermediate species, commonly syngas (a mixture of hydrogen and carbon monoxide)<sup>22,28</sup>. These methods can be energy-intensive and complex due to multiple stages of conversion. Direct pathways, on the other hand, aim to convert methane into final products in a single step, with or without the use of oxidative agents<sup>29,30</sup>. These methods are often simpler and more energy-efficient, but they can also be challenging due to the chemical stability of methane and the need for specific catalysts or conditions.<sup>31</sup>

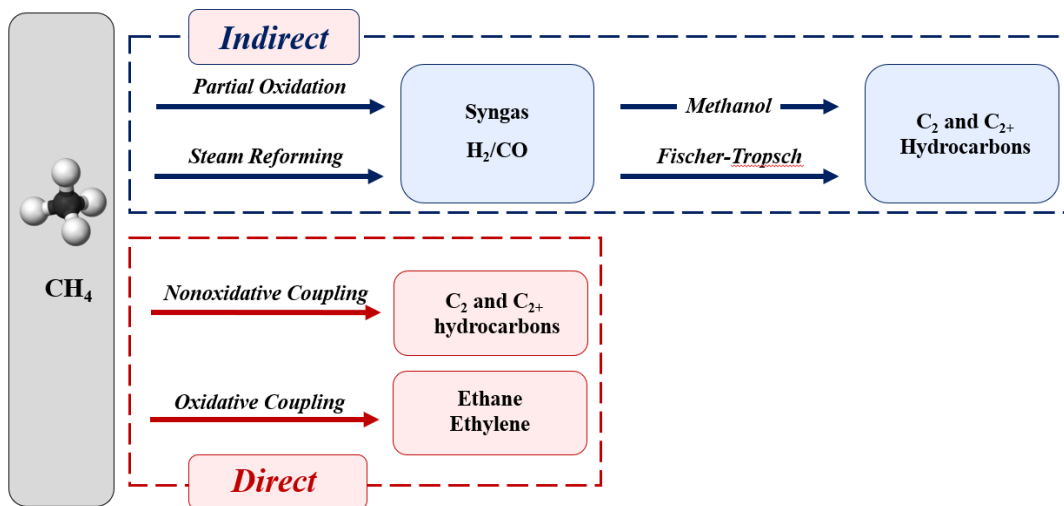
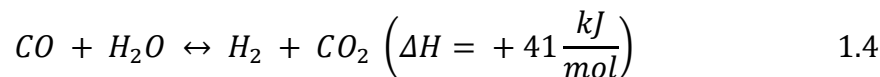
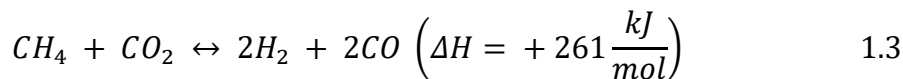
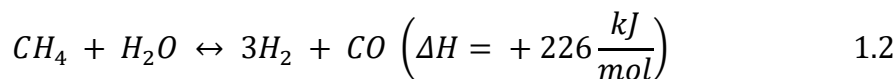
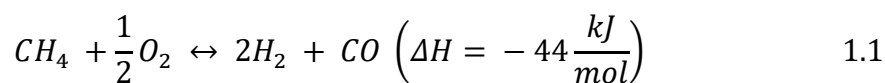


**Figure 1.1.** Overview of reaction pathways for methane conversion to higher hydrocarbons process.

### 1.3 Indirect methane conversion processes to higher hydrocarbons

Over the last century, indirect methods of methane conversion have become well-established. The first step in these methods is typically the conversion of methane into syngas via one of three major pathways<sup>32-34</sup>: (i) partial oxidation of methane (POM) (Eq. 1.1); (ii) steam reforming of methane (Eq. 1.2); and (iii) dry reforming of methane (Eq. 1.3):



In the case of POM (Eq 1.1), syngas is produced using catalysts such as platinum (Pt), rhodium (Rh), or nickel (Ni) alongside cerium oxide promoters<sup>35</sup>. This

method yields a hydrogen to carbon monoxide (H<sub>2</sub>:CO) ratio of 2, within a temperature range of 700-900°C. Owing to the exothermic nature of this reaction, it requires less energy input. However, the challenge with POM lies in activating the strong C-H bonds of methane without leading to complete combustion of methane into carbon dioxide.

Alternatively, the most common route for methane conversion into syngas is steam reforming (Eq 1.2), which typically employs nickel-based catalysts<sup>36</sup>. This method yields a higher H<sub>2</sub>:CO ratio of 3 and is accompanied by the WGSR (Eq 1.4), which produces carbon dioxide.

Lastly, dry reforming of methane (Eq 1.3), which generates syngas with a balanced H<sub>2</sub>:CO ratio of 1, presents a promising path towards achieving negative greenhouse gas emissions. Commonly, metal-based catalyst such as Ni, Mo, MgO and Ir supported by zeolite, alumina and SiN<sub>x</sub>, were commonly used to drive this reaction<sup>37-39</sup>. This method merges methane and carbon dioxide but does have its challenges. These include potential carbon deposition, high energy requirements, and a low H<sub>2</sub>:CO ratio for subsequent olefin formation processes<sup>40</sup>. Furthermore, dry reforming of methane is a highly endothermic reaction which requires reaction temperature in the range of 900-1273 K to reach considerable methane conversion.

#### 1.4 Direct methane conversion processes to higher hydrocarbons

Direct routes for methane conversion offer an appealing alternative to the indirect methods previously discussed. These direct routes are not only more cost-effective but also streamline the process through one-step synthesis. Two such methods include the oxidative coupling of methane (OCM), first introduced by Keller and Bhasin in 1982<sup>41</sup>, and non-oxidative methane conversion (NMC)<sup>42</sup>, which encompasses

processes such as methane dehydroaromatization (MDA)<sup>43-46</sup>, methane to olefins, aromatics, and hydrogen (MTOAH)<sup>47-49</sup>, as well as methane pyrolysis<sup>2</sup>. In these direct conversion processes, the efficacy of catalysts in activating C-H bonds is pivotal, potentially displacing the energy-intensive syngas route with a more efficient alternative.

The OCM process's reaction mechanism involves the extraction of a hydrogen atom from a methane molecule by an oxygen atom on a catalyst's surface<sup>50</sup>. This reaction forms a methyl radical ( $\cdot\text{CH}_3$ ) that couples to form ethane. Although the OCM pathway is exothermic and can transform methane into ethane and ethylene at low temperatures under a wide range of operating conditions, this method still encounters its own challenges. One of the main issues is the formation of thermodynamically favorable yet undesired deep oxidation compounds ( $\text{CO}_x$ ).

Efforts have been directed towards identifying optimal catalysts to selectively convert methane into  $\text{C}_2$  hydrocarbons under oxygen environment. Initial studies identified various metal oxide catalysts for the OCM reaction. In Figure 1.2, an upper bound of  $\text{C}_2$  yield of approximately 25% was predicted<sup>25</sup> with theoretical kinetic evaluation of rate constants for all elementary steps. Subsequently, mixed oxide catalysts, such as  $\text{Li/MgO}$ <sup>51</sup> and  $\text{Mn/Na}_2\text{WO}_4/\text{SiO}_2$ <sup>52</sup>, have demonstrated the highest reported  $\text{C}_2$  yields under one-pass fixed bed setup.

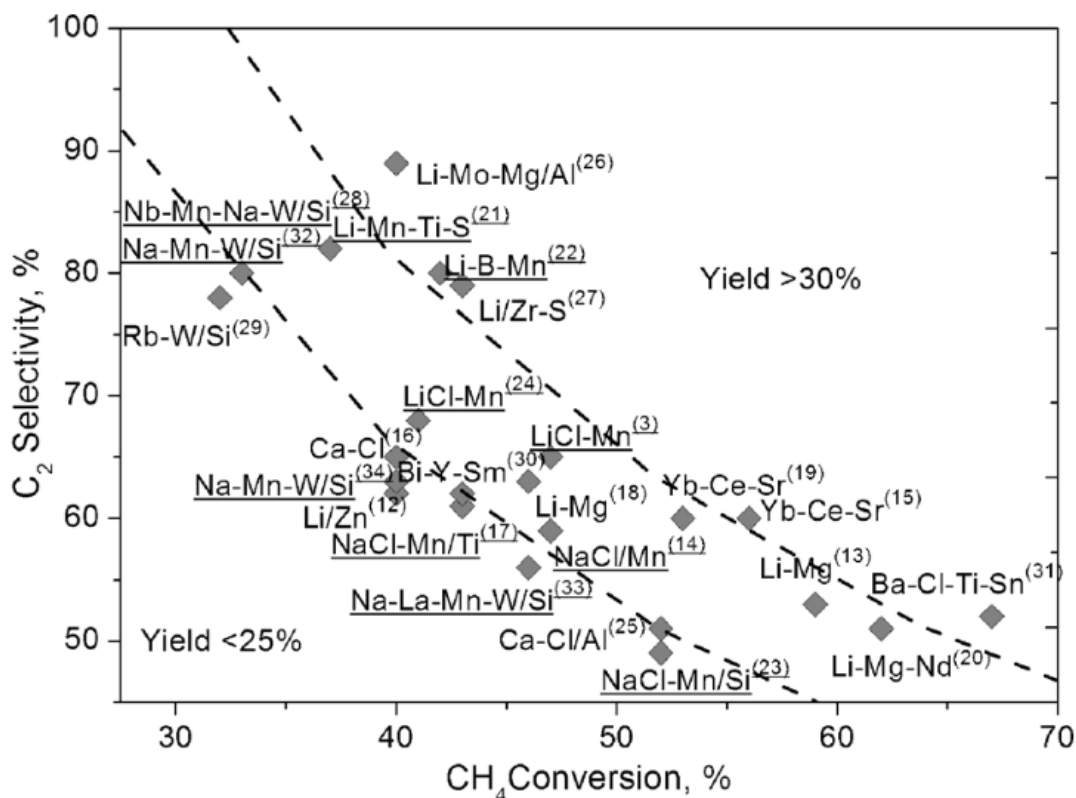


**Figure 1.2.** Elemental compositions of OCM catalysts with Yield<sub>C<sub>2</sub></sub> > 25% reported in the literature. All the catalysts were tested in a fixed-bed reactor in the co-feed mode under atmospheric pressure at temperatures from 943 to 1223 K. p(CH<sub>4</sub>)/p(O<sub>2</sub>) = 1.7–9.0, and contact times from 0.2 to 5.5 s. Reproduced with permission from reference<sup>1</sup>. Copyright 2011 Wiley-VCH.

Despite these advances, the commercialization of the OCM process has faced various hurdles. Siluria Technologies, for instance, claims to have developed a commercially viable OCM process that integrates OCM with alkane cracking reactions<sup>53</sup>. This method produces ethylene and propylene and improves the process in two significant ways: (1) by coupling the exothermic OCM reaction with endothermic cracking reactions to enhance heat utilization, and (2) by recycling methane, propane, and CO<sub>x</sub> back into the integrated reactor to boost the process's overall carbon efficiency. Nonetheless, enhancing the single-pass C<sub>2</sub> yield continues to be a

formidable challenge. Further research and development in this domain are imperative to fully unlock the potential of methane as a chemical feedstock.

### 1.5 Direct nonoxidative methane conversion processes to higher hydrocarbons

The non-oxidative methane conversion (NMC) process presents a unique advantage as it directly converts methane into C<sub>2</sub> hydrocarbons and aromatics, yielding hydrogen as a byproduct. Its potential for remote operation and its status as a negative carbon process - given that no CO<sub>x</sub> is produced in the product effluent - make it particularly attractive. The NMC process is further divided into non-catalytic and catalytic methods.

The non-catalytic method, also known as methane pyrolysis, demands a reaction temperature above 1473K. It's based on the free energy of formation of hydrocarbons and yields acetylene and ethylene as products. As the temperature increases beyond 1503K, acetylene becomes the most stable hydrocarbon and dominates the gas product mix. However, the process also produces solid coke species as a significant byproduct, often leading to deposit formation on internal reactor surfaces. The extreme temperature requirement and uncontrolled radical chain process limit the widespread use of this homogeneous reaction.

In response to these challenges, research has pivoted towards developing new catalysts to lower the required temperature and improve product selectivity. For instance, the formation of aromatics from the zeolite catalyst for the OCM process inspired the exploration of a metal-modified ZSM-5 catalyst for the NMC reaction via the methane dehydroaromatization (MDA) process. This bifunctional zeolite catalyst facilitates methane activation at the metal active site and subsequent aromatization at

the Bronsted acid site at a milder reaction temperature of 973K. The process exhibits high selectivity towards Benzene, a key petrochemical intermediate used in the production of plastics, lubricants, rubbers, and pesticides. However, the rapid deactivation of the zeolite-based catalyst for the MDA reaction, primarily due to coke formation within the zeolite framework's pore structure, continues to pose a significant challenge.

To this day, no commercially viable NMC process has been developed, as multiple challenges persist. However, current research and development efforts are ongoing to unlock this process's full potential and make methane an even more valuable chemical feedstock.

#### *1.5.1 Challenges in NMC reaction*

NMC is a process that directly transforms methane into higher-value products such as ethylene, benzene, or hydrogen, bypassing the need for an initial oxidation step. While promising, the NMC process encounters several formidable challenges including: (1) thermodynamic stability, (2) low selectivity, (3) catalyst deactivation, and (4) kinetic hindrance.

The strong C-H bonds in methane, which have a high bond dissociation energy, make methane thermodynamically stable. To illustrate, consider the MDA reaction (refer to Figure 1.3); under ambient pressure, a temperature exceeding 873K is needed to achieve 50% conversion of methane in equilibrium conditions. As the reaction temperature rises, the Gibbs free energy of formation markedly favors the production of coke, followed by aromatics (such as benzene) and C<sub>2</sub> hydrocarbons. This dynamic

makes it challenging to control the NMC reaction's output for producing more valuable or desired products.

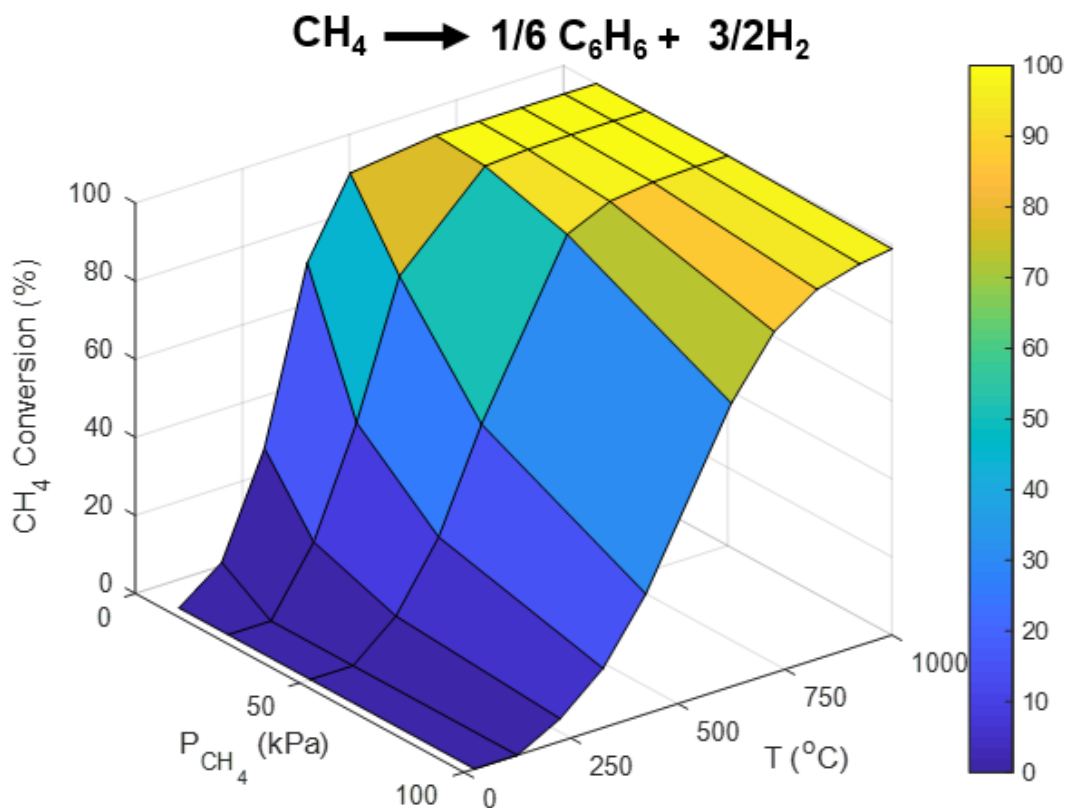


**Figure 1.3.** Equilibrium conversion of NMC reaction from methane to benzene.

In addition, NMC catalysts typically suffer from deactivation issues due to coking and sintering. The formation of carbon species (coke) above 800K is detrimental as it blocks the active sites, thereby impeding catalytic performance. The high temperature requirements of the NMC process often cause agglomeration or sintering of the metal particles or supporting materials. These changes in metal site properties or a decrease in overall surface area can result in poor catalyst performance.

Kinetic hindrance is another obstacle for the NMC process. The substantial amount of energy needed to break these strong C-H bonds creates a barrier that

decelerates the reaction rate, leading to low conversion. Moreover, once the first C-H bond in methane is broken, the resultant intermediate products are typically more reactive than the original methane molecule, and they tend to continue to react further and at a faster pace. This reactivity often results in poor product selectivity.

Hence, enhancing the NMC process is a complex task, demanding a concerted effort in catalyst development, process optimization, and innovative reactor technology design.

### *1.5.2 Development of NMC reaction catalysts*

A very high reaction temperature is generally required for NCM as a result of the tremendous thermodynamic barrier, which causes severe coking deactivation of the catalyst. Therefore, significant efforts have been devoted to exploring efficient catalytic systems to enable activation of the methane C–H bond and C–C coupling to improve the NCM reaction for the efficient utilization of methane. Here are a few types of catalysts that have been studied for this purpose:

#### *1.5.2.1 Metal/zeolite catalysts for NMC*

Since Mo/ZSM-5 was first identified as an efficient catalyst for MDA in 1993, a surge of efforts has been directed towards enhancing zeolite-based catalysts for NMC. Strategies for boosting overall catalytic performance have been multifaceted, ranging from the modulation of metal species to alterations in zeolite support types, and the integration of various promoters within the catalyst structure. Zeolites, a class of microporous aluminosilicate material, have wide applications in separation and catalysis due to their unique physical and chemical properties, such as high surface

area, tunable acidity, and thermal stability. A multitude of metals and metal compounds have been tested on zeolite catalysts, including Zn, Cu, Pt, Ni, Mo, Fe, V, Cr, W, Mo, Mo<sub>2</sub>C, MoO<sub>2</sub>, and MoO<sub>3</sub>, but Mo/ZSM-5 remains the most effective single metal catalyst for the NMC reaction<sup>44,54,55</sup>.

Kosinov et al. delved into the correlation between Mo loading levels and the structural integrity and textural stability of the Mo/HZSM-5 catalyst<sup>56</sup>. Lower Mo/Al ratios encouraged the distribution of both monomeric and dimeric Mo-oxo species throughout the zeolite's micropores, a dispersion that remained constant despite elevated calcination temperatures. Consequently, catalysts with lower Mo loading contents (1-2 wt%) displayed stable catalytic performance, unaffected by the calcination temperature. Yet, a shift was noted when Mo loading increased to 5 wt% in Mo/HZSM-5; a direct reaction between the Mo-oxo species and the framework's aluminum resulted in the formation of Al<sub>2</sub>(MoO<sub>4</sub>)<sub>3</sub>, disrupting the primary framework of the zeolite and causing a rapid decrease in its initial activity<sup>31</sup>.

Beyond Mo/ZSM-5 catalysts, Mo/MCM-22 catalysts, initially synthesized by Mobil Oil Corporation, have shown superior catalytic performance, higher aromatic selectivity, and better catalyst stability<sup>57</sup>. Similar to ZSM-5, MCM-22 zeolite possesses a high internal surface area that facilitates high dispersion of metal active sites. However, MCM-22 differs in its three-dimensional pore structure, which is comprised of a 12-member ring supercage connected by two-dimensional 10-member ring channels, as opposed to ZSM-5's two-dimensional 10-member ring channel system. Consequently, the unique pore architecture and framework composition of MCM-22 zeolite, when combined with molybdenum, afford it a distinctive efficiency for the

direct conversion of methane into more complex hydrocarbons via a nonoxidative pathway.

The effectiveness of Mo/ZSM-5 or Mo/MCM-22 catalysts has been further improved by introducing other metals into the framework as promoters. Additions of promoters like Fe, Mg, Co, Ni, and K have proven beneficial in increasing active sites and reducing coke formation<sup>58</sup>. For instance, when Co and Ni were used as promoters, both Mo-Co/ZSM-5 and Mo-Ni/ZSM-5 catalysts enhanced benzene yield by altering the reducibility and mobility of the active Mo species within the framework. Further suppression of coke formation was achieved through the addition of Fe and K, as found by Bajec et al. and Ramasubramanian et al. This addition weakened the acidity of the zeolite and curtailed the transformation of C<sub>6</sub>H<sub>6</sub> into coke species.

#### *1.5.2.2 Single atom catalysts for NMC*

Single-atom catalysts (SACs), distinguished by their distinct structure of isolated single-atom active sites on supports, provide significant benefits for enhancing catalytic performance. These advantages arise from their well-defined catalytic sites, maximized metal atom utilization, high stability, and enhanced reactivity. In 2014, Bao and colleagues introduced single iron atoms embedded within the lattice of silica (Fe@SiO<sub>2</sub>), which proved to be an extraordinarily efficient catalyst for the non-oxidative conversion of methane to ethylene and benzene<sup>48</sup>. Utilizing a 0.5 wt.% Fe/SiO<sub>2</sub> catalyst, they achieved an impressive 48% conversion of methane, over 99% selectivity for hydrocarbon production (comprising 48% ethylene, 28% benzene, and 24% naphthalene), with a stable performance sustained over 60 hours at 1363 K.

The well-dispersed single Fe atom is depicted as a bright dot in the high-angle annular dark-field scanning transmission electron microscopy (STEM-HAADF) image in Figure X. The XANES and EXAFS spectra of the in-situ Fe/SiO<sub>2</sub> suggest that iron oxide species in the fresh sample interact extensively with the SiO<sub>2</sub> support, embedding within the silica matrix through bonding with Si and C atoms to form an FeC<sub>2</sub>SiO<sub>2</sub> site when exposed to methane above 1173 K. This highly coordinated, isolated active site prevents adjacent C-C coupling on iron nanoparticles and prevents the formation of carbon nanotubes through crystallization. The initial proposed mechanism suggested methane is first adsorbed onto the iron carbide active site, followed by C-H bond activation, the creation of a ·CH<sub>3</sub> radical, and subsequent release of this radical from the surface. The intermediate ·CH<sub>3</sub> radicals then undergo gas phase reactions to form ethane. Further dehydrogenation and cyclization reactions convert ethane to ethylene, benzene, and naphthalene.

Over the past decade, other metal single atom catalysts for NMC reaction were developed by varying the support and metal materials, such as PtSn/SiO<sub>2</sub>, Fe@CRS, Fe@SiO<sub>2</sub>, Fe/SiO<sub>2</sub>-V, and Pt@CeO<sub>2</sub><sup>8,59,60</sup>. Although Fe@SiO<sub>2</sub> remains the superior catalyst for the NMC reaction, it still comes with challenges. The necessity for extremely high temperatures (>1273 K) and an uncontrolled reaction time, which leads to high selectivity of less valuable products, are issues that need to be further optimized and addressed.

#### *1.5.2.3 Semiconductor based catalysts for NMC*

One pathway to improve the efficiency of NMC reaction is the adoption of photocatalytic NMC reaction, as it is a promising green route for nonoxidative methane

conversion under mild conditions and overcomes some of the kinetic and thermodynamic barriers associated with traditional conversion processes. Photoreactions rely on semiconductor catalysts that absorb sufficient photoenergy, thereby exciting electrons to the conduction band and leaving corresponding holes on the valence band<sup>61</sup>. These excited electrons and holes then migrate to the surface of the photocatalysts, facilitating the photoreaction. This process stands out as it can occur even at room temperature and ambient pressure; the photoenergy provides the necessary activation energy for the reaction to take place. In essence, photoexcitation replaces the need for heat in overcoming the reaction's activation energy. Furthermore, the selection of optimal photocatalysts and reaction pathways can significantly lower the required activation energy.

Semiconductor materials such as TiO<sub>2</sub>, MgO, Ce, Ga, Ga<sub>2</sub>O<sub>3</sub> and ZnO have been studied as support material or active species for photocatalytic NMC reactions<sup>62,63</sup>. It is worth to note Li et al was able to synthesize (Zn, Zn<sup>2+</sup>)-ZSM-5 catalyst to achieve 9.8 μmol h<sup>-1</sup> conversion rate and 99.6% selectivity of ethane under 150W high-pressure Hg lamp<sup>64</sup>. The proposed reaction mechanism indicates that the 4s electron of Zn<sup>+</sup> is excited and transfers to the empty C–H antibonding orbital for C–H activation. Nevertheless, the low conversion remains as the main challenge for photocatalytic NMC to achieve scale-up and economic viability.

### *1.5.3 Autothermal Reactor for NMC reaction*

The enhancement of the NMC reaction can be achieved through an innovative multifunctional reactor design approach: the autothermal reactor. This system capitalizes on the symbiosis between chemical reactions and specific heat addition or

removal within a single apparatus. This unifying approach circumvents the need for a sequence of separate operations typically needed for mixing, heat transfer, reaction, separation, etc.

Autothermal reactors are typically designed for the systematic exploitation of exothermic and endothermic reaction coupling, aiming to achieve adiabatic autothermal operation<sup>65,66</sup>. For instance, previous research explored the use of a millisecond catalytic wall reactor for the NMC reaction, demonstrating a proof-of-concept simulation<sup>49</sup>. This approach showed that periodic swapping between NMC and coke combustion on opposite sides could achieve autothermal operation while maintaining 25% methane conversion and less than 10% coke selectivity over 100 hours of operation.

Furthermore, the development of a heat-exchange hydrogen-permeable membrane reactor for the NMC reaction has shown potential in enabling autothermal operation<sup>67</sup>. The mixed ionic-electronic conducting (MIEC)  $\text{SrCe}_{0.7}\text{Zr}_{0.2}\text{Eu}_{0.1}\text{O}_{3-\delta}$  ceramic membrane facilitates hydrogen transport and oxygen transport driven by the partial pressure difference between the sweep side and the reaction side. This setup aids in achieving higher methane conversion with hydrogen removal, following Le Chatelier's principle, and burning the permeated hydrogen provides heat for the endothermic NMC reaction. Moreover, the membrane generally operates above 873 K, making it compatible with the NMC catalyst, Fe/SiO<sub>2</sub>.

Although the MIEC membrane has demonstrated its ability to couple exothermic hydrogen combustion with endothermic NMC reaction and achieve autothermal operation under adiabatic conditions, the energy from combustion was

found to be insignificant compared to the heat provided by the electric furnace. This deficiency is due to the heat losses to the environment, and it prevents the membrane reactor system from maintaining the required reaction temperature without external heating. Thus, the realization of a truly autothermal reactor for the NMC reaction and understanding the impact of genuine autothermal operation remain open challenges. Further investigations are essential to improve the overall NMC reaction performance.

#### *1.5.4 Electrified Reactor for NMC reaction*

Bulk chemical production methods typically rely on continuous high-temperature operations. Electrification of traditionally fired chemical reactors could significantly aid in the global objective of decarbonization, mitigating the environmental impact of burning fossil fuels while facilitating flexible and more efficient heat generation.

Traditional gas burners serve to distribute heat among the reactor tubes. However, a significant drawback is the heat boundary layer, which necessitates substantially higher external combustion temperatures to achieve the desired reactor temperature, leading to poor heat transfer efficiency. Moreover, limited thermal conductivity across the reactor wall and internal catalysts can create steep temperature gradients across the catalyst, resulting in suboptimal catalyst utilization.

Recently, researchers have started exploring the conversion of electrical power into chemical potential as a method to activate methane. Notable work in electrified methane conversion has showcased a compact electrified system for steam reforming of methane, aimed at hydrogen production. In this work, FeCrAl alloy resistant heating elements were coated with a Ni-based catalytic washcoat to achieve exceptional

performance (>85% Conversion) utilizing renewable energy sources<sup>68</sup>. The underlying principle involves the transformation of electricity into heat through Joule heating, enhancing heat transfer efficiency and providing uniform heating from the source to the catalyst. Moreover, the elimination of external heating equipment allows for a significant reduction in the reactor system size. However, challenges such as catalyst deactivation due to coke formation and overall system stability persist.

An alternative approach involves the use of microwave-heated reactors (MWR), which transform electrical power into heat via radiation absorption. MWR reactors can selectively heat only the susceptor, a support for the catalyst that absorbs electromagnetic energy, thus improving product selectivity by avoiding unnecessary feedstock gas heating. Notably, these susceptors are often composed of carbon and SiC due to their high heating efficiencies. Experiments using MWR for dry reforming methane have shown promising results, with methane conversion rates reaching up to 91% at 900 °C with optimized C-SiO<sub>2</sub> catalyst<sup>69</sup>. These results surpass the equilibrium conversion, suggesting that microwave selective heating both enhances dry reforming performance and curbs secondary gas-phase reactions. Nonetheless, the reaction may still foster the formation of carbonaceous species at higher reaction temperatures.

Despite these advancements, electrified studies of the NMC reaction remain limited. Application of electrified NMC reactions could potentially enhance catalyst efficiency and reveal new C1 chemistry routes, improving overall reaction performance and reducing coke formation. Thus, there's a clear avenue for future research in this exciting and promising field.

## *1.6 Thesis Overview*

This dissertation is meticulously structured into five distinct chapters. Chapter 1 provides a comprehensive review of existing technologies for methane utilization, thereby emphasizing the need and impetus for my research into the creation of novel catalysts and reactor systems for direct nonoxidative methane conversion. It also delivers an in-depth discourse on the development of specially designed catalysts and reactor systems for nonoxidative methane conversion.

Chapter 2 delves into the complex interplay between the membrane material, SCZO, and the NMC catalyst, Fe/SiO<sub>2</sub>. It discusses how these interactions guide the reaction pathways in the NMC process, elucidating the integral roles these components play in optimizing reaction efficiency and product distribution.

In Chapter 3, an innovative self-sustaining reactor designed for the NMC reaction is presented. This reactor exploits autothermal operation to achieve tunable product selectivity by linking the endothermic NMC reaction with an exothermic oxidation reaction. The observed high hydrocarbon yield and minimal coke formation illustrate the potential of this approach for industrial application.

Chapter 4 elucidates the mechanisms of the NMC reaction over an Fe/SiO<sub>2</sub> catalyst. The studies utilize a custom-made mass spectrometer system to investigate the local concentration and temperature profiles within the reactor system, providing crucial insights into the NMC reaction dynamics.

Chapter 5 introduces a groundbreaking method for non-equilibrium, continuous chemical synthesis. By harnessing electrified pulsed heating and rapid cooling, this

strategy achieves high C<sub>2</sub> selectivity and energy efficiency in the NMC reaction, marking a significant advance in methane conversion methodologies.

The final chapter encapsulates the pivotal findings from each chapter, providing a consolidated overview of the significant outcomes of this research. Moreover, it lays the groundwork for potential future directions for these projects, inviting further discourse on next steps and additional exploration avenues in the field of the NMC process.

## Chapter 2: Understanding the Impact of Hydrogen Activation by SrCe<sub>0.8</sub>Zr<sub>0.2</sub>O<sub>3-δ</sub> Perovskite Membrane Material on Direct Non-Oxidative Methane Conversion

(Reproduced from Sichao Cheng\*, Su Cheun Oh\*, Mann Sakbodin, Limei Qiu, Yuxia Diao & Dongxia Liu. Understanding impact of hydrogen activation by SrCe<sub>0.8</sub>Zr<sub>0.2</sub>O<sub>3-δ</sub> perovskite membrane material on direct non-oxidative methane conversion. *Frontiers in Chemistry*, 2021, 9, 1119. doi: 0.3389/fchem.2021.806464.)

### *2.1 Introduction*

As mentioned in chapter 1, NMC has received intense attention in the past decades since it directly converts methane into value-added hydrocarbons such as ethylene (C<sub>2</sub>H<sub>4</sub>) and benzene (C<sub>6</sub>H<sub>6</sub>), and hydrogen (H<sub>2</sub>) co-product<sup>15,30,42,45</sup>. However, there are inherent challenges in the NMC reaction such as low thermodynamic equilibrium conversion and catalyst deactivation due to the reaction endothermicity and coke deposition, respectively<sup>70</sup>. A strategy to increase methane conversion in NMC is to conduct the reaction in a hydrogen-permeable membrane reactor<sup>49,71</sup>. H<sub>2</sub> is the smallest molecule in NMC reaction, and its yield reaches up to ~50% in the product effluent, which directly influences the kinetics and thermodynamics of the reaction. According to the Le Chatelier's principle, the removal of hydrogen produced in NMC can shift the thermodynamic equilibrium to higher methane conversion. Membrane reactors comprised of methane activation catalysts and H<sub>2</sub>-permeable membranes, therefore, have been intensively studied since the 1990s<sup>64,72,73</sup>.

Given the reaction temperature (typically, > 873 K) of NMC, research has been focusing on thermally and chemically stable metal and ceramic membrane materials integrated with molybdenum/zeolite (e.g., Mo/ZSM-5)<sup>74</sup> or iron/silica (Fe/SiO<sub>2</sub>)<sup>48</sup> catalysts in membrane reactor studies. For example, Larachi's group had developed a

palladium-silver (Pd-Ag) alloy membrane on porous stainless steel support for direct NMC over a zeolite supported ruthenium-molybdenum (i.e., Ru-Mo/ZSM-5) catalyst at temperatures up to 973 K<sup>54</sup>. The catalytic performance tests showed that the Pd-alloy membrane was effective in hydrogen permeation and resulted in a significant increase in methane conversion. Similarly, Morreale and co-workers had fabricated the Pd membranes containing packed Mo/ZSM-5 catalyst for NMC<sup>75</sup> to achieve significant improvement in methane conversion and total aromatics yield through in-situ H<sub>2</sub> removal. For ceramic membrane reactors for NMC, perovskites-based metal oxides that have mixed ionic-electronic conductivity (MIEC) were used as membrane materials in NMC. For instance, Iglesia's group had manufactured supported SrCe<sub>0.95</sub>Yb<sub>0.05</sub>O<sub>3-δ</sub> thin membrane for NMC over the Mo/ZSM-5 catalyst<sup>45</sup>. The reactor demonstrated a slight increase in methane conversion due to H<sub>2</sub> removal<sup>76,77</sup>. It should be noted that all these studies were based on the metal/zeolite catalyst systems which yielded a higher amount of coke and accelerated catalyst deactivation in the membrane reactor tests.

Our group has recently developed a H<sub>2</sub>-permeable SrCe<sub>0.8</sub>Zr<sub>0.2</sub>O<sub>3-δ</sub> (SCZO) perovskite-based membrane reactor for NMC over the Fe/SiO<sub>2</sub> catalyst, which exhibited significantly higher stability and activity than the membrane reactors packed with the traditional Mo/ZSM-5 catalyst<sup>4</sup>. The SCZO-based membrane reactor also achieved high methane conversion and long-term stability and was chemically and thermally stable at high temperature conditions of Fe/SiO<sub>2</sub> catalyst functioning when NMC was coupled with either hydrogen combustion or reverse water gas shift reaction<sup>67,78</sup>. As expected, the products were shifted to heavier hydrocarbons such as

naphthalene when the NMC was run in the SCZO-based membrane reactor for hydrogen removal. Moreover, we studied the addition of H<sub>2</sub> into the reaction zone via the SCZO membrane by flowing H<sub>2</sub> sweep in the membrane reactor<sup>79</sup>. It shows higher methane conversion than the fixed-bed reactor setting, besides the product selectivity was modulated to lighter hydrocarbons. Clearly, we achieved the tuning of the product selectivity towards to lighter hydrocarbons without sacrificing the methane conversion, which was distinct from all previous H<sub>2</sub> co-feed studies in the fixed-bed reactor conditions in literature.

Inspired by the tailorability of product selectivity without sacrifice of methane conversion in NMC in membrane reactors by H<sub>2</sub> addition into the reaction zone via H<sub>2</sub>-permeable SCZO perovskite, we aimed to provide mechanistic understanding of the impacts of hydrogen addition on NMC in the presence of the H<sub>2</sub>-permeable membrane and methane activation catalyst materials. Hydrogen is the co-product of dehydrogenation of alkane, whose presence impacts both the reaction kinetics and thermodynamics of NMC. Studies for NMC in the fix-bed reactors have shown that addition of a significant amount of hydrogen co-feed would reduce methane conversion while a small amount would have favorable effect in terms of catalyst stability and lighter hydrocarbon production<sup>58,80-84</sup>. For example, it was proposed that 3%-6% of H<sub>2</sub> suppressed coke deposition on a 6 wt. % Mo/HZSM-5 catalyst in a NMC reaction<sup>58,83,85</sup>. In the MIEC ceramic membranes, hydrogen is permeated electrochemically<sup>86-88</sup>. First, hydrogen is dissociated, and ionized to form the hydroxide defects (proton defects), which migrates through the membrane via proton hopping between adjacent oxygen ions at normal lattice sites. At the permeate side of the

membrane, the defects are then reduced to form hydrogen molecules and desorbed from the membrane surface. The formation of hydrogen species upon activation in the SCZO material is expected to influence the NMC in a different manner than that of H<sub>2</sub> co-feed in NMC without the MIEC materials.

In Chapter 2, we report the performance of NMC over the SCZO perovskite oxide, Fe/SiO<sub>2</sub> catalyst, and a mixture of both SCZO oxide and Fe/SiO<sub>2</sub> catalyst in the absence and presence of H<sub>2</sub> co-feed in methane stream, respectively. The methane conversion, product selectivity and coke formation in all these cases were evaluated and compared. In addition, the properties of coke formed on SCZO membrane, Fe/SiO<sub>2</sub> catalyst and their mixture were analyzed using the Raman spectroscopy, X-ray photoelectron spectroscopy (XPS) and temperature programmed oxidation (TPO) techniques. The present study rigorously analyzed the impact of H<sub>2</sub> activation by H<sub>2</sub>-permeable SCZO perovskite oxide on methane activation catalysts in NMC, a topic that has been rarely explored in H<sub>2</sub>-permeable membrane reactor literature in past years.

## 2.2 *Experiments*

### 2.2.1 *Synthesis of membrane and catalyst material*

The SCZO perovskite oxide material was prepared by a conventional solid-state synthesis method<sup>4</sup>. In the synthesis process, stoichiometric amounts of strontium carbonate (SrCO<sub>3</sub>, ≥99.9% purity, Sigma-Aldrich), cerium oxide (CeO<sub>2</sub>, 99.9% purity, Alfa Aesar) and zirconium oxide (ZrO<sub>2</sub>, 99.9% purity, Inframat) were ball-milled to ensure even mixing of the starting chemicals. In order to obtain homogeneous solution in the ball milling process, ethanol (200 proof, Pharmco) and milling media (yttria-

stabilized zirconia) were adequately added. The resultant slurry was ball milled for 24 hours, followed by drying and grinding into fine powder, and then calcination at 1573 K for 10 hours. The as-obtained material was  $\text{SrCe}_{0.8}\text{Zr}_{0.2}\text{O}_{3-\delta}$  perovskite ceramic powder, abbreviated as SCZO, and was directly used in the catalysis tests.

The Fe/SiO<sub>2</sub> catalyst material was prepared by fusing iron silicate (Fe<sub>2</sub>SiO<sub>4</sub>) and quartz particles (SiO<sub>2</sub>, BDH) at 1973 K for 6 hours in stagnant air in a high temperature furnace (MTI Corporation KSL1700X), as reported in our previous work<sup>4</sup>. The iron silicate was synthesized in the lab following a reported procedure<sup>89</sup>. Before the fusing process, the Fe<sub>2</sub>SiO<sub>4</sub> and quartz particles were mixed and ball milled for 12 hours. After cooling to room temperature, the resultant product was crushed and sieved to 40-80 mesh.

### 2.2.2 *Material characterization*

The morphologies of the SCZO and Fe/SiO<sub>2</sub> samples were visualized using scanning electron microscopy (SEM) on a Hitachi SU-70 electron microscope. N<sub>2</sub> adsorption-desorption isotherms of both samples were measured using an Autosorb-iQ analyzer (Quantachrome Instruments) at 77 K. The samples were outgassed at 523 K for 8 hours and 1 mm Hg prior to measurements. The specific surface areas of the samples were determined using Brunauer, Emmett and Teller (BET) method. The crystalline phases were examined using powder X-ray diffraction (XRD) and obtained on Bruker D8 Advance Lynx Powder Diffractometer (LynxEye PSD detector, sealed tube, Cu K $\alpha$  radiation with Ni  $\beta$ -filter). The Raman spectra of the coked samples after NMC reactions with different H<sub>2</sub> co-feed for time on stream (TOS) of 2 hours were collected with a Raman spectrometer (LabRAM Aramis, Horiba Scientific) in the range

of 200–2000  $\text{cm}^{-1}$ . X-ray photoelectron spectroscopy (XPS, ESCALAB 250 Microprobe, Thermo Fisher Scientific) was performed to measure the bonding environment of elements in the fresh and spent SCZO and Fe/SiO<sub>2</sub> samples.

H<sub>2</sub>-temperature programmed desorption (H<sub>2</sub>-TPD) was performed to determine the H<sub>2</sub> adsorption on the used perovskite oxide and methane activation catalyst samples. The H<sub>2</sub>-TPD was evaluated using an AutosorbQ unit (Quantachrome, ASIQM0000-4) equipped with a thermal conductivity detector (TCD). Typically, 100 mg of catalyst sample was loaded into a quartz reactor and pretreated at 973 K for 2 hours under He flow (40 mL min<sup>-1</sup>, ultrapure, Airgas) at a heating rate of 10 K min<sup>-1</sup> from ambient temperature. The sample was then exposed to H<sub>2</sub> stream (5% H<sub>2</sub> in nitrogen, 40 mL min<sup>-1</sup>, ultrapure, Airgas) for 0.5 hours after being cooled to 363 K under He stream. The physisorbed H<sub>2</sub> was removed by flowing He gas (40 mL min<sup>-1</sup>) for 2 hours. Next, the sample was ramped to 1223 K at a ramp rate of 10 K min, and the H<sub>2</sub>-TPD profile was recorded during this step.

The temperature-programmed oxidation (TPO) of the spent SCZO and Fe/SiO<sub>2</sub> samples were acquired using a mass spectrometer (MS, Ametek Proline). In the TPO experiment, 70 mg of spent sample was loaded in a U-shaped tubular quartz reactor (10 mm inner diameter) in which the reactor was placed inside a temperature-controlled furnace (National Electric Furnace FA120 type). The temperature of the furnace was controlled by a Watlow Controller (96 series). A K-type thermocouple was attached to the outer wall of the reactor to monitor the temperature of the catalyst environment. The temperature was increased linearly from room temperature to 1173 K at a ramp rate of 10 K min<sup>-1</sup> and was held constant for 30 min at the final temperature. A mixture

of O<sub>2</sub>/He (30 mL min<sup>-1</sup>; 2% O<sub>2</sub> and 98% He; Airgas) was introduced by He and sent via heated transfer lines hold at 343 K to the reactor during ramping process. The carbon monoxide (CO) and carbon dioxide (CO<sub>2</sub>) effluents as a function of temperature were analyzed using the mass spectrometer to obtain the TPO profiles.

### 2.2.3 *Catalytic NMC reactions*

The NMC catalytic reaction was performed using the same reactor setup as that for TPO, except that the effluents were analyzed using a gas chromatograph (Agilent Technologies, 6890N) equipped with a ShinCarbon ST packed column connected to a thermal conductivity detector (TCD) and a DB-WAX column connected to a flame ionization detector (FID). The NMC reactions were carried out at 1273 K and 1 atm pressure. The performance of NMC on the mixture of SCZO perovskite oxide and Fe/SiO<sub>2</sub> catalyst were measured by arranging 0.375 g of Fe/SiO<sub>2</sub> and 0.1875 g of SCZO powder samples in three different ways in the fixed-bed reactor: (i) SCZO oxide on top of the Fe/SiO<sub>2</sub> catalyst, (ii) SCZO oxide at the bottom of the Fe/SiO<sub>2</sub> catalyst and (iii) well mixing of SCZO oxide and Fe/SiO<sub>2</sub> catalyst. CH<sub>4</sub> (18 mL min<sup>-1</sup>, 99.999% purity, Airgas) diluted in N<sub>2</sub> (as internal standard) (2 mL min<sup>-1</sup>, 99.95% purity, Airgas) were fed to the reactor via heated transfer lines to avoid aromatics condensation. The effects of H<sub>2</sub> addition on NMC over the SCZO, Fe/SiO<sub>2</sub> and their mixture were also investigated by introducing varied H<sub>2</sub> concentrations to the methane feed stream.

## 2.3 Results and discussion

### 2.3.1 Physicochemical properties of SCZO perovskite and Fe/SiO<sub>2</sub> catalyst

The morphologies of both SCZO perovskite oxide and Fe/SiO<sub>2</sub> catalyst materials were examined by SEM observations. Figure 2.1(A)-(B) show that both materials contain irregular shaped particles, while the particle size of Fe/SiO<sub>2</sub> catalyst is ~300 times larger than the SCZO material. The average particle sizes of Fe/SiO<sub>2</sub> and SCZO particles are ~300 μm and ~1 μm, respectively. The crystalline phases of both materials were indicated by XRD data in Figure 2.1(C). The diffraction peaks of Fe/SiO<sub>2</sub> sample are characteristic of cristobalite phase. No XRD peaks related to iron species were identified. The SCZO oxide has the orthorhombic perovskite structure. No secondary phase in this perovskite material was observed. Figure 2.1(D) shows the surface area of both materials. The Brunauer–Emmett–Teller (BET) surface areas of Fe/SiO<sub>2</sub> catalyst and SCZO oxide are 0.38 m<sup>2</sup> g<sup>-1</sup> and 1.01 m<sup>2</sup> g<sup>-1</sup>, respectively. Both materials have low surface areas.

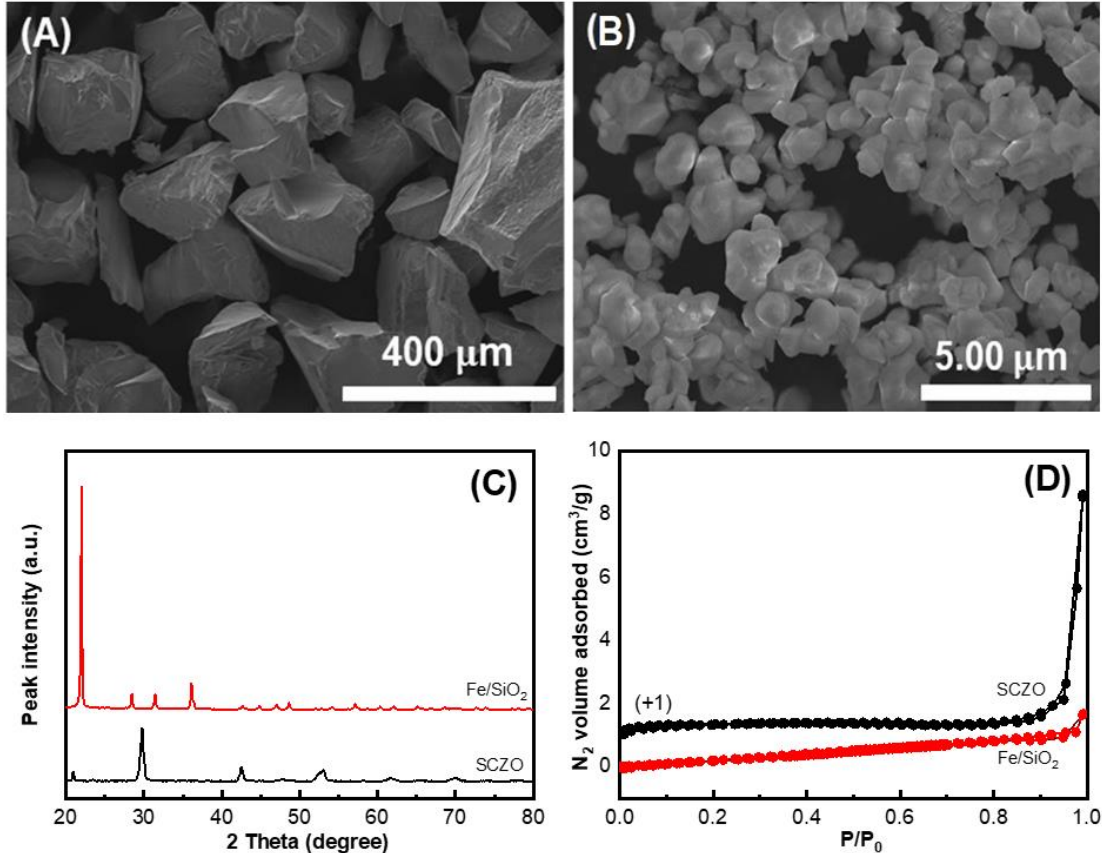


**Figure 2.1.** SEM images showing morphologies of Fe/SiO<sub>2</sub> catalyst (A) and SCZO perovskite oxide (B) particles. (C) and (D) are the XRD data and N<sub>2</sub> adsorption-desorption isotherms of both materials.

The hydrogen adsorption and oxygen coordination environment in both SCZO perovskite and Fe/SiO<sub>2</sub> catalyst materials were characterized by H<sub>2</sub>-TPD and XPS measurements. As shown in Figure 2.2(A), the H<sub>2</sub>-TPD peaks of SCZO oxide sample are more pronounced than those of Fe/SiO<sub>2</sub> catalyst. The four peaks at ~702, ~833, ~1042 and ~1113 K stand for different H<sub>2</sub> desorption states at a broad range of temperatures in the MIEC ceramic. In contrast, only high temperature H<sub>2</sub>-desorption peaks (i.e., 912 and 1128 K) appear in the Fe/SiO<sub>2</sub> catalyst. The XPS data in Figure 2.2(B) show that the fresh Fe/SiO<sub>2</sub> catalyst exhibits an O1s XPS peak centered at 533.0 eV that can be assigned to the Si-O-Si structure in the quartz support.<sup>90,91</sup> The shoulder

peak at 531.9 eV can be assigned to the oxygen bonded in the organic C-O structures.<sup>92</sup> In the SCZO perovskite, two obvious O1s peaks at 531.4 eV and 527.1 eV were observed, which can be caused by the O<sup>2-</sup> and O<sup>1-</sup> ions in the SCZO perovskite oxide, respectively.<sup>93,94</sup> The lower binding energies of oxygen species in the O1s XPS of SCZO oxide material than that of Fe/SiO<sub>2</sub> indicates that the SCZO perovskite can be easily reduced compared to the Fe/SiO<sub>2</sub> catalyst in the NMC reaction conditions.

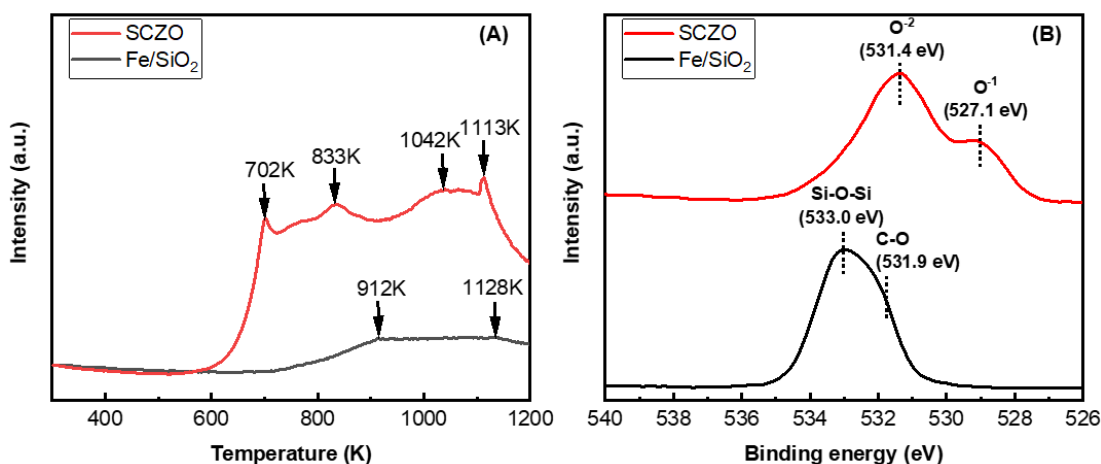


**Figure 2.2.** H<sub>2</sub>-TPD profiles (A) and XPS spectra of O1s photoelectron lines (B) of Fe/SiO<sub>2</sub> catalyst and SCZO perovskite oxide materials.

### 2.3.2 *NMC in the absence of H<sub>2</sub> co-feed in methane stream*

For NMC in the membrane reactor that is made of H<sub>2</sub>-permeable SCZO oxide membrane tube packed with Fe/SiO<sub>2</sub> catalyst in the presence of H<sub>2</sub> sweep gas, a slight increase in methane conversion, tuning product selectivity towards lighter hydrocarbons and absence of catalyst deactivation were observed, as reported in our previous work<sup>4</sup>. The purpose of this study is to reveal the mechanism of this unique property of the H<sub>2</sub>-permeable membrane reactor for NMC. In order to mimic the fact of co-existence of SCZO, Fe/SiO<sub>2</sub> and H<sub>2</sub> co-feed factors in the membrane reactor operation conditions, we used the fixed-bed reactor settings in this work to study the

performance of NMC over Fe/SiO<sub>2</sub>, SCZO oxide, the combination of both, and then integration of these three factors in sequence.

#### 2.3.2.1 NMC over Fe/SiO<sub>2</sub> catalyst or SCZO oxide

The performance of Fe/SiO<sub>2</sub> or SCZO material in the NMC reaction with pure methane feed stream was the first to be studied. Figure 2.3 showed that the methane conversion and product selectivity versus the time-on-stream (ToS) of 10 hours in both materials. In Figure 2.3(A), NMC over Fe/SiO<sub>2</sub> catalyst showed stable methane conversion with no obvious deactivation during the test, in which methane conversion remained at ~10% with C<sub>2+</sub> selectivity > 90%. There was ~10% coke formed, but the reaction was independent of coke formation, and maintained stable performance, similar to our previous study<sup>4</sup>. The SCZO material, however, exhibited deactivation over the course of 10-hour ToS, as shown in Figure 2.3(B). Methane conversion was high initially (~13%), but slowly decreased to ~5% after 10 hours of reaction. Coke formation, on the other hand, increased over time, while aromatics products decreased. Up to ~60% coke selectivity was observed at ToS of 10 hours in NMC over the SCZO oxide.

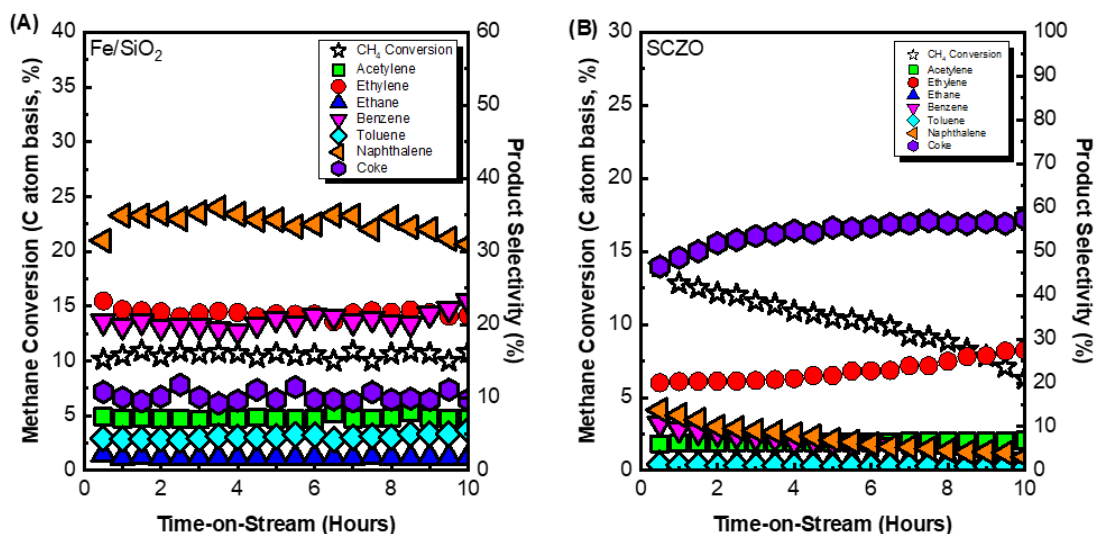


**Figure 2.3.** CH<sub>4</sub> conversion and product selectivity of NMC over Fe/SiO<sub>2</sub> catalyst (A) and SCZO perovskite oxide (B) materials. (1273 K temperature, 101.325 kPa pressure, 3200 mLg<sup>-1</sup>h<sup>-1</sup> space velocity, molar ratio of N<sub>2</sub>/CH<sub>4</sub> = 1/9, N<sub>2</sub> used as internal standard).

The NMC at the studied conditions involved a complex heterogeneous and homogeneous reaction network.<sup>95,96</sup> The mechanistic investigation into the Fe/SiO<sub>2</sub> catalyst revealed that the silica lattice-confined Fe sites initiated CH<sub>4</sub> dehydrogenation to generate methyl and hydrogen species, enabling a series of subsequent surface and gas-phase reactions to form dehydrogenated and cyclized large hydrocarbon products. The performance of NMC over the Fe/SiO<sub>2</sub> catalyst in this study was consistent with our previous work. Although coke was formed in the reaction, the steady state performance data in Figure 2.3(A) suggested that a homogeneous gas phase reaction might play a dominant role after NMC initiation by the heterogeneous catalyst surface. In the SCZO oxide, the high methane conversion at the initial stage of the reaction (e.g., ToS < 2h) suggested its effectiveness in initiating the methane activation. The high coke selectivity, however, hinted that the catalyst was not effective in suppressing the dehydrogenation of the hydrocarbon intermediates or products, thus causing coke

formation. The carbonaceous deposits were detrimental to the SCZO because of the blocked active sites on the SCZO, and eventually led to catalyst deactivation, as shown in Figure 2.3(B).

#### 2.3.2.2 NMC over a mixture of Fe/SiO<sub>2</sub> catalyst and SCZO oxide

To understand the NMC performance in the membrane reactor that had SCZO membrane tube packed with Fe/SiO<sub>2</sub> catalyst internally, the SCZO oxide and Fe/SiO<sub>2</sub> catalyst samples were arranged in three different manners in the fixed-bed reactor to mimic H<sub>2</sub>-permeable membrane reactor setup for NMC. As described in Section 2.3, the layer of SCZO oxide was placed on the top, bottom or evenly distributed in the Fe/SiO<sub>2</sub> catalyst layer, respectively. Figure 2.4(A) shows the methane conversion and product selectivity when SCZO oxide was placed on top and at the bottom of the Fe/SiO<sub>2</sub> catalyst, as well as when both SCZO and Fe/SiO<sub>2</sub> powder were mixed, for ToS of 3.5 hours. The overall methane conversion was slightly lower when SCZO was placed on top of the Fe/SiO<sub>2</sub> layer compared to when SCZO was placed at the bottom of the Fe/SiO<sub>2</sub> layer. Methane conversion was lower in the first case because methane reacted with the SCZO material first before reaching Fe/SiO<sub>2</sub> catalyst. As discussed above, the SCZO material promoted coke formation more easily than Fe/SiO<sub>2</sub> powder. Therefore, coke formed on the SCZO material tended to block the active sites on the Fe/SiO<sub>2</sub> catalyst located at the bottom layer and reduced methane activation from both layers. In terms of product selectivity, ethylene and acetylene selectivity were higher when SCZO was arranged at the top layer. Since methane reacted on SCZO material through surface reaction, the dehydrogenation of methane on the surface formed not only coke but also C<sub>2</sub> products. Aromatic products were proposed to form in the gas

phase homogeneously through a series of cyclization reactions. The aromatic selectivity was lower in the case when SCZO was placed at the top layer because less methane was reacted with Fe/SiO<sub>2</sub> catalyst to form reaction intermediates for gas phase cyclization reactions.

When SCZO was placed at the bottom of the Fe/SiO<sub>2</sub> catalyst, the overall methane conversion and coke selectivity were higher. As shown in Figure 2.4(B), Fe/SiO<sub>2</sub> catalyst did not show significant deactivation over the course of 10-hour reaction. Therefore, when methane reacted with the Fe/SiO<sub>2</sub> catalyst layer first, C<sub>2</sub> and higher products were formed through both surface and gas-phase reactions. However, when these products (including C<sub>2</sub> and aromatics) encountered the SCZO layer at the bottom, they underwent surface reactions on the SCZO oxide to form coke even though methane continued to react at the top Fe/SiO<sub>2</sub> layer. The higher coke selectivity and lower C<sub>2</sub> and higher hydrocarbon selectivity in such SCZO and Fe/SiO<sub>2</sub> sample arrangement verify the proposed surface kinetics of SCZO, and both surface and gas phase kinetics of Fe/SiO<sub>2</sub> catalyst. In addition, comparing both catalyst arrangements in Figures 5.4(A) and (B), methane deactivated faster when the SCZO material was located on the top layer. As explained earlier, methane reacted with SCZO first to form coke, which in turn led to catalyst deactivation. As for the case when both SCZO and Fe/SiO<sub>2</sub> powder were physically well mixed as shown in Figure 2.4(C), methane conversion showed only very slight deactivation from ~11% to ~9.5% over the course of 3.5 hours. Coke selectivity also increased at a slower rate compared to the previous two cases. Such catalyst arrangement allowed methane to react with SCZO and Fe/SiO<sub>2</sub> powder at the same probability. The coke formed through surface reaction on SCZO

material again blocked the active sites of the Fe/SiO<sub>2</sub> catalyst, causing slight deactivation on the overall methane conversion. Overall, a synergetic interaction between these two materials in close proximity has led to more stable NMC performance compared to the other two arrangement modes of SCZO and Fe/SiO<sub>2</sub> materials.

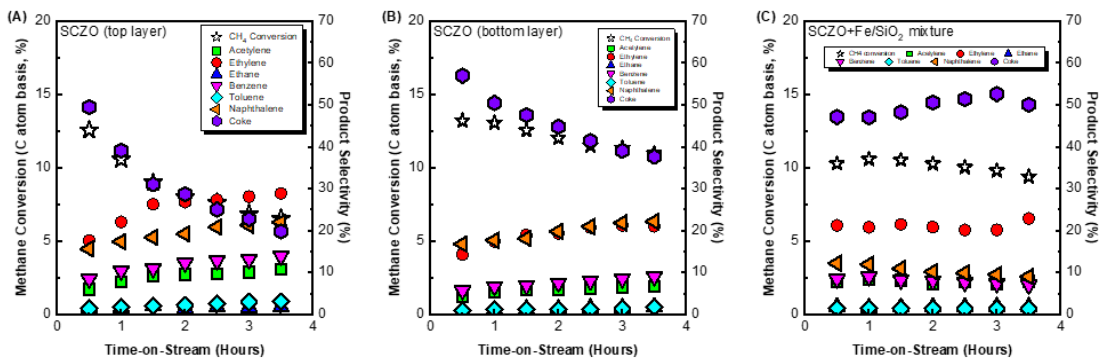


**Figure 2.4.** CH<sub>4</sub> conversion and product selectivity in NMC reaction over Fe/SiO<sub>2</sub> catalyst and SCZO perovskite oxide mixture with different sample arrangement format in the reactor: (A) SCZO packed on top of Fe/SiO<sub>2</sub>, (B) SCZO packed below Fe/SiO<sub>2</sub>, and (C) SCZO and Fe/SiO<sub>2</sub> well mixed. (Mass ratio of SCZO to Fe/SiO<sub>2</sub> = 1:2, 1273 K temperature, 101.325 kPa pressure, 2133 mLg<sup>-1</sup>h<sup>-1</sup> space velocity, molar ratio of N<sub>2</sub>/CH<sub>4</sub> = 1/9, N<sub>2</sub> used as internal standard).

### 2.3.3 *NMC in the absence of H<sub>2</sub> co-feed in methane stream*

#### 2.3.3.1 *NMC over Fe/SiO<sub>2</sub> catalyst or SCZO oxide with H<sub>2</sub> co-feed*

To understand the effects of H<sub>2</sub> sweep gas on the NMC in the membrane reactor, the NMC over SCZO oxide or Fe/SiO<sub>2</sub> catalyst in the presence of H<sub>2</sub> co-feed was studied. Figure 2.5 presents the methane conversion and product selectivity in NMC over each of these two materials at different H<sub>2</sub> co-feed concentrations at ToS of 1 hour. Methane conversion over the Fe/SiO<sub>2</sub> catalyst decreased with increasing H<sub>2</sub> co-feed concentration in Figure 2.5(A) due to the reverse reaction of NMC, consistent with Le Chatelier's principle. The product selectivity shifted from heavy aromatics to light

hydrocarbons. The coke formation also decreased. These results are consistent with previous reports on NMC over the metal/zeolite catalysts<sup>97,98</sup>. It should be noted that the degree of methane conversion was dropped significantly with the H<sub>2</sub> co-feed concentration. For example, at 10% of the H<sub>2</sub> co-feed, methane conversion dropped to ~2.5%, about four times lower than that in the absence of H<sub>2</sub> co-feed.

The presence of H<sub>2</sub> co-feed, however, did not show significant detrimental impact on methane conversion in NMC over the SCZO oxide, except that the H<sub>2</sub> co-feed was very high (e.g., 20%) condition. Figure 2.5(B) shows that methane conversion was kept at ~12% when no H<sub>2</sub> was added to the reaction. When H<sub>2</sub> co-feed concentration increased from 5% to 15%, methane conversions were maintained at ~11%. Unlike Fe/SiO<sub>2</sub> catalyst, coke selectivity remained almost the same at around 52%-58% for SCZO material, except for 20% H<sub>2</sub> co-feed concentration where the selectivity dropped more significantly. The C<sub>2</sub> product selectivity, on the other hand, increased slightly with increasing H<sub>2</sub> co-feed concentration. The NMC performance data over these two materials verified that SCZO oxides favored surface reaction by cleaving the C-H bond in methane to form C<sub>2</sub> products and coke, instead of both surface and gas-phase reaction in the case of NMC on the Fe/SiO<sub>2</sub> catalyst. The H<sub>2</sub> co-feed in the reaction system likely did not influence the surface reaction significantly, while it eliminated the gas-phase reaction rapidly during the NMC in the studied conditions.

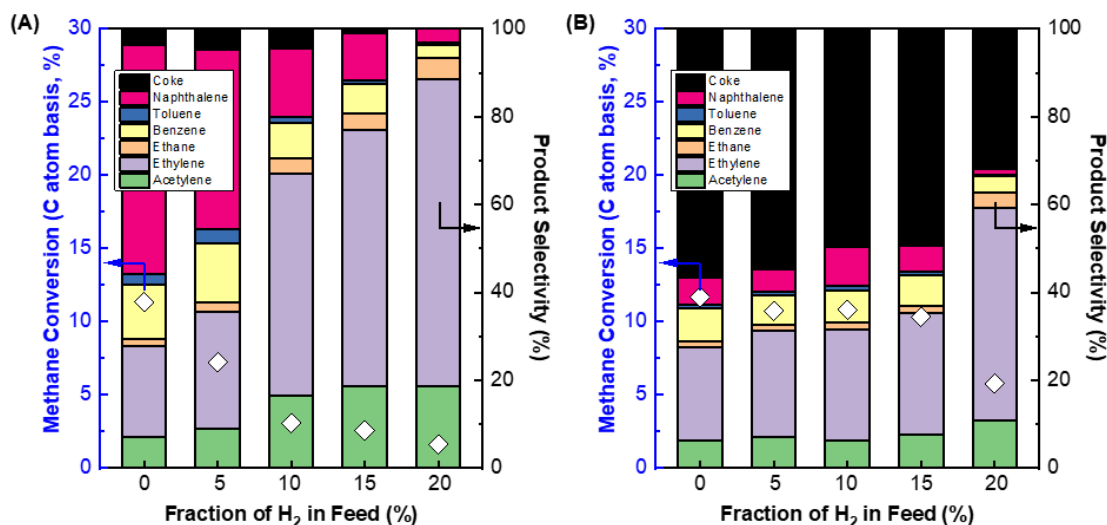


**Figure 2.5.** CH<sub>4</sub> conversion and product selectivity in NMC over Fe/SiO<sub>2</sub> catalyst (A) and SCZO perovskite oxide (B) in a fixed-bed reactor at different hydrogen co-feed concentrations. (1273 K temperature, 101.325 kPa pressure, 3200 mLg<sup>-1</sup>h<sup>-1</sup> space velocity, molar ratio of N<sub>2</sub>/CH<sub>4</sub> = 1/9, N<sub>2</sub> used as internal standard, ToS of 1 hour).

### 2.3.3.2 NMC over a mixture of Fe/SiO<sub>2</sub> catalyst and SCZO oxide with H<sub>2</sub> co-feed

The effects of H<sub>2</sub> co-feed on the catalytic activity and product selectivity of the Fe/SiO<sub>2</sub> catalyst and SCZO oxide materials at three different sample mixing modes were studied. When SCZO oxide stayed on the top of the Fe/SiO<sub>2</sub> catalyst, the methane conversion was ~10%, independent of H<sub>2</sub> concentration until 20% H<sub>2</sub> co-feed in the methane stream was used (Figure 2.6(A)). This result is very similar to the case that only SCZO oxide was used in the reactor as shown in Figure 2.5(B). The coke selectivity decreased slightly with increasing hydrogen concentration. Overall, the coke selectivity was lower compared to the testing condition that only SCZO oxide was used in the reactor. Figure 2.6(B) shows the methane conversion and product selectivity of NMC when SCZO oxide was placed below the Fe/SiO<sub>2</sub> catalyst. Similarly, the addition of H<sub>2</sub> in the methane feed decreased methane conversion and increased light C<sub>2</sub> product selectivity. The coke selectivity was high compared to that in Figure 2.6(A), which

should be caused by the severe secondary and the following on reactions of the products that are formed from the top Fe/SiO<sub>2</sub> catalyst layer. Overall, the presence of SCZO oxide in the reactor maintained stable methane conversion except for the conditions with high H<sub>2</sub> co-feed. At the same time, the usage of SCZO oxide led to high coke selectivity.

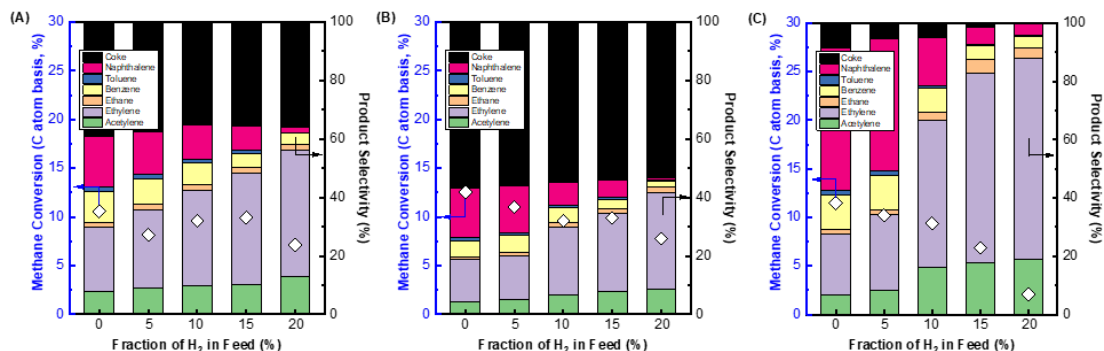


**Figure 2.6.** CH<sub>4</sub> conversion and product selectivity in NMC reaction over Fe/SiO<sub>2</sub> catalyst and SCZO perovskite oxide mixture with different sample arrangement: (A) SCZO packed on top of Fe/SiO<sub>2</sub>, (B) SCZO packed below Fe/SiO<sub>2</sub>, and (C) SCZO and Fe/SiO<sub>2</sub> well mixed. (Mass ratio of SCZO to Fe/SiO<sub>2</sub> = 1:2 in (A) and (B) and 5:95 in (C), 1273 K temperature, 101.325 kPa pressure, 2133 mLg<sup>-1</sup>h<sup>-1</sup> (A) and (B) and 3200 mLg<sup>-1</sup>h<sup>-1</sup> (C) space velocities, molar ratio of N<sub>2</sub>/CH<sub>4</sub> = 1/9, N<sub>2</sub> used as internal standard, ToS of 1 hour).

Figure 2.6(C) showed the NMC performance in the well mixed SCZO oxide and Fe/SiO<sub>2</sub> catalyst samples in the reactor. It should be noted that the amount of SCZO oxide in the Fe/SiO<sub>2</sub> catalyst bed was only 5wt%, about 6.6 times lower than the SCZO amount in the first two mixing modes. The reduction in SCZO oxide usage is based on two considerations. Firstly, SCZO seems to be very active in methane activation that leads to coke formation easily. The lower usage of SCZO is expected to lower the coke formation. Secondly, the 5wt% SCZO oxide has a comparable surface area of SCZO membrane that had contacted with Fe/SiO<sub>2</sub> catalyst in the membrane reactor settings in our previous work (Sakbodin et al., 2016). The surface area ratio between SCZO oxide

and Fe/SiO<sub>2</sub> catalyst in this test was controlled to be the same as that in the membrane reactor condition. In contrast to the previous two SCZO oxide and Fe/SiO<sub>2</sub> catalyst mixing modes, methane conversion dropped gradually from ~11% to ~3% when H<sub>2</sub> co-feed concentration increased from 0% to 20%. Coke selectivity also decreased while heavy aromatics selectivity shifted to lighter hydrocarbons when more H<sub>2</sub> was added to the reaction. However, a closer look showed that methane conversion did not decrease as sharply as the case that only Fe/SiO<sub>2</sub> catalyst was used in Figure 2.5(A). In particular, when H<sub>2</sub> co-feed concentrations were 5 and 10%, high methane conversions and low coke selectivity were reached compared to the sole presence of Fe/SiO<sub>2</sub> catalyst or SCZO oxide. The H<sub>2</sub> co-feed sharply reduced methane conversion on the Fe/SiO<sub>2</sub> catalyst (Figure 2.5(A)), but it mildly decreased methane conversion on the well mixed SCZO oxide and Fe/SiO<sub>2</sub> catalyst mixture (Figure 6(C)). As the MIEC conductor, it is expected that SCZO oxide functions as a “hydrogen transformer” that absorbs co-fed hydrogen and produce activated hydrogen species to reduce coke formation in the NMC on the Fe/SiO<sub>2</sub> catalyst. This function could lower the local hydrogen species concentration that is relevant to the NMC reaction in the reactor, and thus lessens the reverse reaction of NMC according to the La Chatelier’s principle.

#### 2.3.4 Characterization of spent Fe/SiO<sub>2</sub> catalyst and SCZO oxide materials

##### 2.3.4.1 Raman spectroscopy

Raman spectra were measured from spent SCZO, Fe/SiO<sub>2</sub> and their mixture (i.e., 5wt% SCZO in Fe/SiO<sub>2</sub>) materials after ToS of 3.5 h in NMC at different H<sub>2</sub> co-feed concentrations, and the results are shown in Figure 2.7. Nearly no fluorescence

background was detected in all these spectra. The Raman analysis confirmed the existence of two types of carbon structures. The spectra of all the spent catalysts are similar with two observed peaks centered at  $1320\text{ cm}^{-1}$  and  $1600\text{ cm}^{-1}$ , respectively. The band at  $1320\text{ cm}^{-1}$  is assigned to D band while the band at  $1600\text{ cm}^{-1}$  is assigned to G band<sup>99,100</sup>. D band represents disordered graphitic structure, amorphous carbon or polyaromatic type species, while G band relates to graphite involving out-of-phase intra-layer displacement in the graphene structure<sup>101</sup>. There is no significant shift in the two peaks as a function of SCZO oxide usage and  $\text{H}_2$  co-feed concentration.

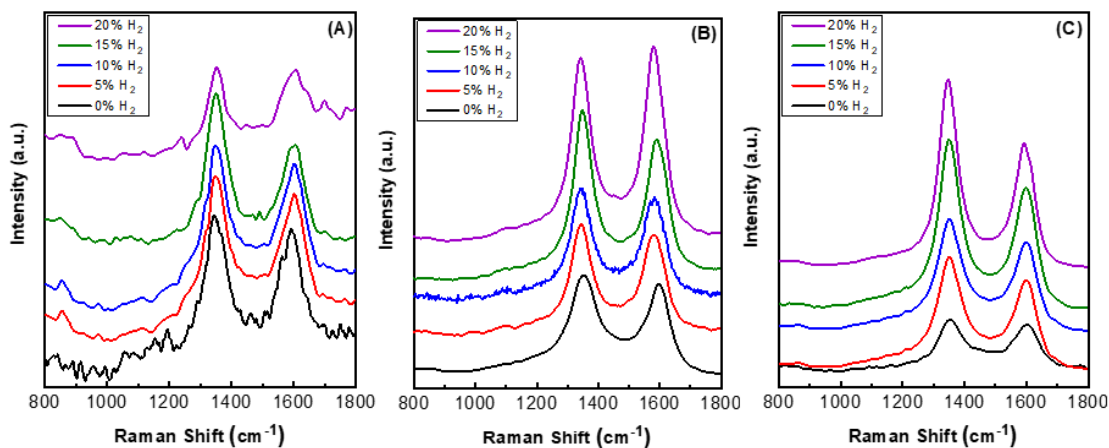


**Figure 2.7.** Raman spectra of coke formed on spent Fe/SiO<sub>2</sub> catalyst (A), SCZO perovskite oxide (B) and Fe/SiO<sub>2</sub> catalyst mixed with 5 wt.% SCZO perovskites (C), respectively, in NMC reaction in a fixed-bed reactor at different hydrogen co-feed concentrations after ToS of 3.5 hr.

Table 5.1 shows the ratio of D band to G band of coke formed on all the samples at different  $\text{H}_2$  co-feed concentration. In the absence of  $\text{H}_2$  co-feed, the ratios are similar among Fe/SiO<sub>2</sub> catalyst, SCZO perovskite oxide, and their mixture. After the addition of  $\text{H}_2$  co-feed, the ratio increased in the Fe/SiO<sub>2</sub> sample, decreased in the SCZO sample, and increased more obviously in the Fe/SiO<sub>2</sub> and SCZO mixture sample, although the ratio did not show obvious dependence on the  $\text{H}_2$  co-feed concentrations in each case.

These results suggested that more coke of ordered graphitic structure was formed on the pure SCZO oxide sample while more coke of amorphous types was formed in the pure Fe/SiO<sub>2</sub> catalyst. The mixing of both materials in the reactor, however, facilitated the formation of amorphous types of coke slightly.

**Table 5.1.** Ratio of D band to G band determined from Raman spectroscopy analysis for Fe/SiO<sub>2</sub> catalyst, SCZO perovskite oxide and 5 wt.% SCZO oxide mixed with 95 wt.% Fe/SiO<sub>2</sub> catalyst after 3.5 hours NMC reaction at 1273 K and at different H<sub>2</sub> co-feed concentrations.

H <sub>2</sub> co-feed (%)	D to G band ratio		
	Fe/SiO <sub>2</sub>	SCZO	5 wt. % SCZO in Fe/SiO <sub>2</sub>
0	1.25	1.30	1.24
5	1.33	1.11	1.37
10	1.39	1.14	1.45
15	1.58	1.21	1.46
20	1.34	0.92	1.59

#### 2.3.4.2 Temperature programmer oxidation (TPO)

TPO of spent SCZO oxide, Fe/SiO<sub>2</sub> catalyst and their mixture in the NMC reactions were measured, and the results were shown in Figure 2.8. The MS signals observed in the TPO profiles include CO<sub>2</sub> and CO; no water signal was detected. Therefore, it was assumed that the coking species on the spent catalysts should be primarily carbonaceous. The CO<sub>2</sub> and CO from the combustion of spent Fe/SiO<sub>2</sub> catalyst displayed relatively narrow TPO profiles (Figures 5.8(A) and (D)), with an onset of 750 K and completion occurring at 1000 K, a span of 250 K. The H<sub>2</sub> co-feed decreased the peak intensity and shifted the peak maximum to lower temperatures. On average, the peak maximum stayed around 860 K. At 20% H<sub>2</sub> co-feed concentration, the sharp decrease in CO<sub>2</sub> peaks was consistent with the sharp decrease in methane

conversion in NMC shown in Figure 2.5(A). For the CO<sub>2</sub> and CO profiles from spent SCZO oxide (Figures 5.8(B) and (E)), both TPO peaks spanning from 670 – 950 K were broadened compared to those of spent Fe/SiO<sub>2</sub> catalyst, and the peak maximum shifted to 800 K in the CO<sub>2</sub> and 760 K in CO profiles. In the CO<sub>2</sub> effluent profiles, a small shoulder peak (centered at 900 K) appeared in the high temperature region. The peak intensity did not reduce obviously with H<sub>2</sub> co-feed until the 20% H<sub>2</sub> concentration was used in the NMC reaction. These results showed that SCZO oxide was more active in methane activation, and it was not influenced by the additional H<sub>2</sub> presence due to its MIEC property. For coking species on the spent SCZO oxide and Fe/SiO<sub>2</sub> mixture sample, the TPO profiles (Figures 5.8(C) and (F)) seem to be the sum of profiles of the two individual materials. The peak spanned broadly from 650 to 1000 K, and the peak maximum stayed at 770 K with very clear shoulder peaks at the high temperature end. The H<sub>2</sub> co-feed decreased the peak intensity, but not as strongly as the cases in the Fe/SiO<sub>2</sub> sample.

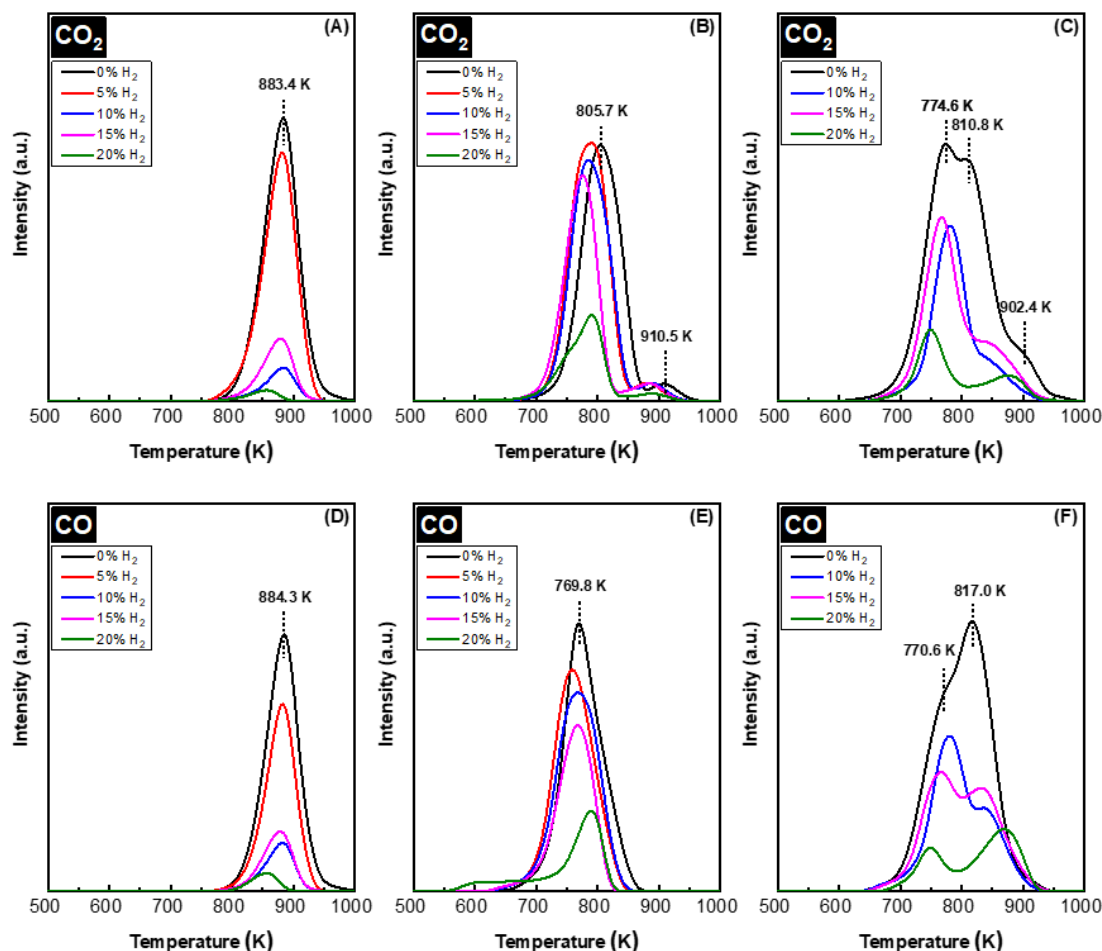


**Figure 2.8.** CO<sub>2</sub> and CO evolution peaks in TPO profiles of spent Fe/SiO<sub>2</sub> catalyst (A and D), SCZO perovskite oxide (B and E), and 5wt.% SCZO in Fe/SiO<sub>2</sub> (C and F) at different H<sub>2</sub> co-feed concentrations after ToS of 3.5 h in NMC reactions.

The TPO peak temperatures reflected the types of coking species in the spent methane activation catalysts. The TPO spectra for each spent catalyst could be deconvoluted into three peaks - a low, medium, and high temperature peak. The low temperature peak could be described as amorphous and oxidized “soft” coke, the medium temperature peak to polymeric aromatic carbon, and the high temperature peak to the ordered, graphitic “hard” coke. The formation of diverse carbon species in the NMC reaction has been observed in Mo/ZSM-5<sup>58,102,103</sup> and metal/sulfated zirconia catalysts<sup>55,104,105</sup> as well as in methane pyrolysis in the absence of any catalyst.<sup>106-109</sup>

The H<sub>2</sub> co-fed NMC condition in the presence of SCZO oxide apparently leads to an obvious increase in the soft coke on the Fe/SiO<sub>2</sub> catalyst, resulting in active NMC reaction without obvious methane conversion drop or high coke selectivity.

#### 2.3.4.3 X-ray photoelectron spectroscopy

Figure 2.9 shows the XPS spectra of C 1s, O 1s, Si 2p, Ce 3d, Sr 3d and Zr 3d of the spent Fe/SiO<sub>2</sub> and SCZO mixture samples in NMC in the absence and presence of H<sub>2</sub> co-feed conditions. The XPS spectra of fresh SCZO or Fe/SiO<sub>2</sub> were included in some of the sub-figures in Figure 2.9(A) for comparison purposes. In Figure 2.9(A), the XPS data of C 1s from the fresh SCZO and Fe/SiO<sub>2</sub> samples has prominent peaks, which are attributed to adventitious carbon present on the surface of the as-prepared materials<sup>110,111</sup>. The XPS spectra of C1s can be deconvoluted into four peaks, located at 284.1, 284.7, 286.4, 288.8 eV in sequence, which can be assigned to carbon in the carbidic (e.g. Si-C or Fe-C), graphitic (C-C or C=C), C-O-C and O-C-O structures, respectively.<sup>92</sup> In comparison to individual SCZO oxide or Fe/SiO<sub>2</sub> catalyst sample, after the NMC reaction, the XPS peak assigned to C-C or C=C group in the SCZO and Fe/SiO<sub>2</sub> mixture samples increased significantly, suggesting the carbon deposition onto these samples from NMC. The appearance of peak around 284.1 eV suggested the formation of metal carbide species when SCZO amount was high in the mixture. In 5wt% SCZO in Fe/SiO<sub>2</sub> sample, this low binding energy peak diminished, so the XPS spectra of C 1s from the SCZO and Fe/SiO<sub>2</sub> mixture sample shares the same feature as that of the fresh SCZO and Fe/SiO<sub>2</sub>, regardless of the H<sub>2</sub> concentration in the feed stream.

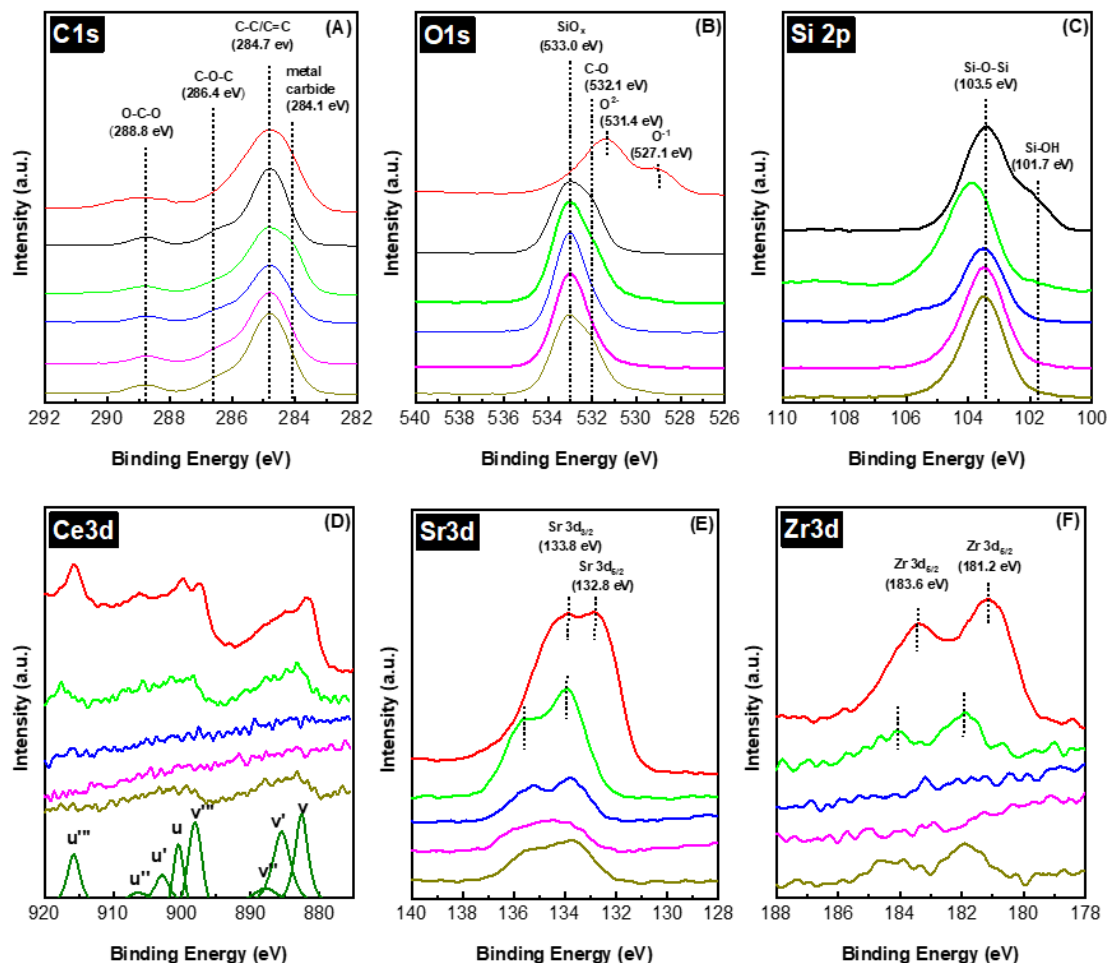


**Figure 2.9.** XPS spectra of C1s (A), O1s (B), Si2p (C), Ce3d (D), Sr3d (E) and Zr3d (F) of fresh SCZO (red), fresh FeSiO<sub>2</sub> (black), spent FeSiO<sub>2</sub> mixed with SCZO in 2:1 mass ratio (green), spent FeSiO<sub>2</sub> mixed with 5 wt.% SCZO (blue), spent FeSiO<sub>2</sub> mixed with 5 wt.% SCZO under 10% H<sub>2</sub> co-feed (purple) and spent FeSiO<sub>2</sub> mixed with 5 wt.% SCZO under 20% H<sub>2</sub> co-feed (dark yellow), respectively.

The XPS data of O 1s in Figure 2.9(B) shows that the fresh Fe/SiO<sub>2</sub> exhibits two peaks at 533.0 and 532.1 eV, which could be assigned to the Si-O-Si structure in the quartz support<sup>90,91</sup> and the oxygen bonded in the organic C-O structures<sup>92</sup>, respectively. The two peaks at 531.4 and 527.1 eV in fresh SCZO were assigned to the O<sup>2-</sup> and O<sup>1-</sup> ions in the perovskite oxide material, as discussed in Section 5.3.1. After the NMC reaction, in the SCZO and FeO<sub>2</sub> mixture sample, the XPS peaks of C-O and oxide ions were reduced significantly. The reductive environment apparently removed

these oxygen species. In the presence of 20% H<sub>2</sub> co-feed, this XPS peak recovers its intensity to the level similar to that of the fresh Fe/SiO<sub>2</sub> sample. Figure 2.9(C) presents the XPS data of Si 2p in these samples. The peaks at 103.5 and 101.7 eV in Fe/SiO<sub>2</sub> sample are associated to the Si-O-Si and Si-OH structures. The positions of peak at 130.5 eV are shifted to higher binding energies because of the Si-O-Si bond interaction with the metal-oxygen bonds in SCZO in their mixture (33wt.% SCZO in Fe/SiO<sub>2</sub>) in NMC<sup>112</sup>. Different from shifting Si 2p to higher binding energies in the mixture with high SCZO usage, 5wt.% SCZO in Fe/SiO<sub>2</sub> did not have obvious peak shift. The presence of H<sub>2</sub> in the methane feed, however, reduced the Si-OH structure, but Si-O-Si was not influenced obviously.

As a reducible metal oxide, the XPS data of Ce 3d, Sr 3d and Zr 3d in SCZO perovskite oxide were analyzed to understand their changes caused by the NMC reaction. As shown in Figure 2.9(D), the Ce 3d spectrum of the fresh SCZO sample has complicated features due to mixing of Ce 4f levels with O 2p states. Two sets of spin-orbital multiplets, corresponding to the 3d<sub>3/2</sub> and 3d<sub>5/2</sub> contributions, were labeled as u and v, respectively<sup>113-115</sup>. The peaks labeled v and v'' have been assigned to a mixing of Ce 3d<sup>9</sup> 4f<sup>2</sup> O 2p<sup>4</sup> and Ce 3d<sup>9</sup> 4f<sup>1</sup> O 2p<sup>5</sup> Ce<sup>4+</sup> final states, and the peak denoted v''' corresponds to the Ce 3d<sup>9</sup> 4f<sup>0</sup> O 2p<sup>6</sup> Ce<sup>4+</sup> final state. On the other hand, the peak v' are assigned to Ce 3d<sup>9</sup> 4f<sup>1</sup> O 2p<sup>6</sup> of Ce<sup>3+</sup>. The same assignment can be applied to the u structures, which correspond to the Ce 3d<sub>3/2</sub> levels. The very sharp v, v''', u and u''' peaks indicated the Ce<sup>4+</sup> dominantly existing in the fresh SCZO. In the spent SCZO and Fe/SiO<sub>2</sub> mixture samples, all these peaks have reduced intensity and shifted to higher binding energies. The same phenomenon was observed for Sr 3d and Zr 3d XPS

data in Figures 5.9(E)-(F). The decrease in the peak intensity was caused by the low SCZO concentrations in the mixture samples, while the peak shift should have been due to the bonding environment change.

In general, a pseudo-binary metal oxide alloy formed by mixing two elemental oxides (e.g.,  $M_aO_b$  and  $N_mO_n$ ) displays M-O-M, N-O-N and M-O-N bonds. If the electronegativity of atom N was larger than M, there were M-O alloy bonds that were more ionic, and N-O bonds that were more covalent in the alloys, than in the respective elemental oxide phases<sup>116</sup>. In the SCZO and  $SiO_2$  mixture, Si was more electronegative than any metal atoms in SCZO. Therefore, the Ce-O bond was more positively ionic than its state in the SCZO material alone, and thus the peak shifted to a higher binding energy. The same reasoning applies to the left-shift in binding energies of Sr 3d and Zr 3d in Figures 5.9(E)-(F). In the spent SCZO and Fe/ $SiO_2$  mixture (i.e., 33wt.% SCZO in Fe/ $SiO_2$ ), the v' and u' peaks are very obvious, indicating the presence of  $Ce^{3+}$  in the sample. The decrease in SCZO quantity to 5wt%. decreased the peak intensity of Ce 3d XPS peak in the SCZO and Fe/ $SiO_2$  mixture sample. The peak intensity is too low to detect clear peaks in the spent sample. The presence of 20%  $H_2$  co-feed in the methane stream in the reaction enabled appearance of these peaks, but the peak intensity is quite low to inform any confirmative information. For the same reason, the XPS peaks of Zr 3d were not obvious for clear analyses. As noted earlier, the formation of Zr-O-Si bond in the SCZO and Fe/ $SiO_2$  mixture is responsible for shifting the Sr 3d peaks to higher binding energies. The presence of  $H_2$  co-feed does not show obvious influences on its bonding environment. Due to the low concentration (0.075 wt.%) of

Fe in the Fe/SiO<sub>2</sub> catalyst, the peaks correlating to Fe binding energies showed a low signal-to-noise ratio and were not included in this discussion.

#### 2.4 Conclusion of chapter 2

The direct non-oxidative methane coupling (NMC) was studied in a fixed-bed reactor packed with a well-mixed Fe/SiO<sub>2</sub> catalyst and SCZO perovskite oxide materials. By flowing proper concentration of H<sub>2</sub> co-feed in the methane stream, NMC with stable and high methane conversion and low coke selectivity were achieved. Characterizations on the spent Fe/SiO<sub>2</sub> catalyst, SCZO oxide and their mixture samples show the co-existence of Fe/SiO<sub>2</sub>, SCZO and H<sub>2</sub> co-feed favors low temperature “soft coke” formation. As a MIEC material, SCZO could function as a “hydrogen transformer” that converted absorbed hydrogen into smaller species (e.g., proton and electron) to influence coke formation on the catalyst. This leads to a low local H<sub>2</sub> concentration and less potential to reverse the NMC reaction according to the Le Chatelier’s principle. The addition of H<sub>2</sub> co-feed into the reactor packed with the sole Fe/SiO<sub>2</sub> catalyst, however, leads to a sharp decrease in methane conversion. The present study mimics NMC in the H<sub>2</sub>-permeable membrane reactor that is made of SCZO membrane tube packed with Fe/SiO<sub>2</sub> catalyst with H<sub>2</sub> sweep gas flowing outside. The results obtained in this work can guide the design and operation of H<sub>2</sub>-permeable membranes for alkane dehydrogenation in general.

## Chapter 3: Sharpening Spatial Temperature of Autothermal Catalytic Wall Reactor for Selective Nonoxidative Coupling of Methane

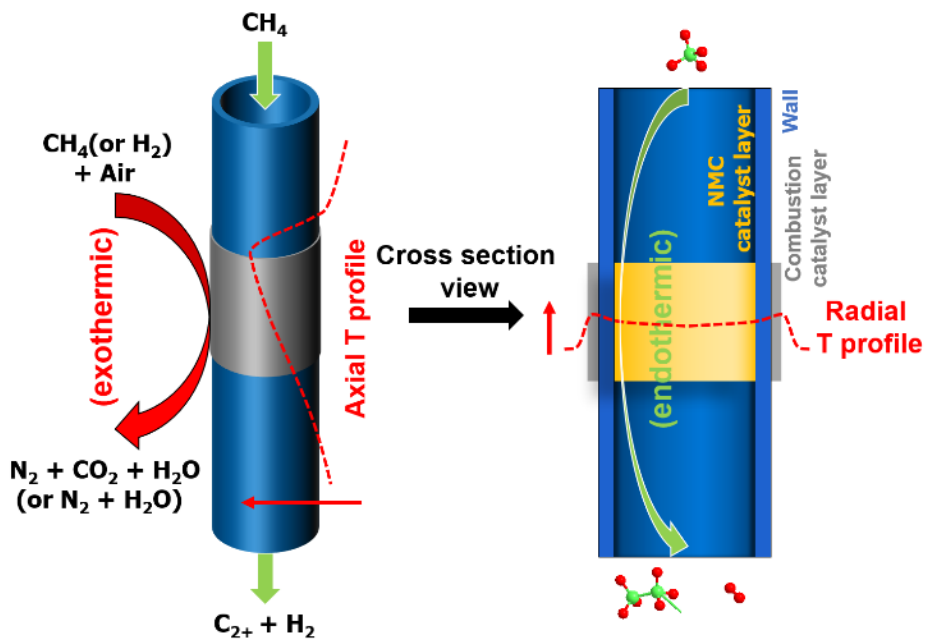
### *3.1 Introduction*

Traditionally, the NMC reaction has suffered from low methane conversion, low product yield and catalyst durability, rooted in the endothermic nature of the reaction. Since high temperature is a thermodynamic requirement for methane C-H bond activation, engineered catalysts, reactors, and processes are required to minimize the subsequent activation of coupling products to undesirable hydrocarbons and coke. Novel catalyst development has been aimed to address this issue. Extensive studies on the molybdenum/ZSM-5 zeolite (Mo/ZSM-5) catalyst have improved hydrocarbon product selectivity at <1023 K (with low methane conversion) but rapid catalyst deactivation due to coking emerges at higher conversions<sup>31,74,117-119</sup>. Fe/SiO<sub>2</sub> has been reported as an effective catalyst at higher temperatures ~1223-1363 K with potential for high methane conversion while preserving high hydrocarbon yields and long-term stability<sup>48</sup>. A mechanistic investigation into this Fe/SiO<sub>2</sub> catalyst revealed that a complex heterogeneous - homogeneous reaction network underlies its performance. The silica lattice-confined Fe species initiate methane dehydrogenation to generate methyl and hydrogen species, enabling a series of subsequent surface and gas-phase reactions to form dehydrogenated and cyclized larger hydrocarbon products<sup>3,78</sup>. Based on this mechanistic understanding, thermal engineering could be a potential strategy for tailoring NMC reaction performance towards lighter hydrocarbons by quenching the subsequent formation of larger hydrocarbons. However, typical upcycling processes via non-catalytic pyrolysis<sup>120-122</sup> or catalytic fixed-beds<sup>56,123,124</sup> rely on

electric furnaces to create a uniform temperature distribution in the heating zone, where opportunities to engineer temperature profiles are minimal. As a proof of concept, independent furnaces heating upstream and downstream of a catalytic fixed bed have shown to influence NMC performance<sup>47</sup>. However, as a major focus has been to develop new catalysts or gain a mechanistic understanding, where fixed beds and membrane reactors are the configurations of choice<sup>78,125</sup>, reactor designs leveraging these mechanistic insights remain unexplored.

In this work, motivated by the potential of improving NMC performance by engineering the thermal driving force<sup>65,126,127</sup>, we design, construct, and operate a modular autothermal catalytic wall reactor (ACWR) with sharp temperature profiles. The developed autothermal ACWR reactor (Schematic 2.1), is made of a quartz tube, coated with NMC and fuel combustion catalysts on opposite tube wall surfaces. The NMC catalyst induces methane activation by heterogeneous surface dehydrogenation at a medium-high temperature (1173-1523 K) that is maintained by the fuel combustion on the other side of the reactor wall using the fed methane/air mixture. Placing the catalysts directly onto the inner (Fe/SiO<sub>2</sub> for endothermic NMC) and outer (Pt/Al<sub>2</sub>O<sub>3</sub> for exothermic combustion) walls of reactor promotes heat transfer in thermal boundary layers. The flame fusion reactor manufacture method allows perfect contact inbetween the catalyst particles and quartz reactor wall shown in Figure 2.2. Razza et al.<sup>128</sup> has proven that such direct contact will significantly improve the heat transfer into the inner reactor chamber. Sharp temperature gradients along axial direction controlled by catalyst zoning, together with short contact-time (e.g., diffusion time of reactant to the reactive wall is within millisecond and shorter than those of product hydrocarbons),

inhibit the secondary and follow-on reactions avoiding coke formation and catalyst deactivation enabling excellent performance.



**Schematic 2.1.** Schematics of autothermal millisecond catalytic wall reactor that couples endothermic NMC and exothermic fuel combustion on reactor wall surfaces. Sharp axial reactor temperature gradient and the use of H<sub>2</sub> byproduct as combustion fuel realize high hydrocarbon yield, negligible coke, and self-sustainability.

### 3.2 Experimental Preparation and Test Procedure

#### 3.2.1 Reactor Structure

The autothermal millisecond catalytic wall reactor was made of two concentric quartz tubes, as shown in Schematic 2.1. The inner tube had an outside diameter of 6.35 mm and a thickness of 1.00 mm. The outer tube had an outside diameter of 12.7 mm and a thickness of 1.20 mm. The exothermic methane combustion gases (i.e., methane and air) flew through the annulus region of the reactor, while the methane in endothermic NMC flew through the inner tube. The length of the catalyst coatings on the catalytic wall surface was ~90.00 mm on both sides. The outer tube was insulated

by a ceramic fiber blanket and ceramic cylinder. During the reactions, the heat generated from the catalytic combustion is transferred across the quartz wall to drive the endothermic NMC reaction occurring inside the tube.

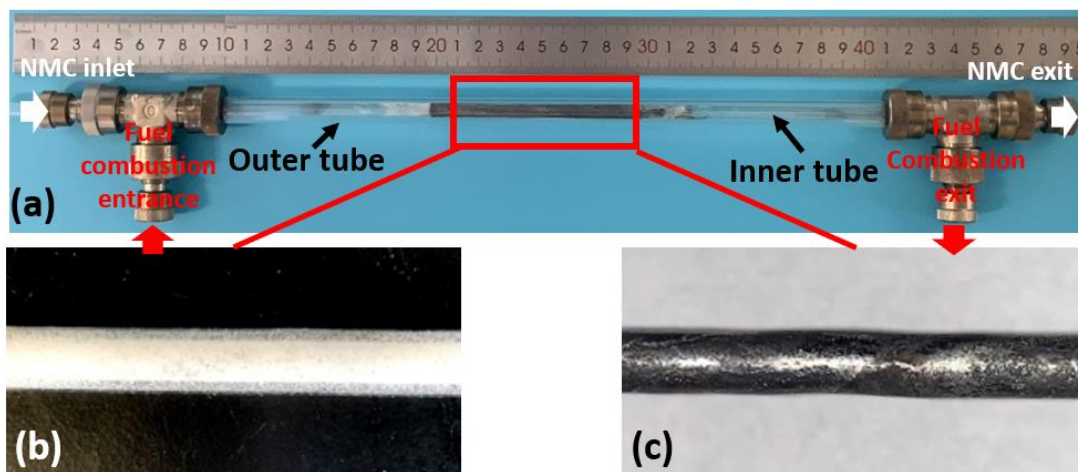


**Figure 2.1.** (a) Photo of autothermal ACWR with Fe/SiO<sub>2</sub> and Pt/Al<sub>2</sub>O<sub>3</sub> coated zones for coupling NMC and fuel combustion reactions; (b) morphology of Fe/SiO<sub>2</sub> catalyst region in inner tube surface of autothermal ACWR; and (c) morphology of Pt/Al<sub>2</sub>O<sub>3</sub> catalyst region on the exterior surface of the reactor wall.

### 3.2.2 *Reactor fabrication*

#### 3.2.2.1 *Coating of NMC catalyst onto the inner reactor wall surface*

Fe/SiO<sub>2</sub> was used as the NMC catalyst. The Fe/SiO<sub>2</sub> catalyst synthesis was reported previously<sup>49</sup>. To coat Fe/SiO<sub>2</sub> catalyst onto the inner wall of the quartz tube, sufficient Fe/SiO<sub>2</sub> (0.075 wt% Fe) catalyst was loaded until catalyst length along the tube reached 90.00 mm. The tube was then treated with hydrogen flame repeatedly. The hydrogen flame was formed by mixing hydrogen (Airgas, industrial grade) and oxygen gas (Airgas, industrial grade) via a hydrogen torch to create a sharp blue flame. By removing the residual catalyst from the tube, a thin uniform layer of Fe/SiO<sub>2</sub> catalyst can be visually observed, as shown in Figure 2.1b and Figure 2.2. Fe/SiO<sub>2</sub> particles

were lightly fused with each other as well as the quartz wall, forming a 550  $\mu\text{m}$  thick layer.

### 3.2.2.2 Coating of fuel combustion catalyst onto the external surface of the reactor wall

Pt/Al<sub>2</sub>O<sub>3</sub> was used as the exothermic reaction catalyst. In order to develop this catalyst layer, an aqueous solution that contained 10.0 wt%  $\gamma$ -alumina (Alfa Aesar, >99.97% purity), 1.0 wt% Cr(NO<sub>3</sub>)<sub>3</sub>•9 H<sub>2</sub>O (Alfa Aesar, 99.99% purity), and 0.1 wt% Y(NO<sub>3</sub>)<sub>3</sub>•6 H<sub>2</sub>O (Alfa Aesar, 99.9% purity) was firstly prepared. After stirring the mixture for 1 h, the aqueous solution was applied dropwise on the outside quartz tube. Then the tube was treated with a hydrogen flame briefly. The application of aqueous ceramic mixture onto the reactor tube and flame fusing of the applied materials were repeated until a visible layer of light-yellow coating was formed. This layer is used to improve the adhesion of the fuel combustion catalyst onto the reactor tube. Another 1g aqueous solution containing 8.0 wt% H<sub>2</sub>PtCl<sub>6</sub>•2H<sub>2</sub>O (Alfa Aesar, 99.9% purity) was applied on top of the yellow layer dropwise and treated in a hydrogen flame. The final catalyst coating was visibly black, as illustrated in **Figure 2.1c** and **Figure 2.2**. The Pt/Al<sub>2</sub>O<sub>3</sub> layer formed a continuous layer on the surface of the quartz tube with an average layer thickness of approximately 30  $\mu\text{m}$ .

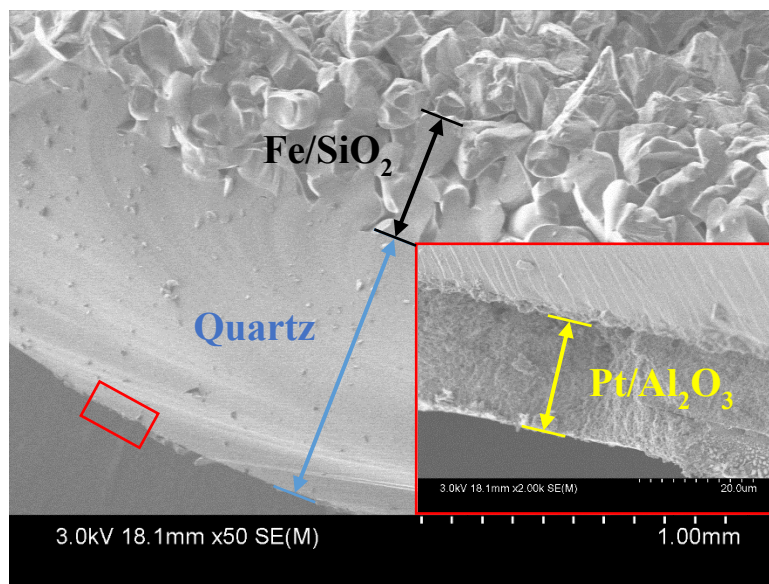


**Figure 2.2.** SEM images showing a cross-section view of ACWR, where Pt/Al<sub>2</sub>O<sub>3</sub> catalyst layer is on the exterior surface of reactor wall and Fe/SiO<sub>2</sub> catalyst layer is fused onto the inner wall surface.

### 3.2.3 Reactor fabrication

#### 3.2.3.1 NMC reaction in the fix-bed and blank reactors

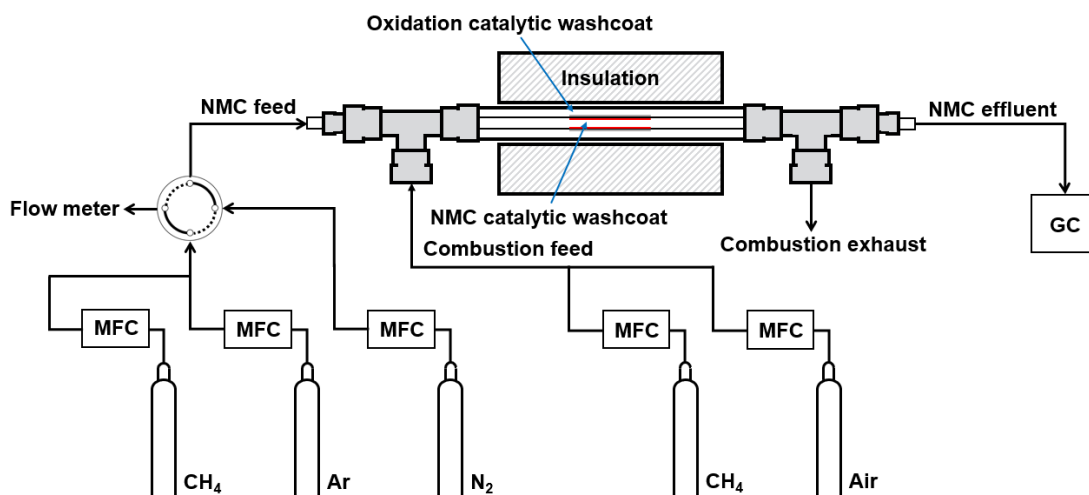
The fixed-bed reactor was made of a non-active straight ¼ inch quartz tube. In the NMC test, 0.375 g of Fe/SiO<sub>2</sub> catalyst was loaded into the reactor, and the position was secured using quartz wool. The reactor was placed horizontally inside a temperature-controlled furnace (Applied Test Systems 3210). A K-type thermocouple was inserted into the reactor to record the temperature. The gas flow was controlled by mass flow controllers (Brooks MFC SLA5850).

Prior to the NMC reaction, the catalyst was heated in an Ar atmosphere (0.48 L h<sup>-1</sup>) to the reaction temperature of 1273 K at 10 K min<sup>-1</sup> ramp rate and kept at the reaction temperature for 1 h. The methane (Airgas MEUHP200, 99.999% purity) and

Ar (Airgas ARUHP300, 99.999% purity) gas mixture was then introduced into the reactor at  $0.48 \text{ L h}^{-1}$  ( $\text{CH}_4:\text{Ar} = 7:1$ ). The product effluents were analyzed online using a gas chromatograph (Agilent Technologies, 5890N) equipped with a DB-WAX column coupled with FID and ShinCarbon ST pack column coupled with TCD to determine methane conversion and hydrocarbon selectivity. To avoid product condensation, all the gas transferring lines were heated to 493 K. The blank reactor test was done using the same conditions as the fixed-bed reactor, except that the catalyst was not used.

### 3.2.3.2 NMC reaction in the ACWR and single layer Fe/SiO<sub>2</sub> CWR

The catalytic wall reactor was fabricated as described in Section 2.2.1 and 2.2.2 above. To start the autothermal NMC reaction in the reactor, methane (Airgas MEUHP200, purity 99.999%) and Air (Airgas AI B300) in the ratio of 1:10 were fed into the exothermic side, while Ar (Airgas ARUHP300, purity 99.999%) was fed into the endothermic side at room temperature first. The exothermic reaction was ignited by directly flame heating the outer tube over the catalytic wall briefly with a propane torch (Bernzomatic WK2301). The ignited Pt-Al<sub>2</sub>O<sub>3</sub> catalyst showed bright red color and extended toward the upstream end of the catalytic wall. The reactor was then insulated by ceramic fibers and cylinders. To monitor the inner tube temperature, a thermocouple was inserted into the inner tube. When the temperature stabilized, methane and Ar with designated flow rates (Ar as internal standard) were fed into the endothermic side, illustrated as Schematic 3.2. The single layer Fe/SiO<sub>2</sub> CWR was tested at the same conditions as the ACWR described here, except the reactor was heated by the electric furnace as the fixed-bed reactor.



**Schematic 3.2.** Schematic drawing of the ACWR system coupling NMC and fuel oxidation reactions.

### 3.2.4 Catalyst characterization

The morphologies of the coated catalysts were observed by scanning electron microscopy (SEM) on a Hitachi SU-70 electron microscope. The specific surface areas of the samples were determined using (Brunauer, Emmett and Teller) (BET) method. Thermogravimetric analysis (TGA) of the catalyst samples was performed in a TGA instrument (2950, TA Instruments, Inc.) under 40 min<sup>-1</sup> of air flow with a heating rate of 10 K min<sup>-1</sup> from 308 K to 1273 K. The surface roughness of catalytic layer was measured by laser microscopy on a Keyence VK-X3000 3D surface profiler with VK-X 3000 Viewer Suite.

## 3.3 Results and Discussion

### 3.3.1 Control experiments for ACWR

The capability of our ACWR is established by comparison to three controls -- a blank reactor, a fixed-bed reactor packed with the Fe/SiO<sub>2</sub> catalyst, and an ACWR

coated with the Fe/SiO<sub>2</sub> catalyst, that were all heated by an electric furnace (Figure 3.3a). The methane conversions were 4.9% (blank), 12.5% (fixed bed), 11.3% (CWR) and 11.0% (ACWR) (Figure 3.3b), with the peak reactor temperature controlled at 1273 K across all cases (Figure 3.3c). Reactor axial position “0 mm” is defined as the gas inlet of the NMC reaction. The presence of Fe/SiO<sub>2</sub> catalyst increased methane conversion (blank versus rest), confirming the existence of heterogeneous methane activation, although it is not sensitively influenced by the catalyst loading quantity and format, as the fixed-bed reactor and CWR showed similar conversions. The product selectivity, however, is significantly influenced by the reactor heating and catalyst loading methods (Figure 3.3b). The coke selectivity shifted from 10.2% in the fixed-bed reactor to 0.8% in the CWR heated by electric furnace to ~0 in the ACWR. Importantly, the C<sub>2</sub> selectivity increased favorably from 60.8% and 69.9% to 92.2% in sequence, accompanied with a decrease in aromatics. selectivity from 28.9% and 29.4% to 7.8%. NMC over the Fe/SiO<sub>2</sub> catalyst has a mixed heterogeneous-homogeneous reaction network, in which the catalyst initiates methane dehydrogenation, generating methyl and hydrogen species, followed by a series of subsequent reaction steps that form dehydrogenated and cyclized larger hydrocarbon products<sup>48,49,71,129,130</sup>. The short-contact-time in the CWR to suppress subsequent chemistries is an important aspect in enhancing the olefin and hydrogen production<sup>131-134</sup>. However, this characteristic alone is not sufficient to extensively suppress coke formation in NMC.<sup>35</sup> Combining the short residence time with the rapid thermal activation and quenching zones developed in the ACWR (Figure 3.3), in contrast to the uniform isothermal zone in electrically heated reactors heated, is a key factor in inhibiting secondary and follow-on reactions.

This inhibition underlies the observed high C<sub>2</sub> selectivity and negligible coke formation. Furthermore, such an exceptional performance is found to be stable over the whole duration of a 10h operation (Figure 3.3d). Post an initial induction period (~2 h, caused when NMC flow switched from inert gas to methane), the time-on-stream (TOS) performance reveals a stable reaction with high methane conversion (~13.7%), high C<sub>2+</sub> hydrocarbons selectivity (66.4% C<sub>2</sub> and 33.6% aromatics), and negligible coking.

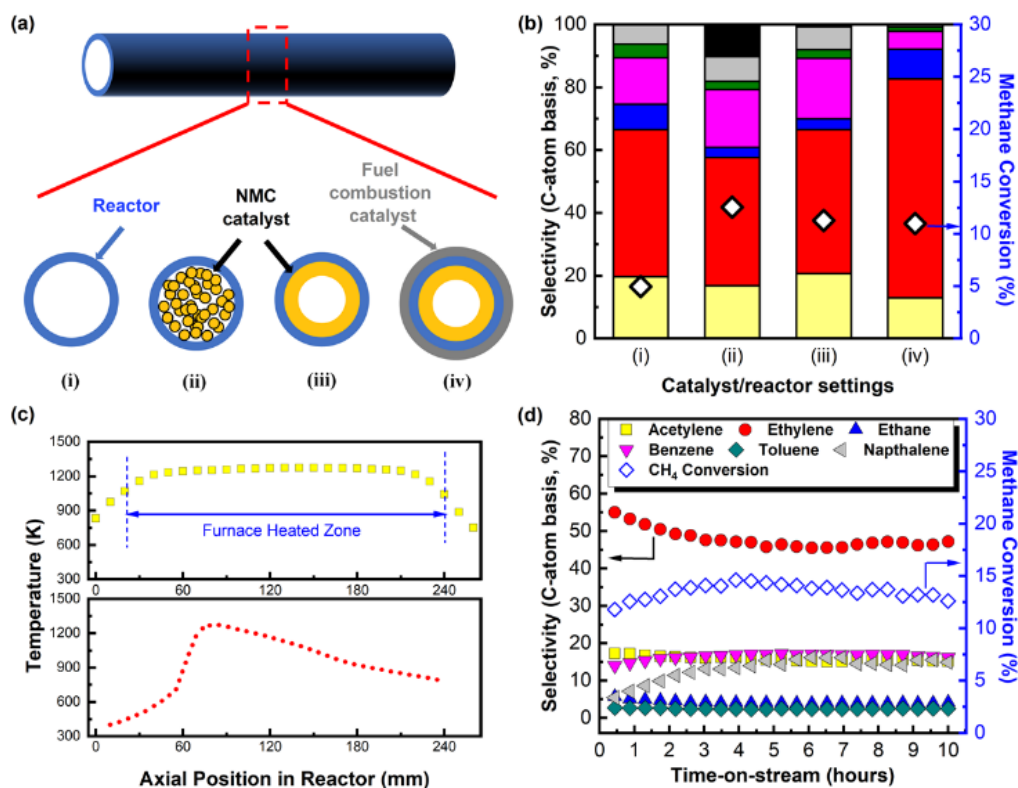


**Figure 3.3.** (a) Cross sectional view of reactor configurations (i) blank; (ii) fixed bed; (iii) CWR and (iv) ACWR. (b) methane conversion and product selectivity in NMC in reactor configurations from (a) in sequence. (Component color Indicators: coke, naphthalene, toluene, benzene, ethane, ethylene, and acetylene) (c) Measured temperature profiles in reactors heated by an electric furnace (top) and fuel combustion (bottom) controlled to the same peak temperature; and (d) NMC performance time-on-stream in ACWR. All data (a-c) was collected under steady state conditions. (NMC reaction: 0.48 L h<sup>-1</sup> gas flow with CH<sub>4</sub>:Ar ratio = 7, 101.325 kPa pressure, 0.375 g Fe/SiO<sub>2</sub> catalyst in fixed-bed reactor, 0.2 g Fe/SiO<sub>2</sub> catalyst in ACWR, Fe

concentration = 0.075 wt%; fuel combustion: 145.2 L h<sup>-1</sup> gas flow with CH<sub>4</sub>:Air ratio = 0.1, 101.325 kPa pressure, 0.1 g Pt/Al<sub>2</sub>O<sub>3</sub> catalyst, Pt concentration = 1.0 wt%)

### 3.3.2 *NMC Performance of ACWR*

Next, to further tune these performance metrics and temperature profiles, the relative flow direction (i.e., co-current versus counter-current flow) and gas flow rates in the reaction channel and combustion channel were studied independently. In the co-current flow mode, under a fixed CH<sub>4</sub>/air flow in the exothermic fuel combustion channel, the increase in methane flow in the endothermic NMC channel decreased the contact time of methane as well as the width and peak temperature of the heating zone (Figure 3.4a). The methane conversion in the NMC channel decreased from 14.2 % to 1.6 % while the C<sub>2</sub> selectivity increased from 61.9% to 98.0% at the expense of aromatics (Figure 3.4b). Countercurrent CH<sub>4</sub>/air flow similarly impacted the temperature profiles (peak temperature, breadth of heating zone, see Figure 3.4c) and NMC performance (methane conversion, product selectivity, see Figure 3.4d) as the methane flow in the NMC reaction channel increased. A comparison between co-current and counter-current flow modes reveals that the peak temperature and its position were 59, 96, 90, and 60 K higher and ~90 mm later in the counter-current cases for the 0.3, 0.48, 0.66 and 1.2 L h<sup>-1</sup> NMC flow rate, respectively. These led to higher methane conversions, higher acetylene and lower aromatics selectivity than the co-current flow mode at the same flow rates in both reaction channels. The increase in methane conversion could be attributed to its longer passage to reach the peak temperature and the increased peak temperature in counter-current mode. The enhancement in acetylene selectivity was attributable to the very sharp temperature drop after the maximum temperature. The decrease in aromatics selectivity indicates

that acetylene is the precursor of benzene and other aromatics, as the sudden temperature drop (or cooling) after the methane activation zone limited the secondary reaction steps in NMC. Further studies in the co-current flow mode showed that the NMC methane conversion increased with an increase of CH<sub>4</sub>/air flow in the combustion channel under fixed flow rate in the NMC reaction channel (Figure 3.4e), contributed by a higher peak temperature associated with higher heat energy released from CH<sub>4</sub> combustion. The naphthalene selectivity increased with increased methane conversion could be contributed to the elevated temperature profile, which would also promote secondary gas phase reaction in the catalytic combustion zone. The manipulation of gas flow rates in both reaction channels under co-current flow pattern promoted methane conversion while tuned the selectivity either towards ethylene or benzene (Figure 3.4f), and a single pass 27.0% methane conversion, 77.8% C<sub>2</sub> (21.0% yield), 17.3% benzene and 3.6% naphthalene selectivity with negligible coke were achieved in NMC in the ACWR with 0.48 L h<sup>-1</sup> NMC gas flow rate and peak temperature at 1384 K under co-current operation. Moreover, a single pass 36.4% methane conversion, 26.8% C<sub>2</sub>, 45.7% benzene (16.6% yield) and 23.6% naphthalene selectivity with negligible coke were achieved in NMC in the ACWR with 1.2 L h<sup>-1</sup> NMC gas flow rate and peak temperature at 1423 K under co-current operation.

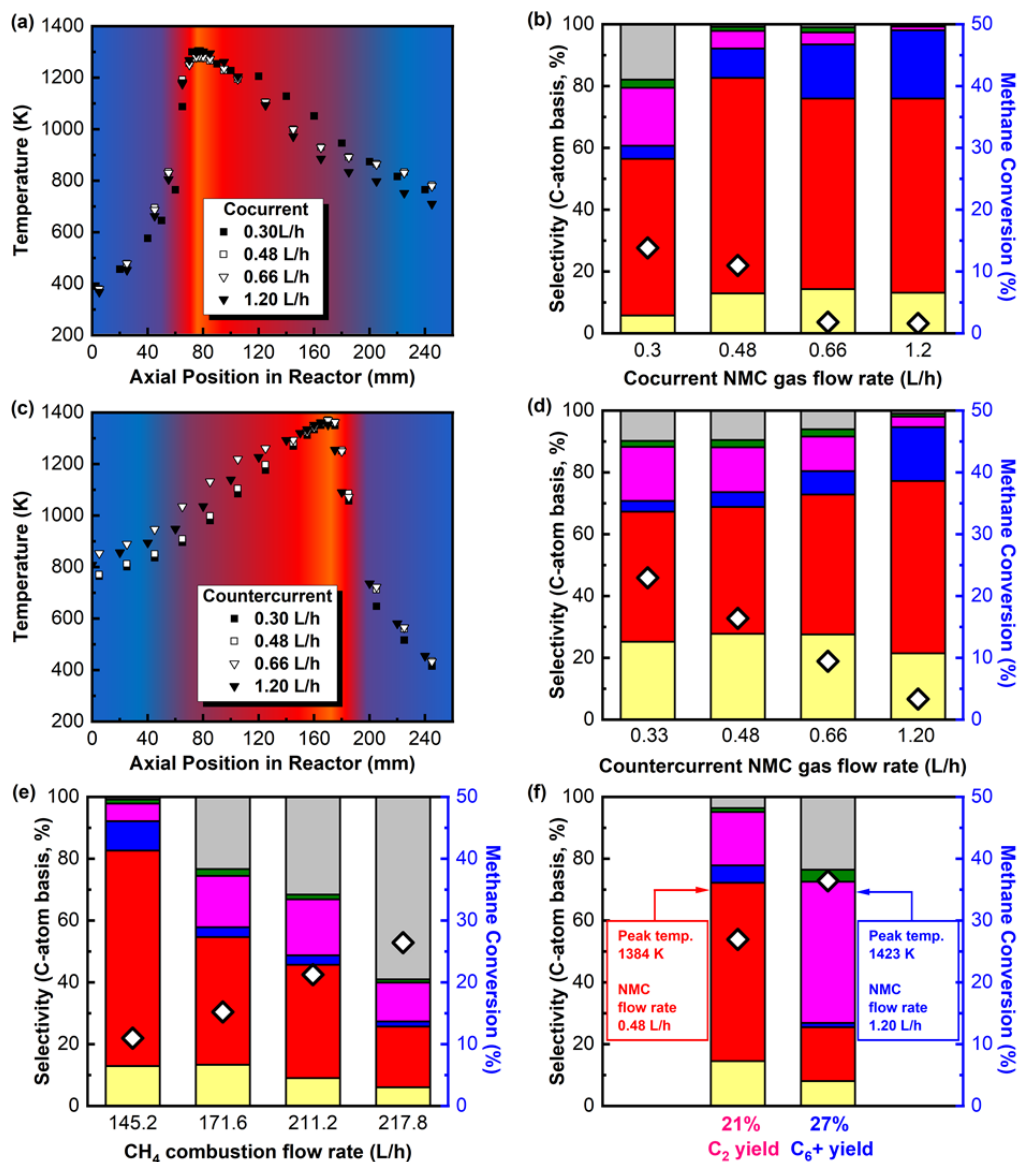


**Figure 3.4.** Effects of gas flow rate and direction on methane conversion and product selectivity in NMC in the ACWR. (a) Temperature profile, (b) methane conversion and product selectivity of varying methane flow rate in the NMC channel at a fixed combustion gas flow rate of 145.2 L h<sup>-1</sup> gas flow (CH<sub>4</sub>:Air ratio = 0.1) under co-current flow. (c) Temperature profile, (d) methane conversion and product selectivity of varying methane flow rate in the NMC channel at a fixed combustion gas flow rate of 145.2 L h<sup>-1</sup> gas flow (CH<sub>4</sub>:Air ratio = 0.1) under counter-current flow. (e) Varying combustion gas flow rate at a fixed NMC gas flow rate of 0.48 L h<sup>-1</sup> gas flow (CH<sub>4</sub>:Ar ratio = 7). (f) Maximized NMC performance by adjusting both NMC and fuel combustion flow rates. (Component color Indicators for (b), (d), (e) and (f): ■ coke, ■ naphthalene, ■ toluene, ■ benzene, ■ ethane, ■ ethylene and ■ acetylene)

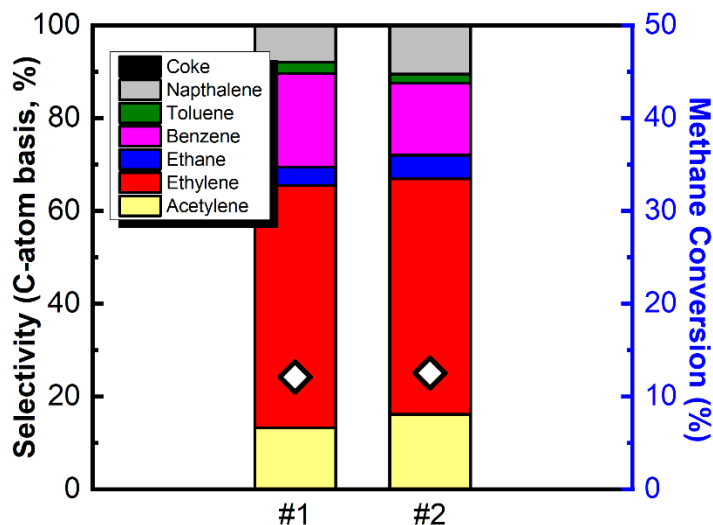


**Figure 3.5.** Methane conversion and product selectivity of two ACWR manufactured under identical process. (Reaction condition: 0.48 L h<sup>-1</sup> gas flow with CH<sub>4</sub>:Ar ratio = 7, 101.325 kPa pressure, 0.2 g Fe/SiO<sub>2</sub> catalyst in ACWR, Fe concentration = 0.075 wt%; Fuel combustion: 165 L h<sup>-1</sup> gas flow with CH<sub>4</sub>:Air ratio = 0.1, 101.325 kPa pressure, 0.1 g Pt/Al<sub>2</sub>O<sub>3</sub> catalyst, Pt concentration = 1.0 wt%)

To confirm the reproducibility of the autothermal millisecond catalytic wall reactor, two additional reactors following the same materials and synthesis method mentioned in the manuscript. Figure 3.5 showed that under the same feed flow conditions, the NMC reaction had similar methane conversion and product selectivity and their respected peak temperatures were 1060 and 1057 °C. This has confirmed that small NMC performance variation might be caused by surface uniformity of Pt/Al<sub>2</sub>O<sub>3</sub> loading for methane combustion reaction during initial synthesis, but the effect is very limited. Furthermore, the methane combustion products analyzed by GC showed that 99.8% and 99.5% methane was completely combusted in the reproducibility test, which validated the assumption of complete methane combustion in the modeling work.

### 3.3.3 Coke analysis and evaluation of catalytic layer uniformity

To evaluate the accuracy of the coke calculation from carbon balance, the amount of coke formed in the catalytic wall reactor was determined by TGA. First, the post reaction inner catalytic tube was obtained from the reproducibility test after 6 hours of reaction. (Figure 3.6) The reactor was split into 3 parts: pre catalytic zone, catalytic zone, and post catalytic zone. As it is difficult to remove catalytic layers from the quartz wall, each zone was grinded into powder and the TGA profile of each powder sample is shown in Figure 3.7. The weight loss of  $0 \pm 0.01\%$  was observed on all powders. The coke selectivity calculated based on TGA measurement was  $0 \pm 0.24\%$ . Thus, using carbon balance to determine coke selectivity is valid.



**Figure 3.6.** Inner tube of ACWR after 6 hours of reaction. (Reaction condition: 0.48 L h<sup>-1</sup> gas flow with CH<sub>4</sub>:Ar ratio = 7, 101.325 kPa pressure, 0.2 g Fe/SiO<sub>2</sub> catalyst in ACWR, Fe concentration = 0.075 wt%; Fuel combustion: 165 L h<sup>-1</sup> gas flow with CH<sub>4</sub>:Air ratio = 0.1, 101.325 kPa pressure, 0.1 g Pt/Al<sub>2</sub>O<sub>3</sub> catalyst, Pt concentration = 1.0 wt%)

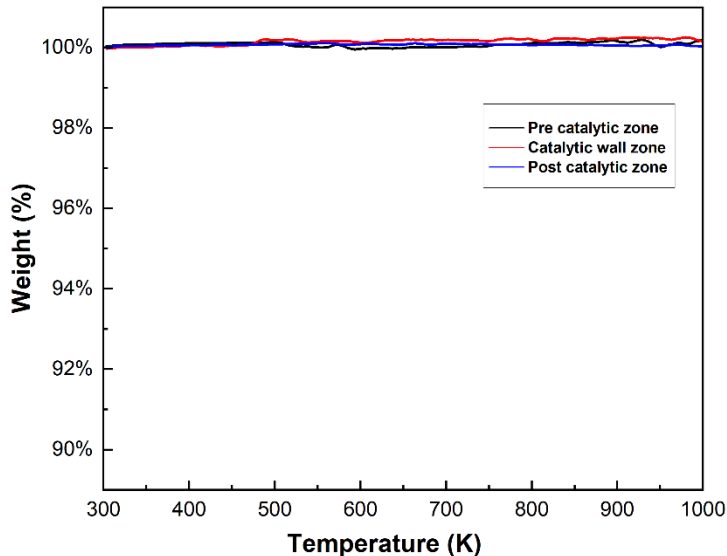


**Figure 3.7.** TGA curve of coke formed on ACWR after TOS = 6 hrs of NMC reaction. (Reaction condition: 0.48 L h<sup>-1</sup> gas flow with CH<sub>4</sub>:Ar ratio = 7, 101.325 kPa pressure, 0.2 g Fe/SiO<sub>2</sub> catalyst in ACWR, Fe concentration = 0.075 wt%; Fuel combustion: 165 L h<sup>-1</sup> gas flow with CH<sub>4</sub>:Air ratio = 0.1, 101.325 kPa pressure, 0.1 g Pt/Al<sub>2</sub>O<sub>3</sub> catalyst, Pt concentration = 1.0 wt%)

Even though the post reaction Fe/SiO<sub>2</sub> catalytic wall layer appeared black, the TGA measurement showed no weight loss. Furthermore, the post reaction upstream and downstream had no discolor and their TGA measurements showed no weight loss either. Thus, the coked formed from NMC reaction is negligible. Some minor carbon deposit on the Fe/SiO<sub>2</sub> catalytic layer is likely to occur during initial catalyst activation to form iron carbide species and the low surface area of Fe/SiO<sub>2</sub> catalyst prevents further coke formation on the surface.

By comparing the performance of our autothermal catalytic wall reactor at 1000 C with the results reported in literature<sup>47,48,78,135</sup>, the ACWR showed remarkable highest olefins selectivity of 92.1% while maintaining methane conversion at 11.0% and negligible coke formed. Postma et al's work<sup>47</sup> confirmed that preheating reaction gas

would cause soot formation in gas phase and increase coke selectivity. The ACWR offered minimal preheating to the reaction mixture before contacting the catalytic wall. On the otherhand, the conventional heating method had unavoidable extended preheating effect before reaching desired reaction temperature due to less effective heat transfer from external heating source which can be observed in Figure 3.3c.

Furthermore, the Fe/SiO<sub>2</sub> catalyst activates methane to form ethylene on the catalyst surface<sup>130</sup> and the homogeneous propagation reaction over Fe/SiO<sub>2</sub> has been reported by Puenete-Urbina et al<sup>136</sup>, where propargyl radicals are important intermediate species between C<sub>2</sub> and aromatic products. The wall reactor design provides millisecond contact time for methane activation on the catalytic wall, but the rapid cooling in the downstream due to the depletion of methane on the combustion side has severely reduced the propagation reaction, as most gas phase reactions were limited at the free volume of high temperature catalytic wall section.

To further check the Pt/Al<sub>2</sub>O<sub>3</sub> catalyst layer uniformity, we used laser microscope to measure the surface roughness of the Pt/Al<sub>2</sub>O<sub>3</sub> catalytic wall. In Figure 3.8a, we took a photo of the outer surface of the reactor tube, where the x-axial direction along the catalytic wall reactor and y-axial direction followed the radial direction of the reactor. The surface height of the same photo was measured in Figure 3.8b. There is minor height difference along the x-axis for rough. The significant height change along the y-axis was caused by the nature of the cylindrical shape of the reactor. To better quantify the surface uniformity, the thickness variation was measured on 3 different locations paralleling along the catalytic wall reactor as shown in Figure 3.8c. the Ra (arithmetic average of profile height deviations from the mean) values of 12.3, 22.5

and 13.4  $\mu\text{m}$ . Combining with the thickness variant result from Figure 3.8d, we could see some height variant of Pt/Al<sub>2</sub>O<sub>3</sub> layer within 60  $\mu\text{m}$ .

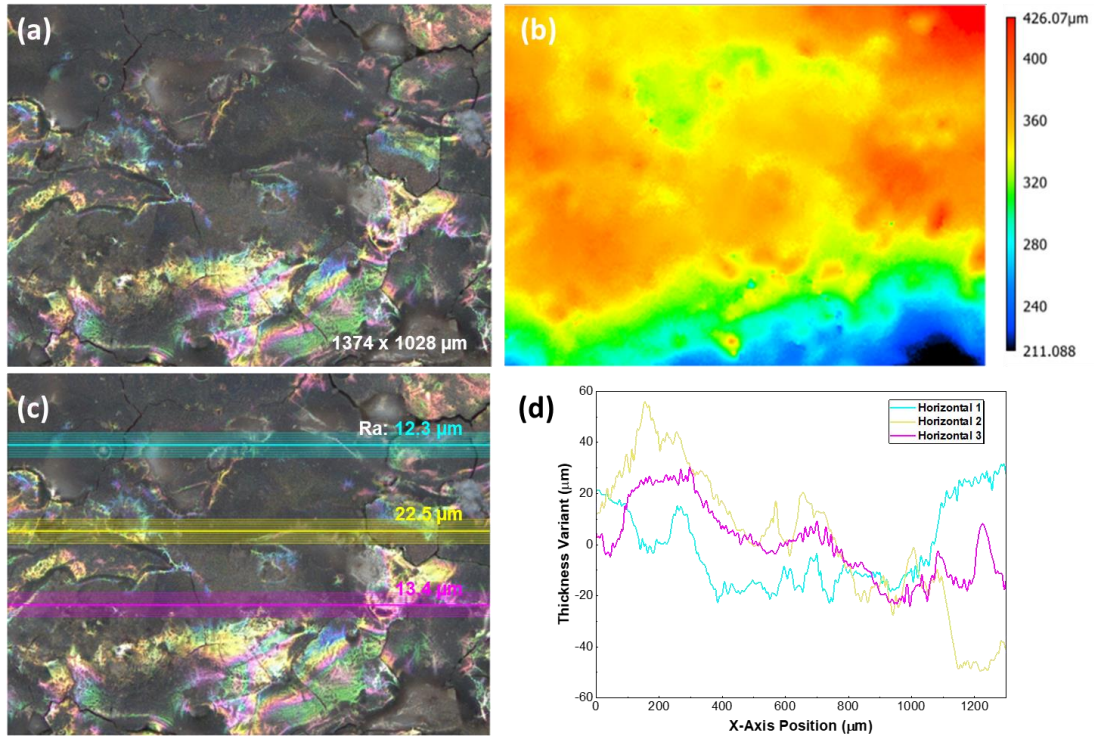


**Figure 3.8.** (a) Laser microscope image of Pt/Al<sub>2</sub>O<sub>3</sub> surface on ACWR the surface size is 1374 x 1028  $\mu\text{m}$ . (b) Height scan of Pt/Al<sub>2</sub>O<sub>3</sub> surface. (c) Horizontal scan along the reaction tube. The Ra values of Horizontal line 1, 2 and 3 are 12.3, 22.5 and 13.4  $\mu\text{m}$ . (d) Thickness variation of the Pt/Al<sub>2</sub>O<sub>3</sub> layer surface on Horizontal line 1, 2 and 3 based on the average mean thickness. Color code of (c) and (d) is identical.

To obtain the Fe/SiO<sub>2</sub> catalyst uniformity, the catalytical wall zone of the ACWR (90 mm) was broken into 3 parts and 3 cross-section SEM images were shown in Figure 6. The average Fe/SiO<sub>2</sub> catalytic layer thicknesses were  $584.4 \pm 112.8$ ,  $525.8 \pm 129.2$  and  $595.0 \pm 129.2$   $\mu\text{m}$  at 0, 35 and 90 mm respectively.

To obtain the Fe/SiO<sub>2</sub> catalyst uniformity, the catalytical wall zone of the ACWR (90 mm) was broken into 3 parts and 3 cross-section SEM images were shown in Figure 3.9. The average Fe/SiO<sub>2</sub> catalytic layer thicknesses were  $584.4 \pm 112.8$ ,  $525.8 \pm 129.2$  and  $595.0 \pm 129.2$   $\mu\text{m}$  at 0, 35 and 90 mm respectively.

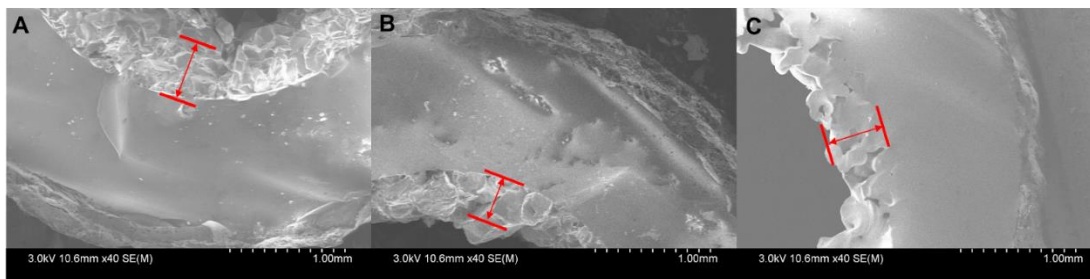


**Figure 3.9.** SEM images showing a cross-section view of ACWR, where Fe/SiO<sub>2</sub> catalyst layer is fused onto the inner wall surface and their thickness is marked in red. The cross-section position of the catalytic wall zone is (A) 0 mm, (B) 35 mm and (C) 90 mm.

We understood that the axial distribution of Pt on the outer wall would influence the local heat generation. However, it was difficult to obtain local methane conversion for methane combustion reaction and was not in the scope of this study. In this study, we used methane combustion reaction on Pt/Al<sub>2</sub>O<sub>3</sub> as a tool to demonstrate, for the first time, an autothermal catalytic wall reactor was built for NMC reaction and temperature profile along the reactor played an important role on mitigating coke formation by eliminating secondary homogeneous reaction. In our current continuing work, we intend to obtain local specie concentrations, local temperatures, and study their influence on both NMC, methane combustion reaction and the advantage of catalytic wall reactors with specifically built analysis instrument.

### 3.3.4 Simulation of gas velocity profile and radial temperature profiles of ACWER using COMSOL

The gas velocity profile and radial temperature could influence the performance of ACWR process, but they were difficult to measure accurately in experiments due to the small diameter of the reactor tube. 2D-axisymmetric steady-state COMSOL simulations were performed to understand the effects of gas flow velocities and

temperature profile along the radial direction after coupling with NMC and methane combustion reaction. Figure 3.10 shows the model geometry of the ACWR.

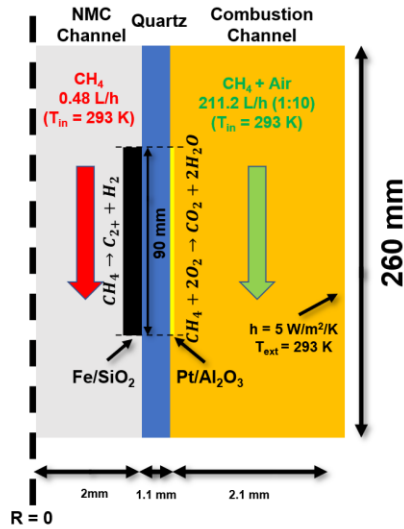


**Figure 3.10.** Reactor schematic and parameters of autothermal catalytic wall reactor used for COMSOL simulation. A cocurrent flow is illustrated.

The following assumptions were made: 1. No slip-conditions are used for flow modeling, with symmetry condition imposed at  $R = 0$ . 2. All gas flows enter the reactor at room temperature, with an open boundary condition at the outlet allowing for gas and heat to be carried away from the modeling domain. 3. The thin  $\text{Pt}/\text{Al}_2\text{O}_3$  layer for methane combustion reaction has little to no effect on the gas flow velocity profile, therefore it is treated as a boundary in simulations. The  $\text{Fe}/\text{SiO}_2$  for NMC reaction is a porous layer and its porosity is 0.5. 4. For thermal modeling, the heat of combustion of methane increases the temperature in the combustion chamber. Due to the lack of simplified reaction kinetics for methane combustion reaction, especially under sudden temperature ramping and cooling, the heat flux is assumed to be uniform over the surface area of the catalyst (and hence the entire axial length of the catalyst zone) and determined using the overall methane conversion (i.e., 100%) and inlet flow rates. 5. A

wavelength-independent radiative emissivity of 0.65 and convective heat transfer coefficient of 5 W/m<sup>2</sup>/K are used at the outer environment boundaries to account for heat exchange between surfaces and losses to the ambient. These are based on typical values encountered in the literature [2] and deemed reasonable owing to the complexity in determining these quantities precisely.

Under these assumptions, we model the temperature profile in the NMC reaction chamber arising from complete combustion over the whole of the catalyst layer and find a reasonable agreement with experimental measurements, as indicated in Figure 3.11. The model does not capture the broadening of the temperature profile around peak temperatures, potentially arising due to radiative transport heating surfaces upstream and downstream. Regardless, in physical agreement with experiments, higher peak temperatures are observed with a higher flow rate as complete methane combustion is assumed, leading to larger heat of reaction. Notably, the model qualitatively agrees with the experimental hypothesis that the asymmetry of temperature profile around the peak underlies the ACWR reactor. In countercurrent flow, a rapid quenching is observed post-peak temperature in the reaction zone. In contrast, when the flow is reversed (i.e., cocurrent), the quenching will be slower.

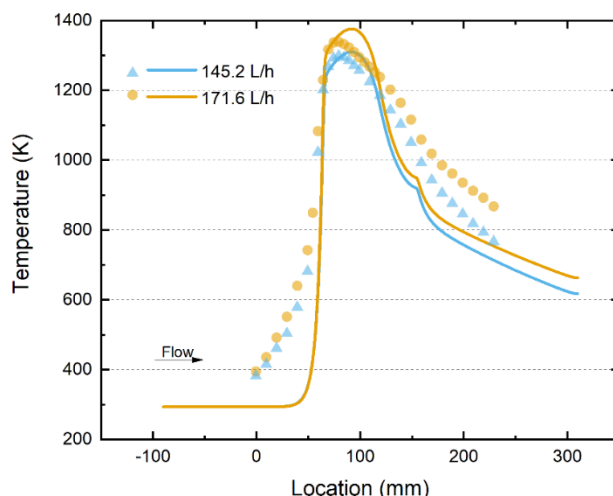


**Figure 3.11.** Axial temperature comparison of steady-state simulation and experiment results at center line of combustion chamber with flow rates of 145.2 and 171.6 L h<sup>-1</sup> (CH<sub>4</sub>: Air ratio = 0.1). The arrow indicates the cocurrent flow in the NMC chamber. First, the flow was simulated in the NMC channel to understand the time-scale that enables efficient catalytic performance.

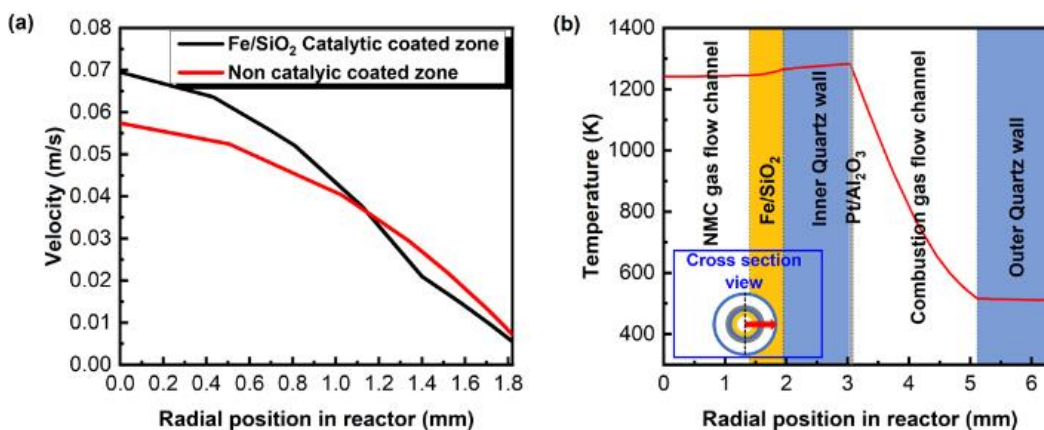


**Figure 3.12.** (a) Modeled maximum local gas velocity (left-y axis) and local temperature (right y-axis, red) in the NMC chamber as a function of iron silica catalyst coating thickness. (b) Radial temperature profile across the whole reactor at 130 mm axial position for combustion chamber gas flow of 145.2 L h<sup>-1</sup> (red) and 171.6 L h<sup>-1</sup> (blue). (NMC channel: Ar flow 0.48 L h<sup>-1</sup>, coating thickness 0.55mm; combustion channel CH<sub>4</sub>:Air ratio = 0.1, 101.325 kPa pressure; co-current flow mode.)

The simulation indicated that the maximum velocity at the high temperatures in the NMC chamber could increase from ~100 mm/s to 200 mm/s when the catalyst coating thickness is changed from 0.2 mm to 0.55 mm (used in the experimental study). Thus, at this experimental coating thickness, the residence time over the catalytic length

(~90 mm) could be as low as ~0.5 s while the time required for a reactant methane molecule to diffuse to the catalytic layer surface is an order of magnitude smaller, enabling sufficient contact for NMC reaction to proceed without diffusion limitation.

In our experiment, all gas flows have Reynolds numbers lower than 500. In laminar flow, the time for methane to diffuse from the center of the tube to the catalytic surface is defined as contact time. It can be approximately using Equation 2.1 below,

$$t \cong \frac{x^2}{D} \quad 2.1$$

where x is the gas transport distance (mm) and D is an approximate gas phase diffusion coefficient (mm<sup>2</sup>/s). **Table 2.1** lists the calculated results.

**Table 2.1.** Contact time analysis for reaction gases in the catalytic wall reactor.

Cases	Diffusion distance (x, mm)	Diffusion coefficient <sup>137</sup> (D, mm <sup>2</sup> /s)	Contact time (t, s)
NMC in non-catalytic zone	2	100	0.04
NMC in catalytic zone	1.45	100	0.02
Methane combustion in non-catalytic zone	2.075	100	0.04
Methane combustion in catalytic zone	2.070	100	0.04

The residence times on both sides of the reactor using inlet room temperature flow can be calculated from:

$$t_{res_{NMC}} \cong \frac{V_r}{Flow\ rate} \cong \frac{\left(\frac{4\ mm}{2}\right)^2 * 3.14 * 90\ mm}{20\ cm^3/min * 60\ s/min} = 3.39\ s$$

$$t_{res_{methane\ combustion}} \cong \frac{\left(\left(\frac{10.5\ mm}{2}\right)^2 - \left(\frac{6.35\ mm}{2}\right)^2\right) * 3.14 * 90\ mm}{3740\ cm^3/min} = 0.079\ s$$

Additionally, the reduction of the contact time in the NMC layer impacted the maximum gas temperature, with the model predicting a decrease of peak temperature with an increase in catalyst coating thickness. Future designs to enable the maximum

throughput from the proposed modular system by optimizing the diameter of the NMC chamber in conjunction with catalyst layer thickness could be envisioned. On the fuel combustion side, the velocity profile was less sensitive to the catalyst coating region around its experimental value owing to its small thickness ( $\sim 0.03$  mm; result not shown). However, the radial temperature profiles depend on the flow rates in the combustion channel (Figure 3.12b). At a higher flow rate of methane, assuming a complete conversion (the experimental methane conversion of combustion reaction is 99.5%), higher peak temperatures were observed. Specifically, at  $145.2 \text{ L h}^{-1}$  flow, the Pt/Al<sub>2</sub>O<sub>3</sub> catalyst layer had the highest temperature of  $\sim 1310 \text{ K}$ . A temperature drop towards the NMC channel direction occurs as heat is conducted through quartz and silica (thermal conductivity  $\kappa \sim 1.5 \text{ W/m-K}$ ). The temperature drops to  $\sim 1295 \text{ K}$  upon reaching the reactor's centerline, where a  $0.48 \text{ L h}^{-1}$  flow of Ar is flowing. This NMC temperature could be lower if the endothermicity of the reaction is accounted for. In contrast to the NMC chamber, a sharp temperature drop along radial direction in the combustion reaction channel towards the outer shell was caused by the strong convective and radiative heat losses from catalytic reactor walls. Minimizing these losses using insulation and shielding are potential pathways to maximize system efficiency. It should be noted that adiabatic operation of the ACWR only required  $0.18 \text{ L h}^{-1}$  CH<sub>4</sub>/air flow (CH<sub>4</sub>:air ratio of 0.1) for fuel combustion to supply heat to the  $1.2 \text{ L h}^{-1}$  CH<sub>4</sub>/Ar flow (CH<sub>4</sub>:Ar ratio of 9) in NMC channel. This case was used to achieve 36.4% methane conversion, as shown earlier in Figure 3.4f. Overall, it was evident from simulations that the close contact between the endothermic NMC and exothermic

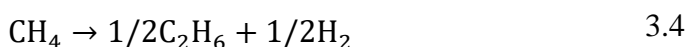
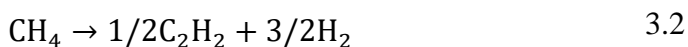
fuel combustion reactions enabled by catalyst coatings on opposite sides of the reactor wall.

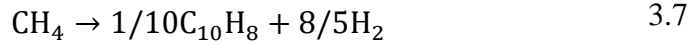
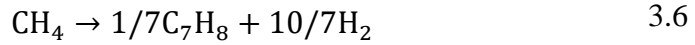
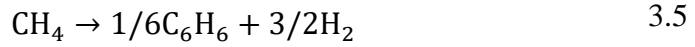
### 3.3.5 *Potential CO<sub>2</sub> emission free ACWR for NMC reaction*

Besides C<sub>2+</sub> products, NMC generates H<sub>2</sub> co-product, which could be used as the fuel for the combustion reaction in the ACWR. Our initial study demonstrated the success of NMC in achieving high C<sub>2+</sub> yield and negligible coke enabled by the methane fuel combustion over Pt/Al<sub>2</sub>O<sub>3</sub> wash-coated catalyst on the reactor wall. However, it cannot be denied that methane combustion carbon emissions via CO<sub>2</sub> production. The replacement of methane by H<sub>2</sub> co-product from NMC would eliminate these carbon emissions while retaining the autothermal operation. To demonstrate this potential, an energy balance calculation for the coupled NMC and H<sub>2</sub>/air fuel combustion reactions in ACWR was conducted with methane conversion and product selectivity data from high benzene yield shown in Figure 3.4f.

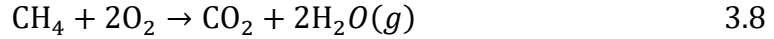
The following assumptions were implemented for the energy calculation: (1) coke was assumed to be solid carbon; (2) All hydrocarbons and coke products were assumed to be formed via one-step reaction to simplify the calculation (Eqn 3.2-3.7); (3) The reaction temperature was assumed to be the peak temperature measured; (4) The reactor was adiabatic.

Product formation reactions for the endothermic NMC include:





The exothermic methane combustion was:



The heat of formation of each component at 1 atm and reaction temperature was calculated based on the following equation:

$$\Delta H_f(T) = \Delta H_f^o + \int_{T_o}^T \Delta C_p dt \quad 3.9$$

$$\Delta H_f(T) = \Delta H_f^o + \int_{T_o}^T a + bT + cT^2 + dT^3 dt \quad 3.10$$

where  $\Delta H_f^o$  (kJ/mol) is the standard enthalpy of formation,  $\Delta C_p$  (kJ/mol/K) is the heat capacity of the component, T (K) is the reaction temperature and  $T_o$  is 298 K, a, b, c and d are the parameters of the heat capacity function of temperature. **Table 2.2** lists the standard enthalpy of formation and heat capacity parameters for each component.

**Table 2.2.** Standard enthalpy of formation and heat capacity parameters of reactant and products in the NMC and methane combustion reaction.

Gas	$H_f^o$ (kJ·mol <sup>-1</sup> ) <sup>a</sup>	a	b	c	d	e
CH <sub>4</sub>	-74.5	19.875	5.02E-02	1.27E-05	-1.10E-08	N/A
C <sub>2</sub> H <sub>2</sub>	227.5	21.799	9.21E-02	-6.52E-05	1.82E-08	N/A

C <sub>2</sub> H <sub>4</sub>	52.5	3.95	1.56E-01	-8.34E-05	1.77E-08	N/A
C <sub>2</sub> H <sub>6</sub>	-83.8	6.895	1.73E-01	-6.40E-05	7.28E-09	N/A
C <sub>6</sub> H <sub>6</sub>	82.9	-36.193	4.84E-01	-3.15E-04	7.76E-08	N/A
C <sub>7</sub> H <sub>8</sub>	50.10	0.29	4.7052E-3	-1.57E-5	0	N/A
C <sub>10</sub> H <sub>8</sub>	105.6	67.099	4.32E-2	9.17E-4	-1.00E-6	3.09E-10
H <sub>2</sub> O	-241.83	32.24	-1.92E-3	1.06E-5	-3.6E-9	N/A
H <sub>2</sub>	0.00	29.088	-1.92E-3	4E-6	-8.7E-10	N/A
O <sub>2</sub>	0.00	29.11	-3.86E-6	1.75E-6	-1.07E-8	N/A
CO <sub>2</sub>	-393.5	19.8	7.34E-2	-5.6E-5	1.71E-8	N/A
Ar	0	20.786	2.8259E-7	-1.464E-7	1.092E-7	-3.66E-8
N <sub>2</sub>	0	31.15	-1.36E-2	2.68E-5	-1.17E-8	N/A

Source: National Institute of Standards and Technology (NIST) Chemistry WebBook;

The heat of the reaction is calculated based on the following equation:

$$\Delta H_{rxn,i}(T) = \sum v_i \Delta H_{f,i}(T) \quad 3.11$$

where  $v_i$  are the stoichiometric coefficients for each component and  $\Delta H_{f,i}$  is the enthalpy of formation of each component in each reaction, and T (K) is the reaction temperature.

The heat of the NMC and methane combustion reaction was calculated from

$$\Delta H_{NMC}(T) = Conversion_{NMC} * \sum Selectivity_{NMC,i} * \Delta H_{rxn,i}(T) \quad 3.12$$

$$\Delta H_{comb}(T) = Conversion_{comb} * \sum Selecitivity_{comb,i} * \Delta H_{rxn,i}(T) \quad 3.13$$

The energy required to allow the reactants to reach the reaction temperature can be calculated as

$$Heat_{NMC}(T) = \sum f_i \int_{T_0}^T \Delta C_{p,i} dt \quad 3.14$$

$$Heat_{comb}(T) = \sum f_i \int_{T_0}^T \Delta C_{p,i} dt \quad 3.15$$

Here  $f_i$  is the fraction of reactants and  $\Delta H_f^0$  (kJ/mol) is the standard enthalpy of formation.

To achieve the goal of zero greenhouse gas emission, H<sub>2</sub> combustion was analyzed to couple with the NMC reaction. The combustion was set to the reaction stoichiometric ratio, where H<sub>2</sub>: Air flow ratio is 1:2.5.

$$\begin{aligned} \Delta H_{Comb,H_2}(1423 K) &= \Delta H_{rxn,comb,H_2}(1423 K) + Heat_{comb,H_2}(1423 K) \\ &= (-466.7 \text{ kJ/mol}) + 31 \text{ kJ/mol} = -435.7 \text{ kJ/mol} \end{aligned}$$

If the reaction operated under adiabatic conditions, the H<sub>2</sub> mole flow rate ( $n_{H_2}$ ) required for combustion reaction to sustain autothermal operation is

$$n_{H_2} = \frac{1}{3.5} * \frac{1.2 \text{ kJ/h}}{435.7 \text{ kJ/mol}} = 7.9 * 10^{-4} \text{ mol/h}$$

Based on the experimental hydrogen yield and methane mole flow rate, the H<sub>2</sub> produced rate ( $n_{NMC,H_2}$ ) from NMC reaction at 1423 K is determined to be

$$n_{NMC,H_2} = 43.4\% * 0.0103 \text{ mol/h} = 4.5 * 10^{-3} \text{ mol/h}$$

Thus, the percentage of H<sub>2</sub> generated from NMC reaction for sustaining combustion reaction can be determined as

$$\% H_2 \text{ required from NMC} = \frac{7.9 * 10^{-4} \text{ mol/h}}{4.5 * 10^{-3} \text{ mol/h}} * 100 = 17.6\%$$

Under adiabatic conditions, the combustion of 17.6% H<sub>2</sub> co-product generated from NMC is sufficient to sustain the NMC reaction. A system-level framework analysis suggests the >25% methane conversion and <20% coke selectivity is viable to realize the economic feasibility of the NMC process.<sup>44</sup> The NMC reaction in the ACWR surpasses all these performance metrics, indicating strong techno-economic viability.

### 3.4 Conclusion of Chapter 3

In summary, a catalytic wall reactor with millisecond contact time and sharp temperature profiles was innovated for the first time for self-sustaining NMC with high hydrocarbon product selectivity and negligible coke formation. The reactor is made of a quartz tube with NMC and fuel combustion catalyst coatings on opposite sides of the tube wall. The intimate contact between the catalysts and reactor wall enables efficient heat transfer from the exothermic fuel combustion to the endothermic NMC, offering high local temperature at active sites for methane activation. The contact time of methane reactant to the reactive wall is shorter than those of the hydrocarbon products. The catalyst zoning in the fuel combustion channel enables a sharp temperature gradient and narrow isothermal zone. The control of contact time and sharpening spatial temperature in the reactor effectively suppress the secondary and follow-on reactions and thus coke formation. By tuning the gas flow rate in each reaction channel and the flow direction, the axial temperature profile was modulated to tune the methane conversion and product selectivity towards C<sub>2</sub> or aromatic products. By optimizing the gas flow rates in both channels, high methane conversion, as well as tunable

hydrocarbon selectivity, was achieved. The system could potentially be driven by combusting the sole co-product  $H_2$  to create a self-sustained operation of NMC without greenhouse emissions.

## Chapter 4: A Spatially Resolved Analysis on Selective Nonoxidative Coupling of Methane in Autothermal Catalytic Wall Reactor

### *4.1 Introduction*

Methane, the primary component of natural gas, is a valuable alternative resource with the potential to replace crude oil in the production of chemicals and fuels<sup>70</sup>. Current methods for methane conversion include indirect processes such as conversion into synthesis gas followed by Fischer-Tropsch synthesis of higher hydrocarbons, and oxidative coupling reactions<sup>138,139</sup>. However, these methods often suffer from significant carbon dioxide emissions, high operation and capital costs. NMC has emerged as a promising alternative, offering a single-step process for converting natural gas into value-added petrochemicals like ethylene and benzene<sup>48</sup>. The development of more efficient and economically viable chemical reactor systems for NMC is crucial for the successful implementation of this technology.

Traditionally, the NMC reaction has faced challenges, including low CH<sub>4</sub> conversion, low product yield, and catalyst durability, due to the endothermic nature of the reaction, coke formation and catalyst deactivation<sup>45,80</sup>. Current research efforts aim to enhance the mechanism understanding of the process, optimize catalyst formulations, and develop efficient reactor systems to pave the way for a more sustainable and economically viable methane conversion technology<sup>49,135,140,141</sup>. The state-of-the-art for non-oxidative methane conversion (NMC) has seen significant advancements in recent years, focusing on the development of novel catalysts and reactor designs to overcome the challenges associated with this highly endothermic process. Metal-loaded zeolite catalysts<sup>74</sup> and iron-modified silica catalysts<sup>48</sup> have

demonstrated promising performance in NMC, with the latter exhibiting high CH<sub>4</sub> conversion and C<sub>2+</sub> yields at elevated temperatures. However, issues such as low conversion rates, rapid catalyst deactivation, and the necessity for high heat supply remain challenges for the widespread adoption of NMC. A mechanistic investigation into the Fe/SiO<sub>2</sub> catalyst revealed that a complex heterogeneous-homogeneous reaction network underlies its performance. The silica lattice-confined Fe species initiate CH<sub>4</sub> dehydrogenation to generate methyl and hydrogen species, enabling a series of subsequent surface and gas-phase reactions to form dehydrogenated and cyclized larger hydrocarbon products.

Efforts have also been made to develop novel reactor designs to address these issues. Su et al. developed a millisecond catalytic wall reactor with an Fe/SiO<sub>2</sub> catalyst for non-oxidative methane conversion aimed at addressing the coking issue<sup>49</sup>. Mann et al. developed a hydrogen-permeable membrane reactor aiming to increase methane conversion<sup>142</sup>. However, the product selectivity favors the formation of aromatics (>60%) and coke. Recent studies from Qi et al. have developed a programmable heating and quenching technique for catalyst-free methane pyrolysis under non-equilibrium conditions, which leads to significantly higher selectivity (>75%) to C<sub>2</sub> products<sup>143</sup>. Nevertheless, the C<sub>2</sub> yield remains below 12% due to the uneven spatial uniformity of temperature. Some studies have indicated the importance of temperature profiles in promoting methane conversion and desired hydrocarbon product selectivity<sup>47</sup>. In chapter 3, we demonstrated an autothermal catalytic wall reactor that coupled the exothermic methane oxidation and non-oxidative coupling of methane reactions. This reactor achieved a tunable productivity of 78% C<sub>2</sub> or 75% aromatics product selectivity

with 26% and 36% methane conversion, respectively. The reactor exhibited limited coke formation, achieved through a non-uniform axial temperature profile along the reactor from rapid heating and quenching effects. However, the detailed interactions among catalytic reactions and gas-phase reactions remain uncertain within the reactor at elevated reaction temperatures.

Although conventional end-pipe testing approaches provide useful information regarding the effectiveness of catalytic systems, they do not reveal important intra-reactor information, especially when reaction pathways involve both surface and gas-phase reactions. Furthermore, spatially resolved reaction profiles, temperature evolution, intermediate formation/removal, deactivation, and reaction sequence are all unobtainable through the end-pipe approach. Oak Ridge National Laboratory has developed the spatially resolved capillary-inlet mass spectroscopy system (SpaciMS) to demonstrate a minimally invasive technique for accessing spatially resolved temperature and gas composition information about reactions occurring inside monolith channels<sup>144</sup>. This can help address the limitations associated with conventional catalyst evaluation and design. The instrument has been successfully implemented in a wide range of conditions, including catalyst beds on both bench-scale and full-engine platforms, advanced diesel combustion, non-reacting gas mixing, electrically active non-thermal plasma reactor chemistry, and fuel cells.[] In these applications, the SpaciMS has been configured to provide 104 ms<sup>-1</sup> s temporal resolution and quantify species concentrations in the 10 ppm to tens of percent ranges.[] Although these applications have required concentration gradients to be measured only on centimeter scales, the spatial resolution is limited only by the ability to control

capillary translation; for example, 2 mm spatial resolution should be readily feasible. The SpaciMS has provided unique detail regarding the network and sequence of catalyst chemistry and previously unavailable insights into improving the performance efficiency of diesel-catalyst systems. Similar unique insights into the fundamentals of catalytic wall reactors are expected from SpaciMS applications.

In this chapter, we developed a customized SpaciMS system to accurately resolve NMC transients in terms of instantaneous reaction and temporal dynamics in an autothermal catalytic wall reactor that couples the exothermic methane oxidation reaction with the endothermic NMC reaction. The oxidation catalyst washcoat Pt/ $\gamma$ -Al<sub>2</sub>O<sub>3</sub> and NMC catalyst washcoat Fe/SiO<sub>2</sub> are coated on the external surface and internal surface of the cylindrical quartz reactor, respectively. This integration leads to a non-uniform temperature profile that enhances the formation of valuable light hydrocarbon products, such as ethylene. This paper describes the first application of the SpaciMS measurement of NMC species transient associated with manipulated axial temperature profiles and intra-reactor species distribution. Measurements are made at common NMC reaction temperatures with Fe/SiO<sub>2</sub> (900-1200 °C) to demonstrate the instrument's applicability at extreme temperatures with a simple setup.

## *4.2 Experiments*

### *4.2.1 Catalyst synthesis*

The Fe/SiO<sub>2</sub>, employed as an NMC catalyst, was prepared as previously reported in the last chapter, using a mixture of fayalite (Fe<sub>2</sub>SiO<sub>4</sub>) and quartz (SiO<sub>2</sub>) particles. The Fe<sub>2</sub>SiO<sub>4</sub> compound was synthesized through a sol-gel method, as

described by DeAngelis et al [33]. The particle mixture underwent ball milling at ambient temperature for 12 hours and was heated to 1973 K for 6 hours under stagnant air in a high-temperature furnace (Sentro Tech, ST-1700C-101012) to produce Fe/SiO<sub>2</sub>. The Fe/SiO<sub>2</sub> catalyst was then crushed, and ball milled into a fine powder for the fabrication of the autothermal catalytic wall reactor.

The Pt/ $\gamma$ -Al<sub>2</sub>O<sub>3</sub>, utilized as a methane oxidation catalyst, was synthesized directly on the external surface of the cylindrical reactor, which will be described in the following section. Before the fabrication process, a 16.67 wt.% chloroplatinic acid solution was prepared using chloroplatinic acid hydrate (Sigma-Aldrich, >99.9%) and deionized (DI) water. Additionally, a 10 g alumina-based slurry was prepared with  $\gamma$ -Al<sub>2</sub>O<sub>3</sub>, chromium nitrate, yttrium nitrate, and DI water.

#### 4.2.2 Fabrication of Autothermal Catalytic Wall Reactor and Catalytic Wall Reactor

The autothermal millisecond catalytic wall reactor consisted of two concentric quartz tubes, as illustrated in Figure 4.3. The inner tube featured an outside diameter of 6.35 mm and a thickness of 1.00 mm, while the outer tube had an outside diameter of 12.7 mm and a thickness of 1.20 mm. To create the Fe/SiO<sub>2</sub> washcoat, the Fe/SiO<sub>2</sub> catalyst was initially packed into the smaller diameter quartz tube and softened by briefly contacting a hydrogen flame. This step was repeated to ensure uniform dispersion and proper anchoring on the inner wall of the quartz tube. To form the Pt/ $\gamma$ -Al<sub>2</sub>O<sub>3</sub> coating on the outer surface of the smaller diameter tube, the alumina-based slurry was applied in droplets on the EtOH-cleaned surface, followed by brief treatment with a hydrogen flame. This process was repeated until the color of the quartz tube transformed from transparent to a uniform milky white. Subsequently, the

chloroplatinic acid solution was applied to the alumina surface in single drops and treated with a propane torch in a repeating manner. Finally, the washcoat region was exposed to a hydrogen flame one last time to ensure complete decomposition of the metal precursor and secure anchoring of the Pt species. A uniformly dark black washcoat indicated the successful coating of Pt/ $\gamma$ -Al<sub>2</sub>O<sub>3</sub> on the quartz reactor.

During the reaction, the exothermic methane combustion gases (i.e., CH<sub>4</sub> and air) flowed through the annulus region of the reactor, while the CH<sub>4</sub> in the endothermic NMC flowed through the inner tube. The catalyst coatings on the catalytic wall surface had a length of approximately 90.00 mm on both sides. The outer tube was insulated with a ceramic fiber blanket and ceramic cylinder. Throughout the reactions, the heat generated from catalytic combustion transferred across the quartz wall, driving the endothermic NMC reaction occurring inside the tube.

The single layer Fe/SiO<sub>2</sub> catalytic wall reactor was fabricated in a 12.7mm tube, followed the exact same procedures without the Pt/Al<sub>2</sub>O<sub>3</sub> washcoat loading. The single layer catalytic wall reactor was operated in conventional electrical furnace.

#### 4.2.3 *Spatially resolved capillary-inlet mass spectroscopy system (SpaciMS)*

The SpaciMS employed in this study, as shown in Figure 1, was based on a Benchtop Mass Spectrometer (Thermo Fisher) using electron ionization and equipped with an electron multiplier. Fused silica capillaries (Restek, 1 m long, 0.53 mm I.D., 0.69 ± 0.05 mm O.D.) were used to transport samples from selected locations throughout the sampling port in the NMC channel to a stainless-steel tee (Valco) with fused silica adapters (Valco). The sample flow rate was approximately 10 L min<sup>-1</sup> for a working capillary, with gases continuously drawn through the connected capillary

while other capillaries were sealed at the terminal. From the tee, the sample stream was directed to the mass spectrometer (MS) for analysis through a 1/16" stainless steel tubing. To prevent the condensation of aromatics, the sample lines outside of the reactor were heated to 200 °C using wrapped heating tapes, and the MS inlet was heated to 250 °C. The SpaciMS typically operated in a selected-ion-monitoring mode, and concentrations of selected species ( $H_2$ ,  $CH_4$ ,  $C_2H_6$ ,  $C_2H_4$ ,  $C_2H_2$ ,  $C_6H_6$ ,  $C_7H_8$ ,  $C_{10}H_8$ , and Ar) were analyzed.

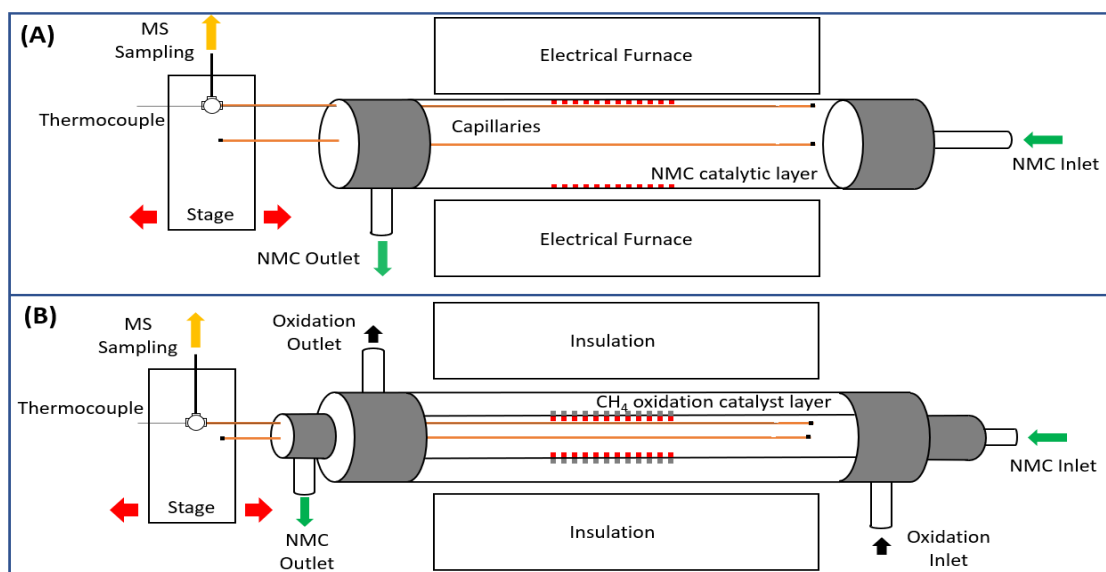


**Figure 4.1.** Axial and radial temperature and concentration profile probing via SpaciMS setup for nonoxidative methane conversion in: (A) Single layer Fe/SiO<sub>2</sub> catalyst wall heated with conventional furnace; (B) Autothermal catalytic wall reactor coupled with methane oxidation reaction.

The temperature acquisition method involved inserting a 0.254 mm O.D. ungrounded type K thermocouple (Omega Engineering) through the Valco tee and into the capillary column. The tip of the thermocouple was aligned with the sample port located inside the reactor, as shown in Figure 4.1 to ensure accurate temperature measurement of vacuum extracted samples. To collect axial temperature profile at different radial positions, the capillary goes through two pieces of alumina monolith,

which were placed on each side of non-heating zones in the reactor and functioning as support.

### 4.3 *Results and Discussion*

#### 4.3.1 *Performance of spatially resolved standard catalytic wall reactor*

The primary focus of this study is the in-depth performance analysis of a Fe/SiO<sub>2</sub> catalytic wall reactor employed for the non-oxidative methane conversion (NMC) reaction. In this context, the spatially resolved temperature profiles and product gas concentration results for the Fe/SiO<sub>2</sub> catalytic wall reactor, heated using a horizontal furnace with a 330 mm heating zone at 1198K, are presented in Figure 4.2. This study, conducted at relatively lower temperatures, aspires to discern the product species resulting from surface reaction.

As demonstrated in Figure 2a, the axial temperature profile is contingent on the radial position within the NMC reaction channel. As the CH<sub>4</sub>/Ar mixture (CH<sub>4</sub>/Ar =7:33, 40 mL min<sup>-1</sup> flow rate) enters the heating zone, a quick rise and subsequent fall in the gas temperature is observed near the reactor wall, which can be attributed to the heat transfer boundary layer present at the quartz reactor's inner wall.

C<sub>2</sub> chemistry plays a pivotal role in the NMC gas phase reaction, following the equilibrium reactions: C<sub>2</sub>H<sub>2</sub> <-> C<sub>2</sub>H<sub>4</sub> <-> C<sub>2</sub>H<sub>6</sub>. Figures 3.2(b), (c), and (d) reveal that the C<sub>2</sub>H<sub>4</sub> concentration at 210 mm is nearly three times higher than that of C<sub>2</sub>H<sub>2</sub> and C<sub>2</sub>H<sub>6</sub> at the 210 mm axial position close to the reactor wall. This elevated ethylene concentration near the reactor wall provides empirical evidence for the catalytic coupling of methane to form ethylene over the Fe/SiO<sub>2</sub> surface. Further, a higher

concentration of  $C_2H_2$  at the reactor's center suggests that  $C_2H_2$  is likely a product of  $C_2H_4$  dehydrogenation through a gas-phase reaction.

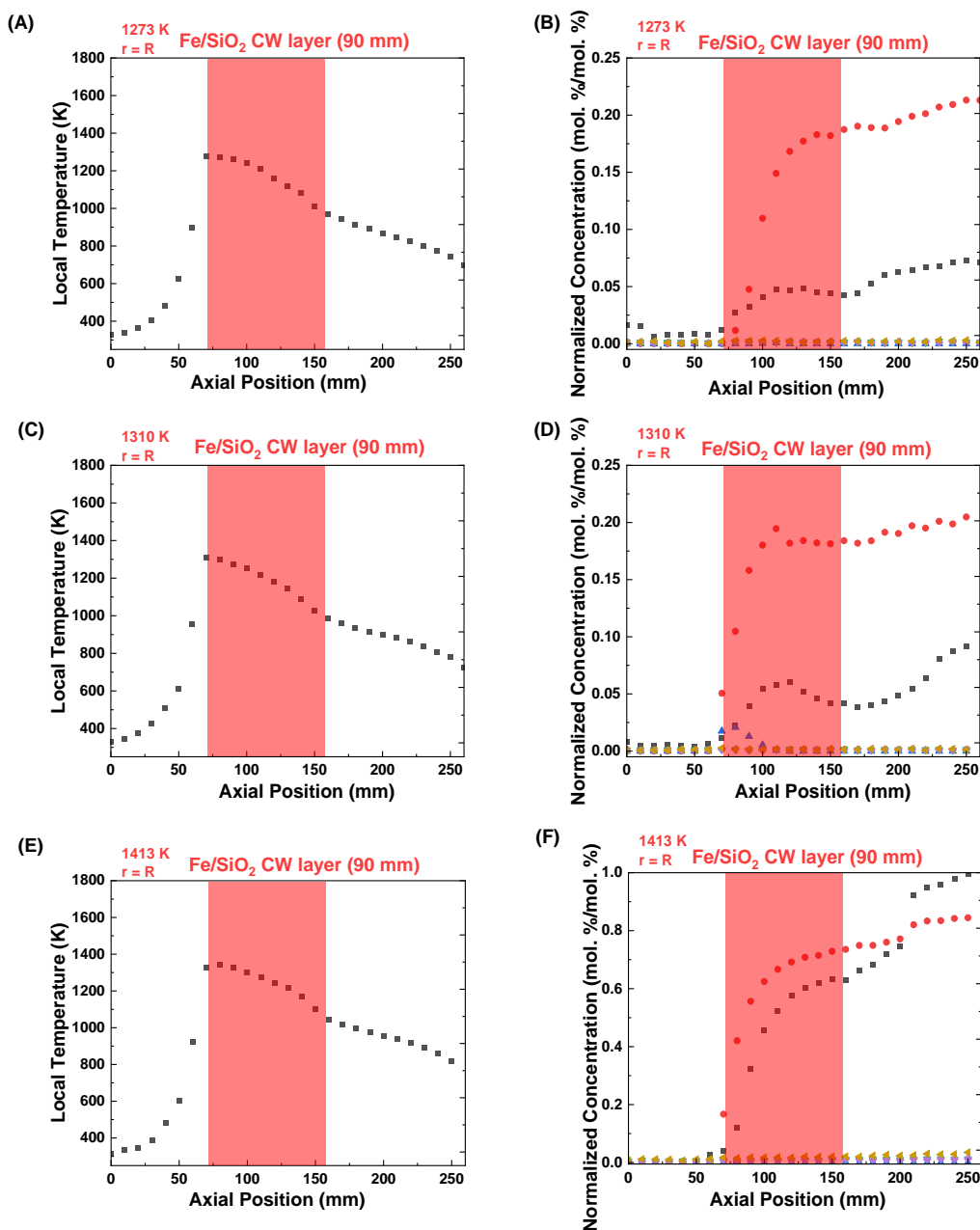


**Figure 4.2.** Autothermal Fe/SiO<sub>2</sub> catalytic wall reactor: (A)(C)(E) Axial temperature profiles at near the reactor inner wall with peak temperature at 1273 K, 1310 K and 1413 K. (B)(D)(F) Axial local concentration of nonoxidative methane conversion products: acetylene, ethylene, and ethane, respectively in autothermal catalytic wall reactor respect to (A), (C) and (E). (■ Acetylene; ● Ethylene; ▲ Ethane; ▼ Benzene; ◆ Toluene; ♣ Naphthalene)

A degree of C<sub>2</sub>H<sub>6</sub> formation is observed near the reactor wall as methane enters the catalytic wall zone (70 mm). However, C<sub>2</sub>H<sub>6</sub> quickly disappears once the effluent leaves the catalytic section. We theorize that this phenomenon results from a high local ethylene concentration that triggers an equilibrium response, thereby leading to the formation of transient specie, ethane, through ethylene hydrogenation. Nevertheless, as the product species diffuse in the radial direction, the reaction equilibrium at 1198 K continues to favor ethylene dehydrogenation, contributing to the reversible nature of C<sub>2</sub> chemistry and complete dehydrogenation of ethane. The axial C<sub>2</sub>H<sub>6</sub> concentration profile, resembling a volcano shape near the reactor wall, results from a reduced rate of catalytic surface reaction to generate C<sub>2</sub>H<sub>4</sub> due to the decreasing temperature in the axial direction (200-300 mm).

Hilal Ezgi Toraman and colleagues have previously reported a comprehensive density functional theory (DFT) model of non-oxidative methane conversion over Fe/SiO<sub>2</sub><sup>130</sup>. According to their model, under reaction conditions, iron atoms form isolated carbides that activate ethylene formation on the catalyst surface. This ethylene is then consumed by a gas-phase dehydrogenation reaction to form acetylene and aromatics. Our experimental results provide direct experimental evidence validating these model predictions.

#### 4.3.2 Spatially resolved autothermal catalytic wall reactor analysis

The SpaciMS analysis method was also applied to the autothermal catalytic wall reactor for NMC reaction with diluted methane gas flow rate (CH<sub>4</sub>:Ar = 1:4, 14 mL min<sup>-1</sup>) The purpose of this application was to examine the interaction between surface and gas phase reactions during methane conversion over a Fe/SiO<sub>2</sub> catalyst at different

heating profiles controlled via methane combustion flow rates. Figure 4.3 demonstrates the spatially resolved temperature and gas concentration results for the autothermal catalytic wall reactor.

In comparison to the conventional heated catalytic wall reactors, the axial production concentration profiles of autothermal catalytic wall reactors exhibited a significant difference. No substantial number of products was observed before the reactor's catalytic zone, indicating that the autothermal catalytic wall reactor could suppress the formation of undesired gas-phase reactions. This is achieved by providing a rapid heating solution, enabling the on-demand catalytic formation of ethylene. Based on the NMC flow rate, the average heat rate of the autothermal catalytic wall reactor is  $226 \text{ K sec}^{-1}$ . Conversely, under a conventional furnace, the methane feed flow is heated at a rate of  $36 \text{ K sec}^{-1}$ . This slower heating rate leads to the gas-phase conversion of methane to acetylene and aromatics before entering the catalytic zone, increasing the risk of coke formation on the catalyst surface due to prolonged exposure to high-temperature gas-phase reactions.

Further investigations into temperature and product concentration profiles led to the discovery of a higher ethylene selectivity (>50%) within the catalytic zone of the autothermal catalytic wall reactor. This observation signifies the suppression of gas-phase reactions in the autothermal catalytic wall reactor. Despite a rapid decrease in the axial temperature profile after reaching the peak temperature, the concentration of ethylene and acetylene increased rapidly near the entrance of the catalytic zone and then declined linearly before exiting the catalytic wall zone.

These concentration profiles can be explained by the promoted Fe/SiO<sub>2</sub> surface reaction near the peak temperature, forming ethylene at the catalytic reactor wall. As the temperature starts to decline, the ethylene formation rate decreases, and secondary gas-phase reactions continue to form vinyl, ethyl, and acetylene from ethylene, leading to a decrease in ethylene concentration.

The acetylene concentration increased and decreased in concert with ethylene along the axial direction. Despite gas-phase reactions being suppressed in an autothermal catalytic wall reactor, an increase in reaction temperature still promotes the gas-phase ethylene dehydrogenation reaction. Moreover, the decrease in acetylene concentration near the exit of the catalytic wall zone is likely caused by the secondary gas-phase reaction of acetylene with the methyl radical, forming allyl radicals and leading to a series of C<sub>3</sub> hydrogenation/dehydrogenation equilibrium chemistries.

The autothermal catalytic wall reactor limited secondary gas-phase reactions as the gas effluent left the catalytic zone (160 mm to 260 mm). In this reactor region, the temperature profile played a critical role in the formation of acetylene and ethylene. The ethylene and acetylene concentrations continued to increase as the temperature declined from 968°C to 697°C at an average rate of -2.7 K/mm (Figure 4.2A); 987°C to 726°C at an average rate of -2.6 K/mm (Figure 4.2C); and 1045°C to 819.25°C at an average rate of -2.5 K/mm (Figure 4.2E). In comparison to the isothermal heating technique, the autothermal catalytic wall reactor offers a unique non-uniform temperature profile. This enables rapid catalytic coupling of methane and limited gas-phase reactions, thus preventing the formation of heavy aromatics without compromising the ethylene yield.

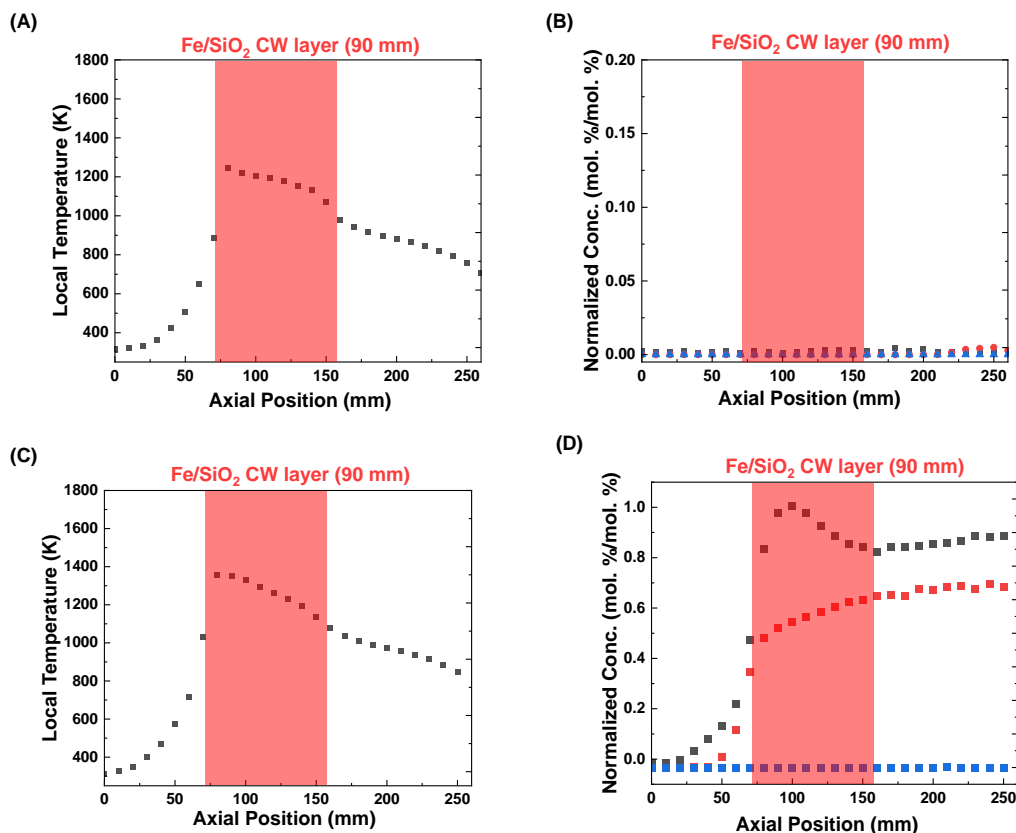


**Figure 4.3.** (A)(C) axial temperature profiles of pre-coked autothermal catalytic wall reactor with peak temperature at 1248 K and 1355 K. (B)(D) Axial local concentration of nonoxidative methane conversion products: acetylene, ethylene, and ethane, respectively in autothermal catalytic wall reactor respect to (A) and (C) (■ Acetylene; ● Ethylene; ▲ Ethane)

For a more comprehensive understanding of the influence of the gas-phase reaction on the NMC reaction, an autothermal catalytic wall reactor was pre-coated on the Fe/SiO<sub>2</sub> layer with methane above 1100°C for 10 hours before operation. In Figure 4.3, methane combustion flow rates of 2.5 L min<sup>-1</sup> and 2.8 L min<sup>-1</sup> were used to obtain axial temperature profiles with peak temperatures of 1248 K and 1355 K, respectively (Figure 4.3a and 4.3c).

Under these conditions, we found that when the peak temperature was at 1248 K, no product formed, indicating that methane decomposition is unlikely below this

temperature (Figure 4.3b). However, when the peak temperature was increased to 1355 K, rapid gas-phase activation of methane resulted in the formation of ethylene as an intermediate species and acetylene as the primary product (Figure 4.3d). Similar to the earlier autothermal catalytic wall reactor result with active Fe sites (Figure 4.2), the rapid increase and decrease of acetylene concentration profile underwent rapid dehydrogenation due to the sharp increase in temperature, followed by a temperature drop favoring the hydrogenation reaction.

It is worth noting that ethylene is a transient product for the gas-phase methane coupling reaction. To increase the ethylene yield, the gas-phase reaction should be well-controlled under a well-defined temperature that favors the acetylene hydrogenation reaction but suppresses the reverse dehydrogenation reaction of  $C_2H_4$ . From the species concentration profiles of the pre-cooked autothermal catalytic wall reactor, we can infer that the active autothermal catalytic wall reactor was dominated by the catalytic formation of ethylene on Fe active sites, as opposed to gas-phase reactions in the catalytic wall zone.

#### 4.4 Conclusion of chapter 4

In summary, the data affirms that the autothermal catalytic wall reactor represents a promising advancement in the efficient conversion of methane to ethylene. By harnessing its ability to rapidly adjust the temperature profile and suppress gas-phase reactions, this reactor can not only promote the desired catalytic reactions but also mitigate the risk of detrimental coke formation. The identification of higher ethylene concentration near reactor wall has demonstrated experimental evidence of Fe/SiO<sub>2</sub> catalyst surface product, ethylene. The higher local concentration and volcanic

concentration profile of ethylene in the ACWR presented the effectiveness of ACWR in comparison with conventional reactors. Therefore, the exploration and optimization of such technology could serve as a significant steppingstone towards the development of more efficient, sustainable, and economically viable industrial-scale applications.

## Chapter 5: Programmable heating and quenching for efficient methane pyrolysis

(Work reproduced from Qi Dong\*, Yonggang Yao\*, Sichao Cheng\*; Konstantinos Alexopoulos\*, Jinlong Gao, Sanjana Srinivas, Yifan Wang, Yong Pei, Chaolun Zheng, Alexandra H. Brozena, Hao Zhao, Xizheng Wang, Hilal Ezgi Toraman, Bao Yang, Ioannis G. Kevrekidis, Yiguang Ju, Dionisios G. Vlachos, Dongxia Liu & Liangbing Hu. Programmable Heating and Quenching for Efficient Thermochemical Synthesis, *Nature*, 2022, 605, 470–476. doi: 10.1038/s41586-022-04568-6.)

Acknowledgement: The work presented here is from the main efforts of Sichao Cheng to initiate the PHQ of methane pyrolysis reactor design and testing with Dr. Qi Dong. The first-principle-based reactor simulation was mainly contributed by Dr. Konstantinos Alexopoulos.

### *5.1 Introduction*

Thermochemical reactions proceed along specific pathways that are heavily affected by the reaction temperature and time. In particular, the elementary reaction rate is exponentially dependent on temperature according to the Arrhenius law, and the product distribution can be further influenced by establishing or shifting the chemical equilibrium<sup>145,146</sup>. Therefore, dynamic modulation of the heating profile could be used to control the reaction pathways for targeted product yield and selectivity. However, conventional thermochemical reactions are typically conducted by continuous heating under near-equilibrium conditions<sup>145</sup>, despite a long history of efforts to develop dynamically heated reactors<sup>147-149</sup>. This is in part because conventional heating devices show poor heat transfer and large thermal inertia, which makes it challenging to attain temporal control over the temperature profiles and thus affect the reaction pathways. Taking methane pyrolysis as an example, selective methane transformation to value-added products has proved extremely important but difficult to achieve under continuous heating at a relatively mild temperature regime (<1,400 K)<sup>48</sup>. The

constraints of chemical equilibrium often result in limited selectivity, low conversion, or both.

In chapter 5, we report a dynamic operating technique that addresses these issues using programmable heating and quenching (PHQ) to conduct thermochemical reactions with a high selectivity, rate and yield to value-added products at low energy cost. Compared with conventional steady-state approaches that operate with continuous heating at constant temperatures (for example, 1,273 K in Figure 1a), the Joule-heating-based PHQ method allows for rapid switching between low and high temperatures (for example, between 650 and 2,000 K in Figure 5.1b) in just milliseconds, simply by varying the electric current applied to a carbon heater to achieve thermochemical synthesis. Such a heating profile is also enabled by placing the porous carbon heater in direct contact with the reactants to establish efficient heat transfer. This design allows the temperature of the gas-phase reactants and the adsorbed surface species on the catalysts to closely follow the temperature profile of the carbon heater, which enables us to precisely control the reaction pathway under non-equilibrium conditions.

Using methane pyrolysis as a model reaction, our PHQ method demonstrates much higher selectivity (>75% versus <35%) to value-added C<sub>2</sub> products at comparable methane conversions (about 13%) in comparison with the conventional catalyst-free methane pyrolysis performed under near-equilibrium conditions by continuous heating<sup>2</sup> (Figure 5.1c). The C<sub>2</sub> product selectivity by our metal-catalyst-free PHQ technique even outperforms most literature reports of methane pyrolysis using optimized catalysts by continuous heating<sup>3-10</sup> (Figure 5.1d). The PHQ technique can also be expanded to a variety of thermochemical processes, such as NH<sub>3</sub> synthesis, to

achieve high production rates and good stability. This approach establishes a general platform for efficient thermochemical synthesis with a high reaction rate, selectivity, reduced energy cost and improved catalyst stability.

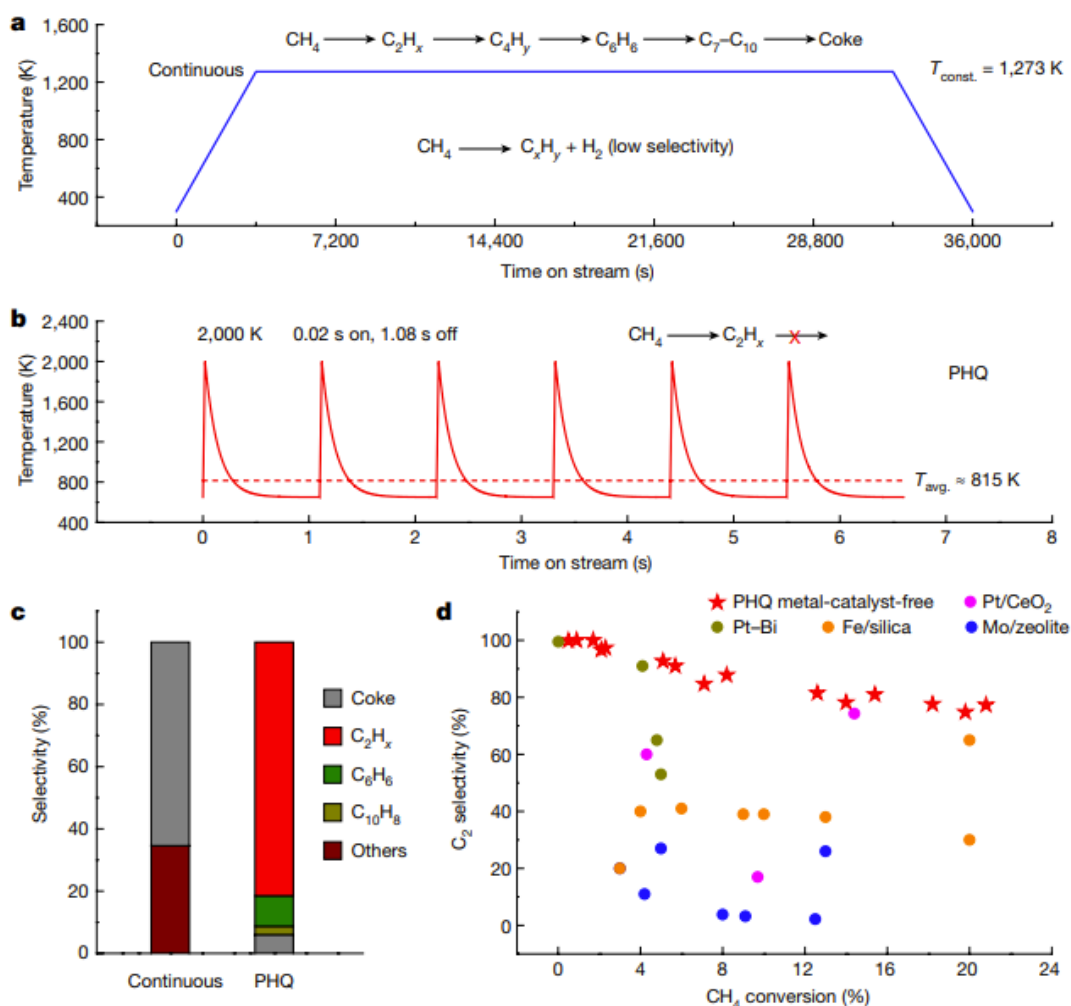


**Figure 5.1.** Comparison between our PHQ method and conventional continuous heating using a  $\text{CH}_4$  pyrolysis model reaction. a, Schematic of a typical temperature profile by continuous heating. Continuous heating creates a variety of products owing to the lack of temporal tunability over the temperature profile and thus the resulting

reaction pathways. b, Schematic of an estimated temperature profile by the PHQ method. PHQ selectively produces value-added C<sub>2</sub> products. The high temperature ensures high conversion, whereas the transient heating duration enables high selectivity. c, Comparison of CH<sub>4</sub> pyrolysis by PHQ in this work and continuous heating reported in the literature<sup>2</sup>. At comparable CH<sub>4</sub> conversions (about 13%), continuous heating of the non-catalytic CH<sub>4</sub> pyrolysis reaction results in coke as the major product (grey) with other minor products (maroon)<sup>8</sup>, whereas CH<sub>4</sub> pyrolysis by PHQ showcases its >75% selectivity to C<sub>2</sub> products (red). d, Our metal-catalyst-free PHQ technique (red stars) even outperforms most literature reports of CH<sub>4</sub> pyrolysis reactions with optimized catalysts conducted by continuous heating in terms of the C<sub>2</sub> product selectivity at a wide range of CH<sub>4</sub> conversions<sup>3-10</sup>.

## 5.2 Experiments preparation and test procedure

### 5.2.1 Materials and instruments

Carbon paper (Freudenberg H23 gas diffusion layer) and carbon felt (AvCarb G475A) were obtained from Fuel Cell Store. Carbon felt (ACF 1000) was obtained from Fuel Cell Earth. The ACF 1000 carbon felt was used to study the morphological evolution of the catalyst. The AvCarb G475A carbon felt was found to be more stable against the rapid temperature change by programmable heating and quenching (PHQ), while the ACF 1000 carbon felt may break during long-term PHQ operations. Ruthenium (Ru) chloride hydrate, iron (Fe) chloride, hydrochloric acid, sodium hydroxide, sodium citrate, sodium hypochlorite, salicylic acid, sodium nitroferricyanide, and ammonium chloride of at least reagent grade were purchased from Sigma Aldrich. The carbon felt was loaded with Ru (2 wt%) or Fe catalyst (2 wt%) using a method described in our previous work<sup>150</sup>. All carbon materials were rinsed with ethanol and acetone, followed by overnight vacuum drying prior to installation in the heating device. The carbon materials were additionally preheated in Ar atmosphere for 2 h before each test due to the high surface area to remove moisture. Mirrorlike multipurpose 110 copper wire (99.9%, 0.04" diameter) and multipurpose

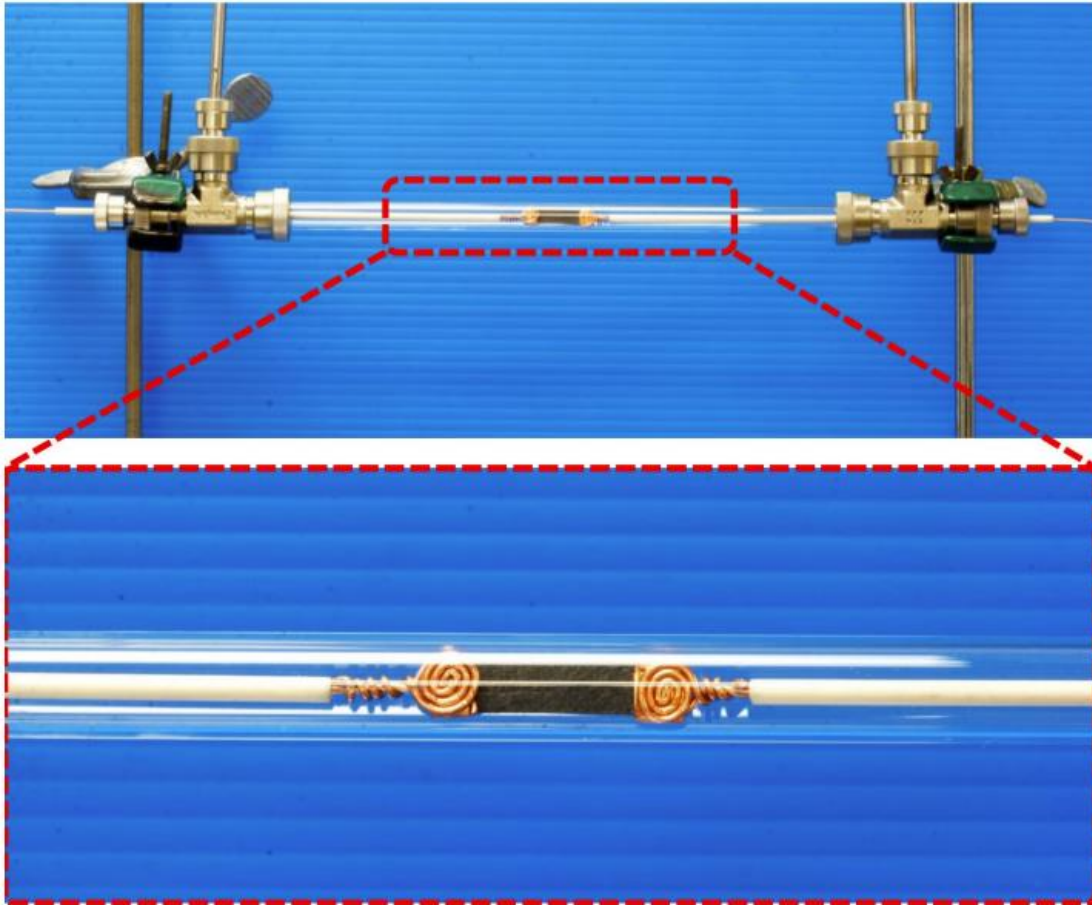
110 copper sheets (99.9%, 0.002" thickness) were obtained from McMaster Carr. The copper materials were cleaned by acetone and dried under vacuum prior to installation in the heating device. Alumina ceramic protection tubes (99.8%, 0.125" outer diameter and 0.062" inner diameter, maximum temperature 2,223 K) were obtained from Omega and used without further cleaning. A solid-state relay device with DC input and DC output (maximum current 25 A) was obtained from Omega. The input signal to the solid-state relay was provided by a sourcemeter (Keithley, Model 2425). The output signal was provided by a power source (Volteq, 75 V, 20 A).

### 5.2.2 *Reactor setup*

The dimensions of the carbon paper used for the methane pyrolysis reaction were 40 mm × 8 mm in size, with 20 mm × 8 mm exposed during the PHQ operations, with the remaining distance at each end being wrapped with copper foil. The dimensions of the carbon felt used in the NH<sub>3</sub> synthesis were 35 mm × 8 mm in size, with 15 mm × 8 mm exposed during the PHQ operations, with the remaining distance at each end being wrapped with copper foil. The lengths of the carbon paper shown in the digital images (but not for testing the reaction products) were increased for better demonstration. The wrapped region was further connected with copper wire to secure the electrical connection. No additional conductive glue or paste was needed to improve the electrical contact. The copper wire was then inserted through the alumina ceramic protection tube and connected with the power supply. Each end of the alumina ceramic protection tube was sealed with epoxy (Gorilla) (T < 373 K). The carbon heating element, copper material, and alumina ceramic protection tubes were placed in a quartz tube reactor (1/2"), which was connected with Swagelok Ultra-Torr tee fittings on each

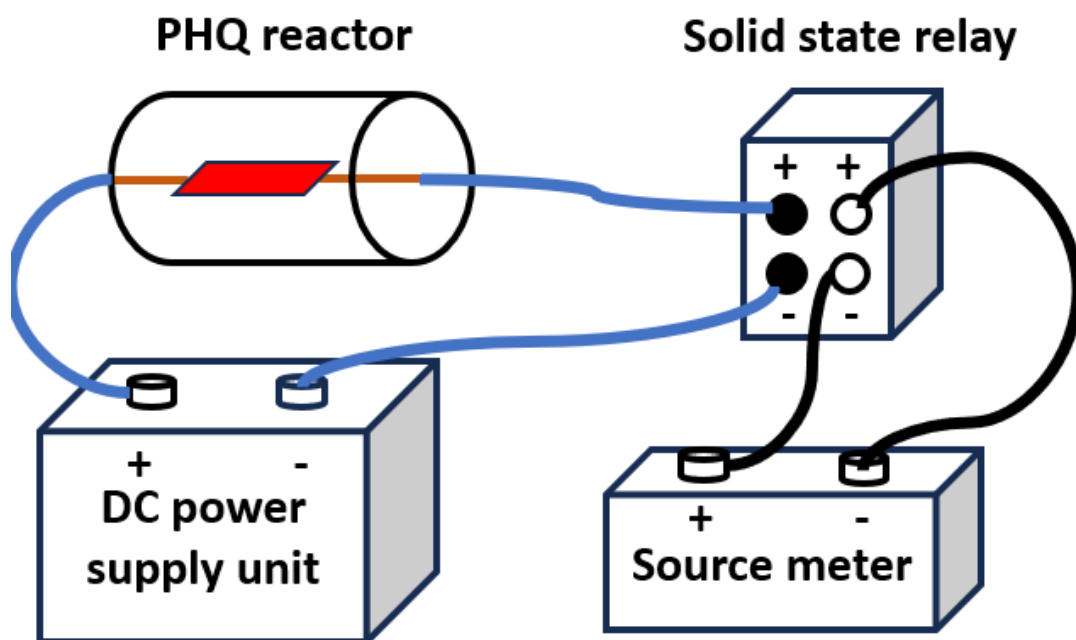
end. One port of the tee fitting was used for the electrical connection while the other was used for the gas inlet or outlet. A thermocouple was attached to the quartz tube close to the carbon material to monitor the temperature of the quartz tube during PHQ operations. The measured temperature was used to establish boundary conditions in the modeling efforts. Continuous heating for methane pyrolysis was conducted using a tube furnace.

The PHQ reactor can be simply modified from a conventional flow reactor setup (Schematic 4.1). The carbon heater is placed in a quartz tube (1/2" outer diameter) and connected to a power source via copper wires that are protected by alumina ceramic tubes. At both ends of the reactor, we attach Swagelok Ultra-Torr tee fittings, in which one port of each tee is used for the electrical connection, and the other is used for the gas inlet or outlet.



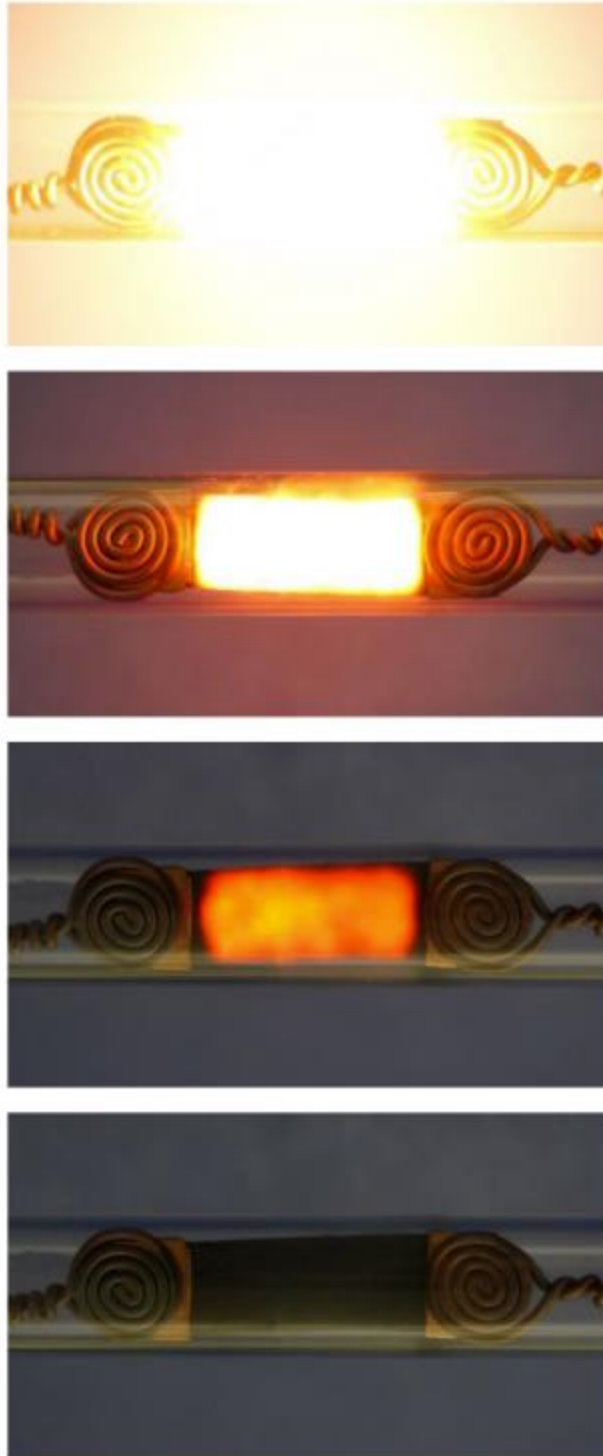
**Schematic 4.1.** Digital images of the PHQ reactor.

The schematic drawing of the electrical circuit is shown in Schematic 4.2. The input signal is passed from the sourcemeter to the solid-state relay device, which provides the ability to program the on/off switching. The output signal of the solid-state relay is applied to the power source and the reactor, which are connected in series. The pulse peak temperature ( $T_{\text{high}}$ ) is controlled by the electrical power of the power source, while the pulse duration is controlled by the “on” duration of the sourcemeter.



**Schematic 4.2.** Schematic drawing of the electrical circuit.

An electric current is applied through the carbon paper to generate heat. We are able to achieve ramping and cooling rates of  $\sim 10^4$  K/s owing to the low heat capacity of the carbon paper heater. Notably, Joule heating of the carbon paper heater can allow us to reach  $\sim 2,400$  K in milliseconds. After turning off the power, the heater quickly cools down to  $\sim 800$  K within  $\sim 1$ s (Schematic 4.3).



**Schematic 4.3.** Four selected frames from a recorded video during the cooling process of the carbon paper heater.

### 5.2.3 Product detection for methane pyrolysis

The outlet product stream from the reactor was connected to and examined by gas chromatography (GC, Agilent 6890N) equipped with a DB-Wax column connected to a flame ionization detector as well as a ShinCarbon ST packed column connected to a thermal conductivity detector. A mixture of Ar and methane was fed into the reactor, where Ar was used as an internal standard and balance gas. The percent conversion of CH<sub>4</sub> ( $X_{CH_4}$ ) was calculated according to Equation 4.1, where  $A_{i,in}$  ( $i = CH_4$  or Ar), which is the integrated peak area from the GC analysis, was determined from at least two initial GC calibration injections before the PHQ operation for each run.

$$X_{CH_4} = \frac{\left(\frac{A_{CH_4,in}}{A_{Ar,in}}\right) - \left(\frac{A_{CH_4,out}}{A_{Ar,out}}\right)}{\left(\frac{A_{CH_4,in}}{A_{Ar,in}}\right)} \quad 4.1$$

After the installation, the reactor was purged with 30 standard cubic centimeters per minute (sccm) Ar for 1 h, followed by feeding a mixed stream of CH<sub>4</sub> and Ar into the reactor for another 1 h until reaching a steady-state. Each data point was collected after running the reaction for ~26 mins. Product formation rates ( $\dot{n}_{product}$ ) were calculated from the response factor according to Equation 4.2, where RF represents the response factor of each product with respect to Ar from the GC analysis, A is the integrated peak area from the GC analysis, and  $i \geq 1$  (including CH<sub>4</sub>).

$$\dot{n}_{C_iH_j} [mmol/min] = \frac{A_{C_iH_j}}{A_{Ar}} \times \dot{n}_{Ar,in} \times RF_{C_iH_j/Ar} \quad 4.2$$

The coke formation rate ( $\dot{n}_{coke}$ ) was calculated according to Equation 4.3 based on the initial CH<sub>4</sub> feed flow rate, where  $i \geq 1$  (including  $\dot{n}_{CH_4,out}$ ).

$$\dot{n}_{coke} [mmol/min] = \dot{n}_{CH_4,in} - \sum (\dot{n}_{C_iH_j} \times i) \quad 4.3$$

The selectivity of CH<sub>4</sub> to each gaseous product (S) was calculated according to Equation 4.4, where  $i \geq 2$  (not including CH<sub>4</sub>).

$$S_{product} [mol\ \%] = \left( \frac{\dot{n}_{C_iH_j} \times i}{\sum (\dot{n}_{C_iH_j} \times i) + \dot{n}_{coke}} \right) \quad 4.4$$

The selectivity of CH<sub>4</sub> to coke products ( $S_{coke}$ ) was calculated according to Equation 4.5, where  $i \geq 2$  (not including CH<sub>4</sub>). Note the unaccounted species  $\dot{n}_{coke}$  include actual coke and other products with large molecular weights, which we considered to be coke-like species.

$$S_{coke} [mol\ \%] = \left( \frac{\dot{n}_{coke}}{\sum (\dot{n}_{C_iH_j} \times i) + \dot{n}_{coke}} \right) \quad 4.5$$

All reactions were conducted under ambient pressure (1 atm). The inlet gas temperature was 298 K in all cases. A flow rate of 24 sccm (90 mol% CH<sub>4</sub>, 10 mol% Ar) was used for comparing continuous heating and PHQ methods (Figure 5.3a). A flow rate of 4 sccm (75 mol% CH<sub>4</sub>, 25 mol% Ar) was used for detailed studies on  $T_{high}$  and the pulse duration (Figure 5.3b–d, with one data point from Figure 5.3c being used in Figure 5.1c for comparing PHQ and continuous heating, due to their comparable conversions). With a lower flow rate of 4 sccm, the conversion was relatively high so that the influences by  $T_{high}$  and the pulse duration could be better unveiled.

Note that the temperature of the electric circuit components (e.g., Cu wires) remained lower than  $T_{avg.}$  during PHQ operations due to their low electrical resistivity (therefore low heat generation during Joule heating), large heat capacity, and high thermal conductivity. A control experiment showed ~0% CH<sub>4</sub> conversion in the

presence of the electric circuit components (e.g., Cu wires) under continuous heating by a furnace at 900 K ( $> T_{avg}$ ), ruling out potential artifacts in the PHQ process.

#### 5.2.4 *Temperature acquisition*

The temperature evolution of the carbon-based heating element was measured using a Vision Research Phantom Miro M110 high-speed camera based on color ratio pyrometry, with videos recorded at 1000 frames/s. The temperature was calculated by applying the gray-body assumption substituted in Planck's Law and integrating over the entire spectrum where the camera is sensitive (i.e., 400–1,100 nm; shown in Equation 4.6)<sup>151</sup>.

$$\frac{I_i}{I_j} = \frac{\psi_i \int L(\varepsilon, \lambda, T) \chi_i(\lambda) d\lambda}{\psi_j \int L(\varepsilon, \lambda, T) \chi_j(\lambda) d\lambda} \quad 4.6$$

in which  $I_i$  is the intensity of a color channel (i.e., red, green or blue),  $\psi_i$  is the channel gain,  $\varepsilon$  is the emissivity, and  $\chi_i$  is the spectral response. Calibration was achieved by a Newport Oriel 67000 Series Blackbody Infrared Light Source and calibration factors  $C_{gr}$  (green/red),  $C_{bg}$  (blue/green), and  $C_{br}$  (blue/red) can be obtained by comparing the measured values to the theoretical ones, as shown in Equation 4.7<sup>151</sup>.

$$\frac{I_i}{I_j} = C_{ij} \left( \frac{I_i}{I_j} \right)_{\emptyset} \quad 4.7$$

At each pixel, to recover values for the red, green, and blue channels, the demosaicing routine in MATLAB was used with the camera's Bayer color filter array. Temperature estimates were made using color ratio pyrometry in which three color channels (red, green, and blue) were calculated and then matched to a gray-body calibration curve. The error in the reported temperature values is nominally ~100 K.

For the temperature profile, only unsaturated pixels above the black level and within the error threshold were included to report the mean and median temperature of the frame for a contiguous area of at least 10 acceptable pixels. The temperature of the carbon heater was calculated by fitting the emitted light spectra according to the gray body radiation and the following equation:

$$B_{\lambda}(\lambda, T) = \gamma \varepsilon_{gray} \frac{2hc^2}{\lambda^5} \frac{1}{e^{\frac{hc}{\lambda k_b T}} - 1} \quad 4.8$$

in which  $k_B$  is the Boltzmann constant,  $\lambda$  is the wavelength,  $h$  is Planck's constant,  $c$  is the speed of light, and  $\varepsilon_{gray}$  is the gray body emissivity. Scaling constant  $\gamma$  and temperature  $T$  are the fitting parameters for this equation.

As the color ratio pyrometry method has a lower detection limit of ~1,100 K, only a part of the temperature profile can be accurately captured. Therefore, we used a linear temperature ramp followed by exponential decay of temperature based on the measured  $T_{high}$ , initial cooling rate, and  $T_{low}$  (measured by a thermocouple) to estimate the temperature profiles shown in Figure 5.1b and Figure 5.2b, which schematically demonstrate the fast heating and cooling processes by the PHQ technique.

### 5.2.5 Spectroscopic and microscopic characterization

X-ray diffraction (XRD) was conducted using a PANalytical X'Pert Pro diffractometer with Cu K $\alpha$  radiation. Raman spectra were obtained with a micro-Raman system (XploRA, Horiba) equipped with a 532 nm laser. Scanning electron microscopy (SEM) images were taken using a JEOL 6340F microscope operated at a 10 kV accelerating voltage.

### 5.2.6 Modeling details for first-principles-based reactor simulations

Methane pyrolysis was modeled using an *ab initio* gas-phase reaction mechanism<sup>152</sup>. This gas-phase reaction mechanism involves 501 species and 9,286 reactions that belong to six main reaction families: (1) hydrogen atom abstraction; (2) dissociation/recombination; (3) isomerization; (4) addition/ $\beta$ -scission; (5) disproportionation; and (6) other reactions, such as Diels-Alder and retroDiels-Alder reactions. The full microkinetic model was solved in a continuous stirred tank reactor using an in-house Fortran code built around the Chemkin II chemical kinetics library of subroutines<sup>58</sup>. The experimental results shown in Figure 5.6c and 5.6d suggest that the methane conversion affects the selectivity to various species. For a fair comparison between the two operation modes of PHQ and continuous heating, both reactors adopted the same 5% methane conversion to ensure that the mechanistic study was carried out in the kinetically-controlled regime. A temperature ramp followed by exponential decay of temperature was applied on the reactor to simulate the PHQ process under transient conditions<sup>153</sup>, while the steady-state operation (continuous heating) of the reactor was simulated under isothermal conditions. In the case of PHQ, methane pyrolysis was assumed to occur during the temperature ramp. No further reaction occurs during cooling of the gas-phase mixture, which maintains its fixed composition obtained at the end of the temperature ramp (i.e., 5% methane conversion). The heat rates (Q) were calculated in the presence or absence of methane pyrolysis from the energy balance:

$$Q = \rho V_r C_p \frac{dT}{dt} + \dot{m}_{in}(H_{out} - H_{in}) \quad 4.13$$

where  $\rho$  is the density of the reaction mixture,  $V_r$  denotes the reactor volume,  $C_p$  is the heat capacity of the reaction mixture,  $\frac{dT}{dt}$  denotes the differential change of temperature over time (which is zero at steady-state isothermal conditions),  $\dot{m}_{in}$  is the total inlet mass flow rate,  $H_{out}$  is the total outlet enthalpy per unit mass, and  $H_{in}$  is the total inlet enthalpy per unit mass. It is worth noting that the energy balance equation is generally applicable to the entire reactor control volume, and the heat of reaction is embedded in the differences between the outlet and inlet enthalpies. Nevertheless, at the set methane conversion (i.e., 5%) the heat of the reaction does not add significantly to the overall heat required to operate the system. This finding also allows us to perform a more extensive analysis of the heating requirements with varying pulse duration, avoiding the need to include the reaction (i.e., by only using an inert gas flow).

### 5.3 Results and discussion

#### 5.3.1 PHQ technique for rapid heating and quenching

To apply the PHQ technique, we use a sheet of porous carbon paper as the heating element, which is placed along the middle axis of a quartz tube reactor (Figure 5.2a). To generate heat, we pass an electric current through the carbon paper, which — owing to its low heat capacity ( $<0.033 \text{ J K}^{-1}$ ) — is able to reach ramping and cooling rates of around  $104 \text{ K s}^{-1}$  (Figure 5.2b). During this process, the gas-phase reactants flow through the reactor and come into direct contact with the carbon paper, passing through and directly interacting with its microstructure (Figure 5.2c), thereby closely following its programmed heating pattern. Most of the electrical energy is converted to heat the gas molecules<sup>154</sup>, therefore the energy transfer efficiency by PHQ

is enhanced compared with conventional processes, in which heaters are generally placed outside the reactor<sup>68,155</sup>. Note that no extra catalyst is needed in the design (Figure 5.2c), as the high temperature of the carbon heater exponentially increases the methane activation rate for high conversion. For initial characterization of the PHQ method, we investigated the carbon paper heating element in a ‘flat’ configuration in the center of the reactor, which was straightforward to reproduce, although we acknowledge that this setup is not optimized for the spatial uniformity of temperature and methane conversion. However, the structural flexibility of the carbon heater provides the potential to manipulate its shape for enhanced interaction with the gas molecules (Figure 5.2d)

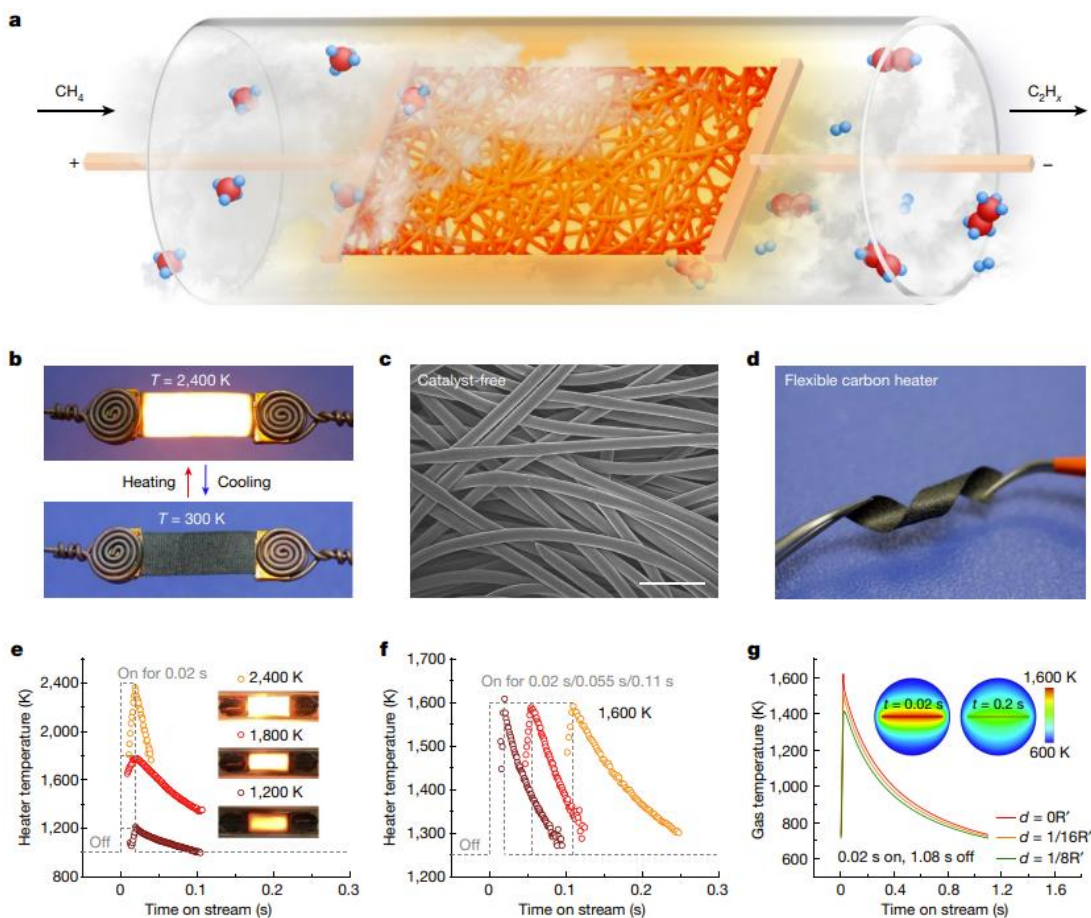


**Figure 5.2.** Operation of the PHQ technique. a, Schematic of the reactor design. The  $\text{CH}_4$  molecules pass through the reactor and interact with the heated porous carbon paper to rapidly transform into desirable value-added  $\text{C}_2$  products. b, Digital images of the carbon heater in power off (bottom) and power on (top) states, corresponding to the switch from room temperature (about 300 K) to high temperature (about 2,400 K). c, Scanning electron microscopy image of the carbon heater, showcasing the highly porous microstructure and the catalyst-free surface. Scale bar, 50  $\mu\text{m}$ . d, Digital image of the flexible carbon heater. e, The temporal temperature pattern of the carbon heater is tuned by increasing the input electrical power for higher peak temperatures at fixed pulse duration (dashed grey line). Insets are digital images showing the carbon paper being heated to different temperatures. f, The temporal temperature profile of the carbon heater can also be tuned by varying the pulse duration at a fixed peak temperature. Increased pulse duration requires decreased power input to reach the same peak temperature. g, Numerical simulation verifies that the temporal temperature pattern of the gas molecules closely follows that of the carbon heater (0.02 s on, 1.08 s off;  $T_{\text{high}} = 1,600$  K). The three traces represent the temporal temperature patterns of three spatial positions (in the reactor cross-section) vertically above the middle point on the upper surface of the carbon paper with distances ( $d$ ) of  $0R'$ ,  $1/16R'$  and  $1/8R'$ .  $R'$  is the closest distance from the middle point on the upper surface of the carbon heater to the edge of the cylindrical quartz tube reactor ( $R' = R - 1/2D$ , in which  $R$  is the radius

of the reactor and  $D$  is the thickness of the carbon paper). The insets show the cross-sectional contour maps of the gas temperature distribution when the time on stream equals 0.02 s (when  $T_{\text{high}}$  is reached) and 0.2 s (when most gas molecules are cooled down)

**Table 4.1.** Electrical parameters used for heating the carbon paper at various conditions.

<b>Pulse Duration (s)</b>	<b>Peak Temperature (K)</b>	<b>Applied Voltage (V)</b>
0.02	1200	~55
0.02	1400	58~61
0.02	1600	61~64
0.02	1800	64~67
0.02	2000	67~72
0.055	1200	28~33
0.055	1400	33~35
0.055	1600	35~37
0.055	1800	~38
0.055	2000	38~40
0.11	1200	~26
0.11	1400	26~28
0.11	1600	28~30
0.11	1800	~30
0.11	2000	30~33
0.33	1200	~16
0.33	1400	16~18
0.33	1600	18~20
0.33	1800	20~22
0.33	2000	~24

In a typical heating program, we switch the electrical power applied to the carbon heater from the ‘off’ state to the ‘on’ state and hold for 0.02 s, followed by removing the power to turn the heater back off for 1.08 s to complete a period of 1.1 s, which is then repeated. By adjusting the input power for a specific pulse duration, the peak temperature ( $T_{\text{high}}$ ) of the carbon heater can also be accurately controlled.

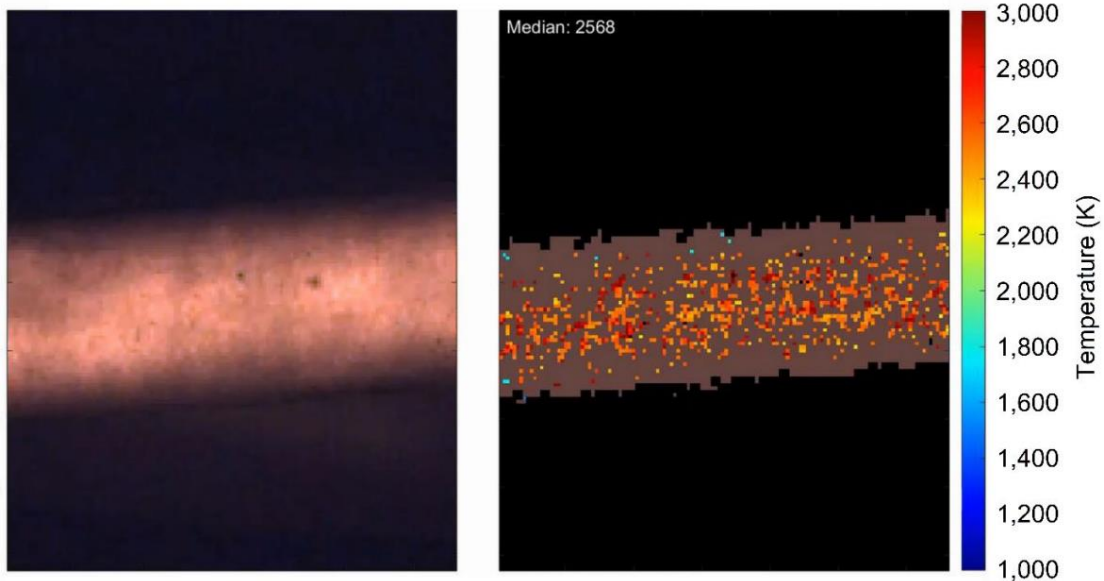


**Figure 5.3.** Peak temperature ( $T_{\text{high}}$ ) measurement using a high-speed camera.

An example of the peak temperature ( $T_{\text{high}}$ ) measurement is shown in Table 5.1 and Figure 5.3. The temperature distribution is captured using a high-speed camera. We convert the color image (on the left) of the carbon heater to a temperature map (on the right) to extract the average temperature ( $\sim 2,500$  K) throughout the material. The slight temperature variation at different positions of the carbon paper heater is due to the presence of pores of the material. We demonstrate the ability to tune  $T_{\text{high}}$  and the pulse duration according to the programmed electrical signal, as shown in Figure 5.2e, f, respectively. Using numerical simulations with different peak temperatures, we verify that the temperature profile of the gas molecules that interact with or are near the surface of the carbon paper precisely coincides with that of the heater (Figure 5.2g, Figure 5.4 & 5.5), demonstrating rapid heating and cooling rates. These results confirm that our PHQ method enables an accurate, temporal temperature pattern experienced by the gas molecules flowing through the reactor and interacting with the carbon heater.

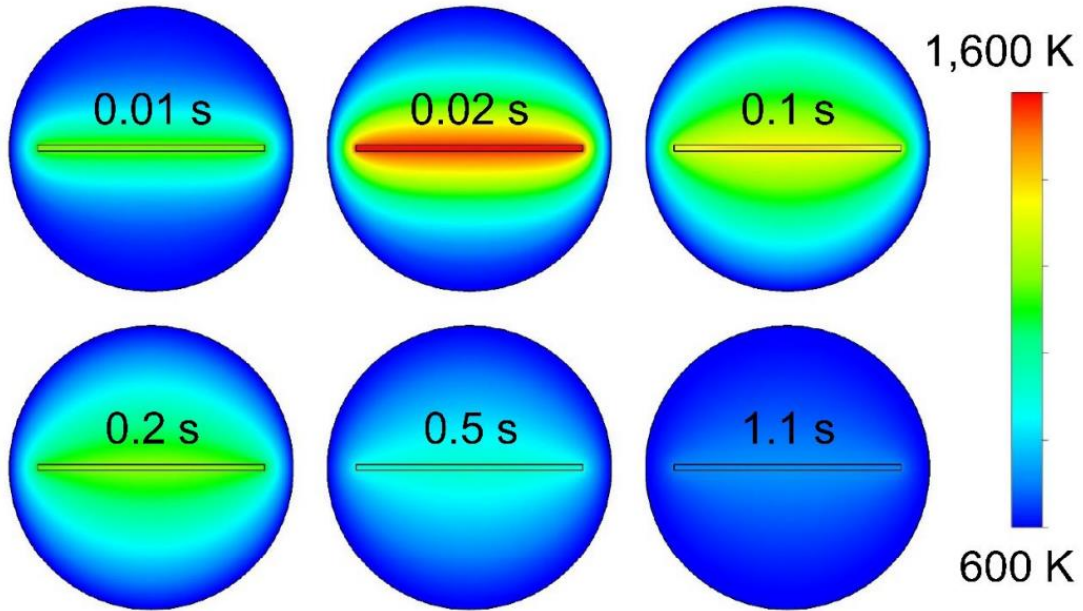


**Figure 5.4.** Cross-sectional contour images of the gas temperature distribution when the time on stream equals 0.01 s, 0.02 s, 0.1 s, 0.2 s, 0.5 s, and 1.1 s in a pulse period (0.02 s on, 1.08 s off;  $T_{\text{high}} = 1,600$  K). The temperature of the gas near the surface of the carbon paper (whose geometry is not optimized) follows closely to that of the heating element.

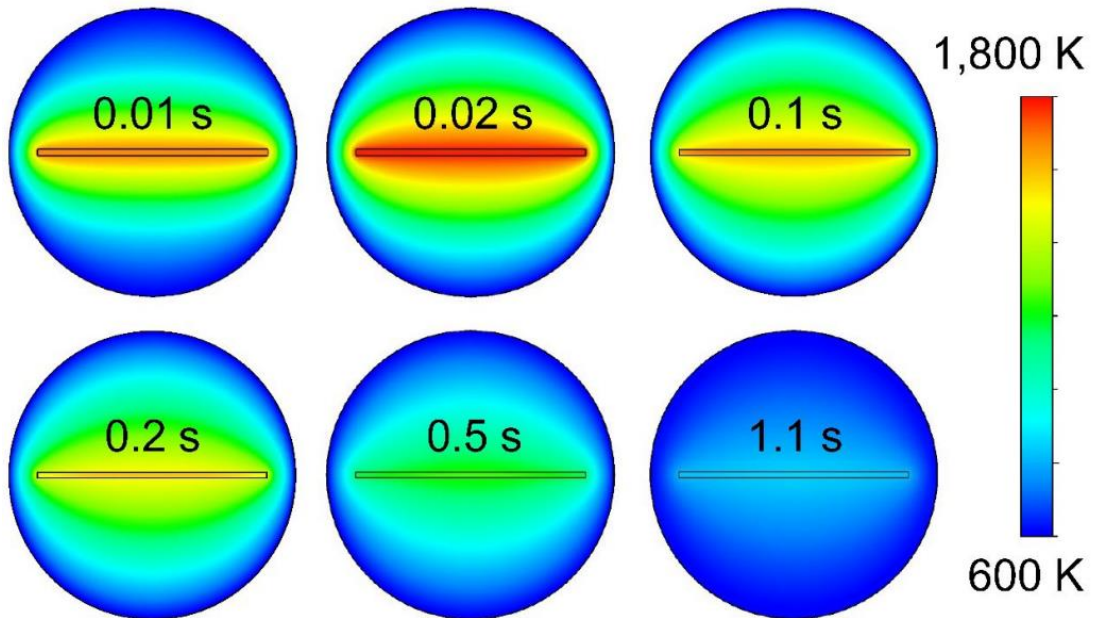


**Figure 5.5.** Cross-sectional contour images of the gas temperature distribution when the time on stream equals 0.01 s, 0.02 s, 0.1 s, 0.2 s, 0.5 s, and 1.1 s in a pulse period (0.02 s on, 1.08 s off;  $T_{\text{high}} = 1,800$  K). The temperature of the gas near the surface of the carbon paper (whose geometry is not optimized) follows closely to that of the heating element.

### 5.3.2 *PHQ technique for methane pyrolysis*

Figure 5.6 demonstrates the utility and advantages of our PHQ technique using methane pyrolysis as a model reaction. We compared four different reaction conditions (Figure 5.6a), including: (1) non-catalytic methane pyrolysis using continuous furnace heating at 1,273 K; (2) catalytic methane pyrolysis with a state-of-the-art Fe/silica catalyst<sup>3,4,48</sup> using continuous furnace heating at 1,273 K; (3) methane pyrolysis with the carbon paper heating element (as shown in Figure 5.2 but without PHQ) using continuous furnace heating at 1,273 K; and (4) methane pyrolysis using our PHQ technique with a  $T_{\text{high}}$  of 2,200 K and pulse duration of 0.055 s over a period of 1.1 s (0.055 s on, 1.045 s off). We found that the product distribution of our PHQ method showed a notable improvement compared with the other techniques, with a much higher selectivity (around 80%) for  $C_2$  products. In comparison, only about 40%  $C_2$  products were measured using continuous heating by a furnace at 1,273 K with the Fe/silica catalyst, which is consistent with the literature<sup>3</sup>. For the non-catalytic system, continuous furnace heating at 1,273 K produced nearly zero product. Meanwhile, continuous heating in the presence of the carbon paper (using a furnace, without PHQ) showed a large amount of undesired coke (about 30%) and low  $C_2$  product selectivity (about 40%)<sup>156,157</sup>(Figure 5.6a). These results indicate that low  $C_2$  selectivity is intrinsic to the continuous heating method owing to marked secondary and subsequent reactions, resulting in the formation of low-value compounds, such as naphthalene and coke.

By contrast, PHQ can achieve stable and high selectivity to  $C_2$  products with limited coke formation. In particular, the selectivity to coke remains low (< 5%). In this experiment, we used a  $T_{\text{high}}$  of ~2,000 K, a pulse duration of 0.055 s over a period of

1.1 s (0.055 s on, 1.045 s off), and a flow rate of 20 sccm (75 mol% CH<sub>4</sub>, 25 mol% Ar). The dimensions of the carbon paper used for this experiment were 40 mm × 8 mm in size, with 10 mm × 8 mm exposed during the PHQ operations, with the remaining distance at each end being wrapped with copper foil. Notably, with an average temperature ( $T_{\text{avg}}$ ) of <900 K, PHQ can obtain a comparable methane conversion (about 15%) and much higher value-added C<sub>2</sub> product selectivity than those by the Fe/silica catalyst using continuous heating at 1,273 K<sup>3,67</sup> (Figure 5.6a).

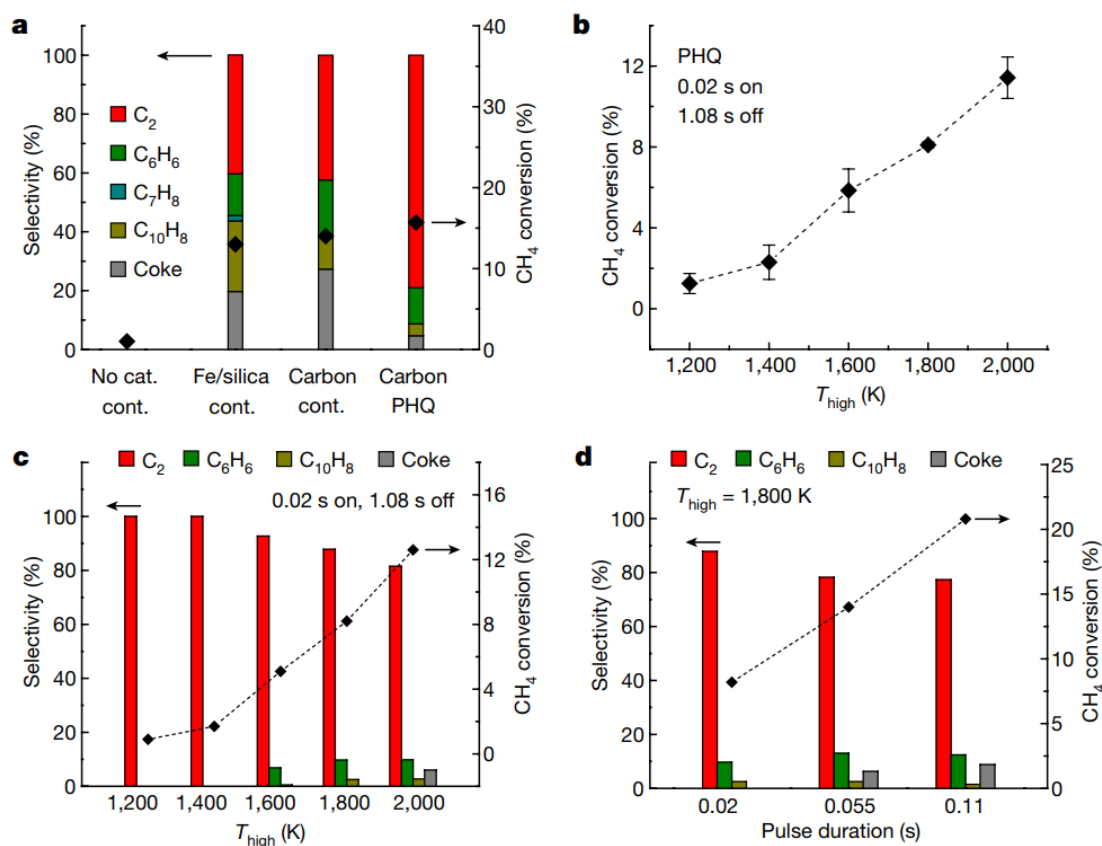


**Figure 5.6.** The utility and advantages of our PHQ technique. a, Comparison between (from left to right): (1) non-catalytic CH<sub>4</sub> pyrolysis using continuous furnace heating at 1,273 K; (2) catalytic CH<sub>4</sub> pyrolysis with a state-of-the-art Fe/silica catalyst using continuous furnace heating at 1,273 K; (3) CH<sub>4</sub> pyrolysis with carbon paper using continuous furnace heating at 1,273 K; (4) CH<sub>4</sub> pyrolysis using PHQ with a T<sub>high</sub> of 2,200 K and pulse duration of 0.055 s over a period of 1.1 s (0.055 s on, 1.045 s off,  $T_{\text{avg}}$  < 900 K). A flow rate of 24 sccm was used for all four reaction conditions. b,

CH<sub>4</sub> conversion increases with T<sub>high</sub> monotonically by PHQ, as demonstrated using a pulse duration of 0.02 s over a period of 1.1 s (0.02 s on, 1.08 s off). Error bars denote standard deviation with the value of n ≥ 3. c, Product selectivity by PHQ at various T<sub>high</sub> values with a fixed pulse duration of 0.02 s on and 1.08 s off. d, Product selectivity by PHQ using various pulse durations at a fixed T<sub>high</sub> of 1,800 K. A flow rate of 4 scem was used for b–d. The error range for C<sub>2</sub> product selectivity was found to be ±3%.

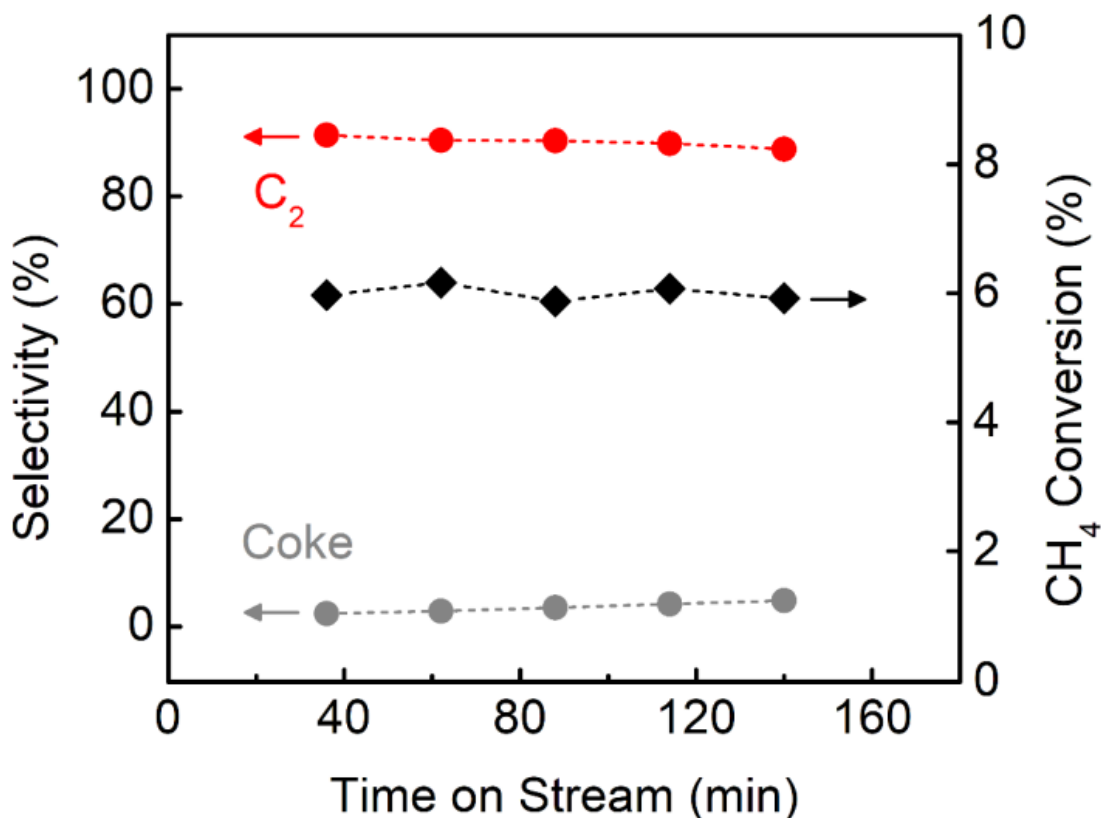


**Figure 5.7.** methane conversion and C<sub>2</sub> product selectivity by PHQ as a function of the time on stream.

We further explored the effect of T<sub>high</sub> and the pulse duration on the methane pyrolysis reaction by programming the electrical signal. Figure 5.8 schematically showcases the programmable control of the PHQ technique, which allows us to precisely tune the pulse peak temperature and pulse duration via the electrical signal applied to the carbon heater. Note that due to the gradual change of defect level and crystallinity of the carbon heaters (e.g., carbon paper and carbon felt) during PHQ

operations, the power input may need to be adjusted to maintain the desired peak temperature.

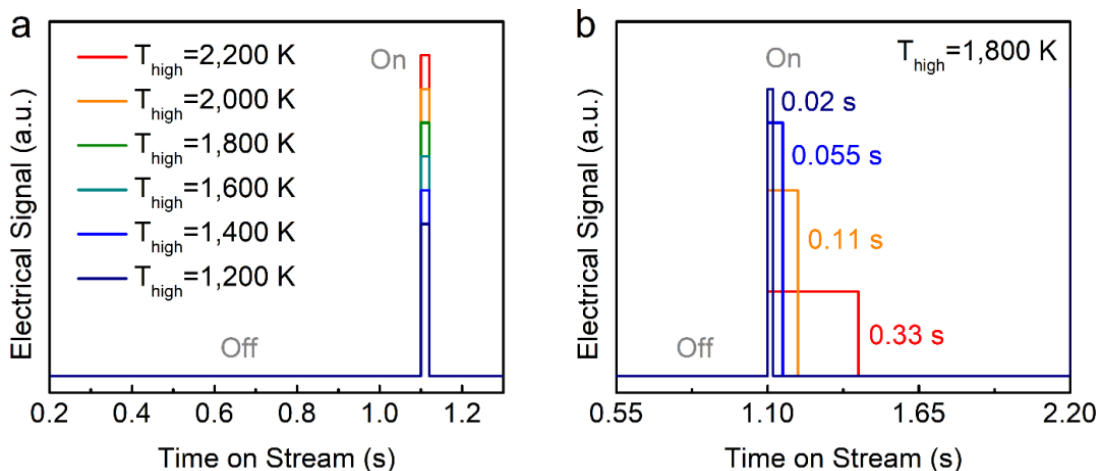


**Figure 5.8.** Programmable control by the PHQ technique. (a) Programmable control over the peak temperature from 1,200 K to 2,200 K by PHQ. (b) Programmable control over the pulse duration from 0.02 s to 0.33 s by PHQ.

In this experiment, we used a lower flow rate (4 sccm, 75 mol% CH<sub>4</sub> and 25 mol% Ar) to increase the methane conversion to better resolve these effects. With a fixed pulse duration of 0.02 s on and 1.08 s off, methane conversion increases with  $T_{\text{high}}$  monotonically (Figure 5.6b). Note that increased  $T_{\text{high}}$  at fixed pulse duration (0.02 s) leads to slightly lower selectivity to the C<sub>2</sub> products but higher selectivity to benzene (C<sub>6</sub>H<sub>6</sub>) owing to the increased reaction rate at higher temperatures (Figure 5.6c). Meanwhile, increasing the pulse duration at a constant  $T_{\text{high}}$  (1,800 K) leads to a similar trend owing to the longer reaction progress (Figure 5.6d). In general, the observed selectivity of the total C<sub>2</sub> products (for example, >75%) by the metal-catalyst-free PHQ process are among the best reported in the literature at comparable methane conversions<sup>3,5-10,158-160</sup>.

### 5.3.3 *Optimizing methane pyrolysis performance*

We suggest that the rapid heating and quenching processes of the PHQ synthesis provide a greater degree of control by matching the formation timescales of the intermediate  $C_2$  species in the methane pyrolysis reaction network but without allowing a steady state to be reached that would lead to secondary and subsequent products<sup>161</sup>. To investigate the mechanism behind the high  $C_2$  product selectivity of our technique, we used first-principles-based microkinetic simulations to compare the continuous heating and PHQ methods. We modelled two types of reactors operated at steady state (that is, under an isothermal condition) and transient modes (that is, using a rapid temperature ramp followed by an exponential decay) to simulate continuous heating and PHQ, respectively. In the steady-state continuous-heating mode, the simulated selectivity to  $C_6H_6$  species is notably high, indicating a large amount of secondary and subsequent reaction products. Compared with continuous heating, PHQ offers higher selectivity to  $C_2H_6$  and  $C_2H_4$  and lower selectivity to  $C_2H_2$  and  $C_6H_6$  (Figure 5.9). These results are in good agreement with our experimental observations in terms of the high  $C_2$  product selectivity. Beyond the enhanced  $C_2$  product selectivity, our calculations also show that PHQ potentially reduces the average energy needed by >80% compared with continuous heating at identical methane conversion. In Figure 5.10, our energy balance calculations show that PHQ reduces the average energy needed by > 80% compared to continuous heating at identical methane conversion, due to the use of a much lower average temperature. Figure 5.10 suggests that the heat required by the methane pyrolysis reaction is a small contribution to the total system energy needed at relatively low methane conversion (i.e., 5%). This result allows us to

perform further analysis with an inert gas (i.e., N<sub>2</sub>) as a feed to compare the energy efficiency of continuous heating and PHQ, which can be generalized for other reaction schemes. Thus, PHQ with pulse durations of less than 0.33s can largely reduce the required energy compared to continuous heating, potentially leading to better energy efficiency. This feature can be generalized for other reaction schemes, in which PHQ with pulse durations of less than 0.33 s could greatly reduce the energy cost compared with continuous heating.

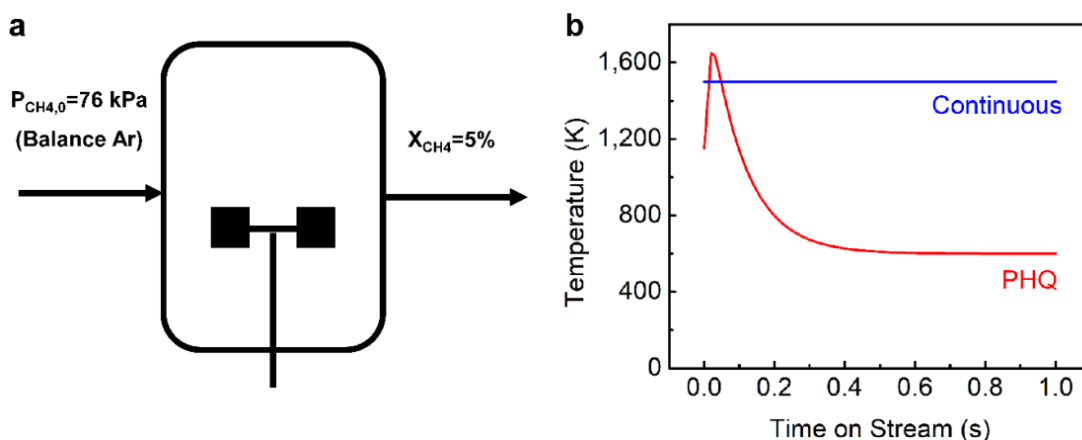


**Figure 5.9.** Modeling details. (a) The continuous stirred tank reactor setup used to model both the continuous heating and PHQ methods. (b) Temporal temperature profiles used for the steady-state and transient reactors, simulating conventional continuous heating and PHQ, respectively.

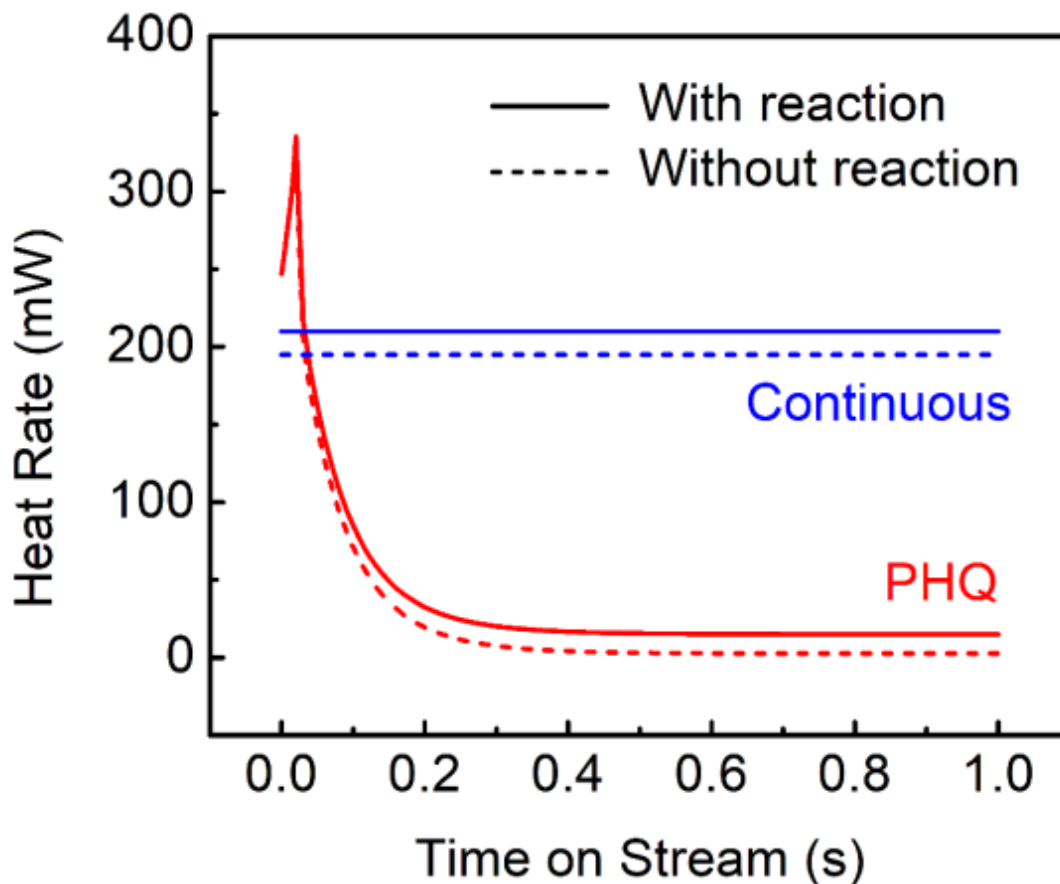


**Figure 5.10.** Heat rate profiles for the steady-state and transient reactors, simulating conventional continuous heating and our PHQ method, respectively. The heat of the reaction constitutes only a small portion of the overall heat required to operate the system at the set methane conversion of 5%.

#### 5.3.4 *First-principles-based reactor simulations for methane pyrolysis*

To understand the role of pulse duration by PHQ, we simulated the characteristic trajectories of methane conversion and product yields up to  $C_6H_6$  as a function of the astronomic time (that is, clock time or external time of the system)<sup>146,162</sup> under isothermal conditions ( $T = 1,500$  K). We employed first-principles-based microkinetic simulations to compare the continuous heating and PHQ methods for their product distribution and energy cost. Compared with continuous heating, PHQ offers higher selectivity to  $C_2H_6$  and  $C_2H_4$  and lower selectivity to  $C_2H_2$  and  $C_6H_6$  (Figure

5.11a). In addition, our calculations also show that PHQ reduces the average energy needed by > 80% compared to continuous heating at identical methane conversion (Figure 5.11b). Furthermore, through simulating the characteristic trajectories of methane conversion and product yields up to  $C_6H_6$  as a function of the astronomic time (Figure 5.11c), we found that the transient pulse durations by PHQ (e.g., 0.02 s and 0.055 s) can provide enough thermal energy to drive the methane pyrolysis reaction to  $C_2$  species but quench it before a large fraction of  $C_6H_6$  is produced as the reaction reaches steady-state.

We calculated the characteristic timescales (Figure 5.11d) and the reaction flux under PHQ and continuous heating conditions (Figure 5.11e) for each elementary step in the reaction path of methane pyrolysis toward aromatics formation. The results show that quenching of aromatics formation can be achieved by operating the pulse heating duration below the timescale for the cyclization reaction from  $C_3H_3\cdot$  (red, Figure 5.11d). In addition, the timescale for  $C_2H_2$  formation from  $C_2H_4$  is comparable to the pulse heating durations, which corroborates with the reduction in  $C_2H_2$  formation by PHQ (Figure 5.11a). Meanwhile, the timescales of the elementary steps towards  $C_2H_4$  formation are much smaller than the pulse duration, allowing the reaction to proceed towards  $C_2H_4$  by PHQ (Figure 5.11a). The calculated reaction flux under PHQ condition is distributed in reactions among  $C_2$  species (red), and the cyclization reaction from  $C_3H_3\cdot$  is insignificant. In contrast, under steady-state (continuous heating) condition, the reaction flux is more uniformly distributed among all the simulated elementary steps of methane pyrolysis, allowing the recombination of  $C_3H_3\cdot$  to form aromatic species (blue, Figure 5.11e).

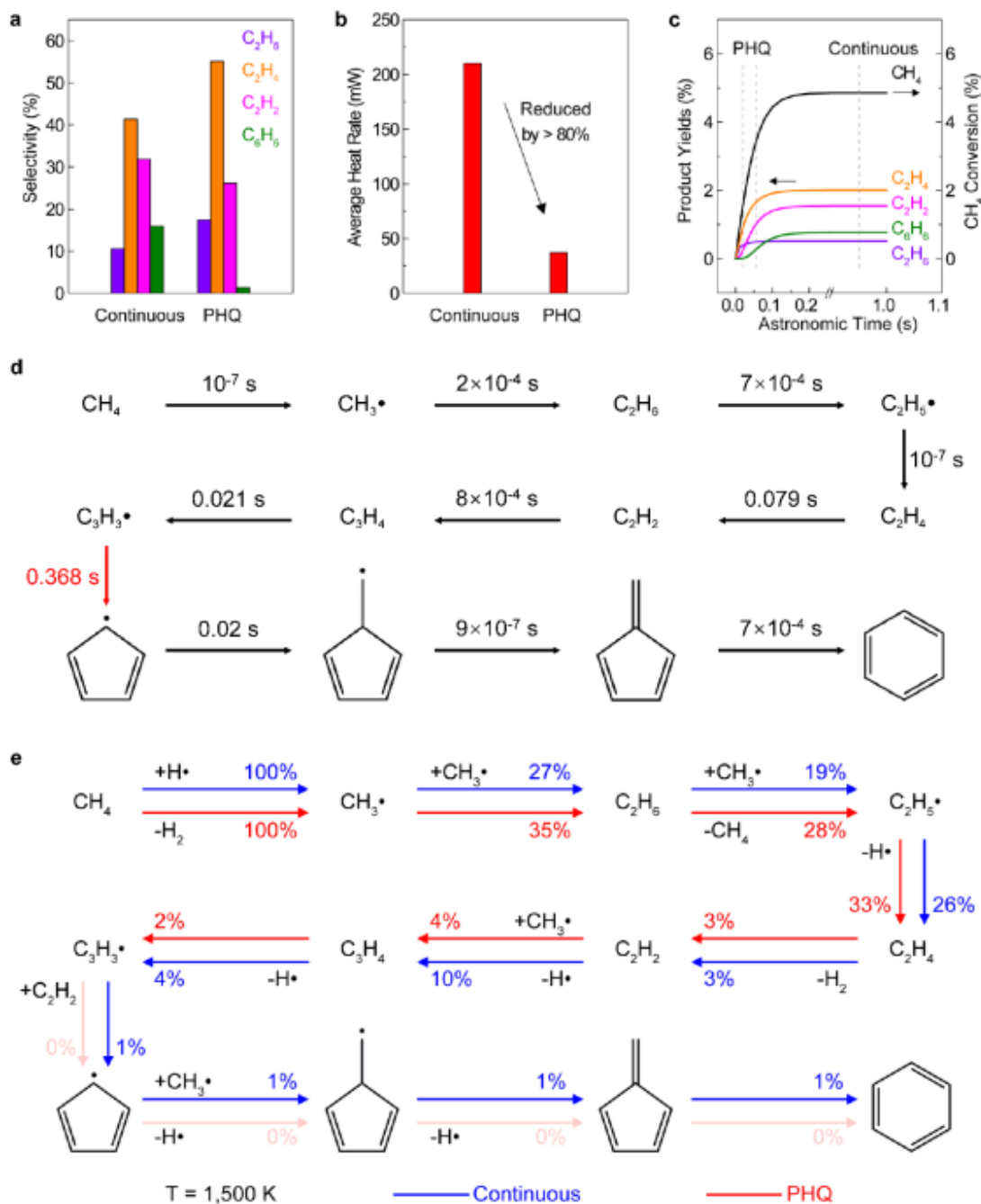


**Figure 5.11.** Modeling of  $CH_4$  pyrolysis reactions under continuous heating and PHQ. Comparison of the (a) product distribution and (b) energy required by the  $CH_4$  pyrolysis reaction between steady-state (simulating continuous heating) and transient (simulating PHQ) operations at an identical  $CH_4$  conversion of 5%. (c)  $CH_4$  conversion and product distribution as a function of astronomic time (i.e., clock time or external time of the system) under isothermal conditions at 1,500 K. (d) Characteristic timescales for each elementary step in the reaction path of  $CH_4$  pyrolysis toward aromatics formation, simulated at 1,500 K. The side species are omitted for clarity. The timescale for the slowest step ( $\tau_{cyclization} = 0.368 s$ ) along this reaction path is indicated in red. (e) Reaction pathway analysis for  $CH_4$  pyrolysis by steady-state (blue) and transient (red)

operations under isothermal conditions at 1,500 K. The percentages, next to each elementary step, correspond to the net reaction rates normalized by the net reaction rate of the initial dehydrogenation (initial CH<sub>4</sub> activation step) from CH<sub>4</sub> to CH<sub>3</sub><sup>•</sup>. For PHQ, the secondary and subsequent reactions after the propargyl radical (C<sub>3</sub>H<sub>3</sub><sup>•</sup>) are quenched (the shaded arrows), therefore yielding more C<sub>2</sub> products.

#### 5.4 Conclusion of chapter 5

In this chapter, we demonstrate the PHQ thermochemical synthesis technique using the methane pyrolysis reaction as proof of concept. The process, without using metal-based catalysts, enables a high selectivity to value-added C<sub>2</sub> products. Our study opens up a new model for implementing a range of industrially important thermochemical processes. In general, the high temperature in the PHQ technique enables fast activation of reactants for high rates and conversions, and the precise control over the heating process leads to high selectivity of desired products. Although the quenching process is not actively controlled, tuning the electric current can potentially create complex and sculpted temperature patterns (for example, square wave, triangle wave, stepped heating and cooling, and so on) to accurately manipulate the reaction pathways.

Scaling up the PHQ reactor relies on increasing the size of the carbon heater, which needs to be porous to allow gas molecules to diffuse throughout the structure, and — at the same time — possess a low total heat capacity for rapid heating and cooling. Commercial materials such as carbon felt and carbon foam can be used. Specially designed and synthesized carbon materials are also promising candidates. For example, the carbon heater can be highly porous three-dimensional structures and assembled to arrays for large-scale operations. Driven by electrical energy, our

technique may also enable process intensification and distributed chemical manufacturing with improved efficiency.

## Chapter 6: Conclusions and Future Works

### 6.5 *Conclusions*

The aim of my work is driven by a desire to innovate and develop cutting-edge technology to supersede the existing, commercially prevalent, indirect methods of methane upgrading. These conventional methods are not only energy-intensive but also contribute to significant CO<sub>2</sub> emissions. As a more economically viable alternative, the Direct Non-Oxidative Methane Conversion pathway stands out. However, it's not without its challenges, including thermodynamic stability, low selectivity, catalyst deactivation, and kinetic hindrance. Addressing these issues calls for breakthroughs in both catalyst development and reactor engineering for the NMC reaction. Our goal is to devise solutions that enhance the efficiency and effectiveness of methane conversion while optimizing the selectivity towards desired hydrocarbon products. We are striving to create a transformative shift in methane upgrading technology, making it not only more environmentally friendly, but also more economically and operationally advantageous.

The primary objectives of my work are as follows: Firstly, we aim to develop a new autothermal catalytic wall reactor system for NMC reactions. This system, featuring a sharpened axial temperature profile, will enable swift methane activations and controlled gas phase reactions. Secondly, we intend to utilize a bespoke SpaciMS system to analyze the performance of this autothermal catalytic wall reactor employing an Fe/SiO<sub>2</sub> catalyst, to better understand the NMC reaction pathways. Thirdly, we propose the invention of an innovative electrified reactor system. This system, with programmable heating and quenching, will efficiently facilitate methane pyrolysis.

Lastly, we seek to understand the impact of hydrogen activation on direct non-oxidative methane conversion by using an  $\text{SrCe}_{0.8}\text{Zr}_{0.2}\text{O}_{3-\delta}$  perovskite membrane material in conjunction with the Fe/SiO<sub>2</sub> catalyst.

In Chapter 2, we report the impact of hydrogen activation by hydrogen-permeable  $\text{SrCe}_{0.8}\text{Zr}_{0.2}\text{O}_{3-\delta}$  (SCZO) perovskite oxide material on NMC over an iron/silica catalyst. The SCZO oxide has mixed ionic and electronic conductivity and is capable of H<sub>2</sub> activation into protons and electrons for H<sub>2</sub> permeation. In the fixed-bed reactor packed with a mixture of SCZO oxide and iron/silica catalyst, stable and high methane conversion and low coke selectivity in NMC was achieved by co-feeding of H<sub>2</sub> in methane stream. The characterizations show that SCZO activates H<sub>2</sub> to favor “soft coke” formation on the catalyst. The SCZO could absorb H<sub>2</sub> in-situ to lower its local concentration to mitigate the reverse reaction of NMC in the tested conditions. The co-existence of H<sub>2</sub> co-feed, SCZO oxide and NMC catalyst in the present study mimics the conditions of NMC in the H<sub>2</sub>-permeable SCZO membrane reactor. The findings in this work offer the mechanistic understanding of and guidance for the design of H<sub>2</sub>-permeable membrane reactors for NMC and other alkane dehydrogenation reactions.

NMC suffers from low methane conversion, low selectivity to larger hydrocarbons, and catalyst coking in conventional isothermal fixed-bed reactors. The endothermicity of methane activation requires high temperatures, but the higher reactivity of product hydrocarbons than methane leads to secondary and follow-on reactions and subsequent coke formation. In chapter 3, we report a catalytic wall reactor operated with sharp spatial temperature profiles and millisecond contact time to resolve

all these challenges. The engineered reactor, coated with NMC and combustion catalysts on opposite tube wall surfaces, enables millisecond activation of methane powered by the energy generated from catalytic combustion of fuel gas. Sharp temperature gradients controlled by combustion catalyst zoning, together with shorter contact time of reactant than products inhibit coke formation and catalyst deactivation. The spatially fast quenching of the reactions in the catalytic wall reactor leads to unprecedented NMC performance with high hydrocarbon selectivity/yield and negligible coke.

In chapter 4, we have adopted an innovative approach by developing a spatially resolved capillary-inlet mass spectroscopy system (SpaciMS) to study the NMC process in an autothermal catalytic wall reactor (ACWR), which has showed excellent and stable performance as well as tunable product selectivity. The reactor utilizes a dual catalyst system, with Pt/ $\gamma$ -Al<sub>2</sub>O<sub>3</sub> as the oxidation catalyst and Fe/SiO<sub>2</sub> as the NMC catalyst, applied to the external and internal surfaces of the reactor respectively. This configuration establishes a non-uniform temperature profile along the reactor, promoting the formation of light hydrocarbon products such as ethylene. The SpaciMS system provides detailed, spatially resolved data on the transient reaction dynamics, temperature evolution, intermediate formation, and removal. This study is the first to apply SpaciMS to NMC, offering insights into the reaction dynamics at extreme temperatures (900-1200 °C) and enhancing our understanding of the NMC process. The findings pave the way for the development of more efficient and economically viable chemical reactor systems for methane conversion.

In chapter 5, we present a non-equilibrium, continuous synthesis technique that uses pulsed heating and quenching (for example, 0.02 s on, 1.08 s off) using a programmable electric current to rapidly switch the reaction between high (for example, up to 2,400 K) and low temperatures. The rapid quenching ensures high selectivity as well as lowers the average temperature to reduce the energy cost. Using methane pyrolysis as a model reaction, our programmable heating and quenching technique leads to high selectivity to value-added C<sub>2</sub> products (>75% versus <35% by the conventional non-catalytic method and versus <60% by most conventional methods using optimized catalysts). Conventional thermochemical syntheses by continuous heating under near-equilibrium conditions face critical challenges in improving the synthesis rate, selectivity, catalyst stability and energy efficiency, owing to the lack of temporal control over the reaction temperature and time, and thus the reaction pathways. This study establishes a new model towards highly efficient non-equilibrium thermochemical synthesis.

## 6.6 Future work

### 6.6.1 Renewable and scalable ACWR for NMC reaction

The ACWR featuring millisecond contact time and sharp temperature profiles was developed for the first time, for self-sustaining NMC reaction with high hydrocarbon product selectivity and negligible coke formation. Following the promising results obtained from the benchtop-scale ACWR, an important next step is to design a renewable and scalable reactor for potential commercialization. Instead of

methane, renewable hydrogen will be used as the fuel, with the goal of reducing CO<sub>2</sub> emissions from the autothermal operations. We aim to investigate the effects of catalyst hydrogen combustion and the coupled NMC reaction. Moreover, we have designed a multi-tubular ACWR for the NMC reaction with increased catalytic surface area to enhance product throughput.

#### 6.6.2 Assembly of electrical catalytic monolith reactor for NMC reaction

We have demonstrated the electrified PHQ (Pulsed Heating Quenching) thermochemical synthesis technique using the CH<sub>4</sub> pyrolysis reaction as a proof of concept. This enables a high selectivity to value-added C<sub>2</sub> products without the use of metal-based catalysts. Our study presents a novel model for implementing a range of industrially significant thermochemical processes. However, I hypothesize that the performance of this technique in the NMC reaction can be further improved by optimizing heating distributions and using catalysts to lower the energy barrier.

To enhance the technique, our plan involves fabricating an electric catalytic monolith reactor for the NMC reaction with the aim of boosting reaction performance and energy efficiency. Initially, we will design and fabricate the electrically conductive monolith based on findings from existing literature and modeling tools. Following this, PHQ tests will be conducted to analyze temperature profiles and help in constructing a suitable prototype. Secondly, we plan to disperse catalysts onto the monolith and study both the morphology of the catalyst and the catalytic test using conventional heating and reactor design. This step will aid in pre-screening different catalysts and establishing baselines for PHQ reaction performance tests. Next, we will conduct an NMC reaction using the electric catalytic monolith reactor to assess reactor

performance, catalyst morphology, and stability. We will also evaluate the effects of various reaction parameters, such as flow rate, catalyst loading, and heating program, on methane conversion and product selectivity. Lastly, we will establish a reproducible fabrication process to ensure the consistency of this novel type of reactor.

### *6.6.3 Fabrication of electrified membrane reactor model for chemical synthesis*

Catalytic membrane reactors have demonstrated exceptional performance in enhancing reaction conversion. This is achieved by adhering to Le Chatelier's principle, which involves removing products from the reaction. However, conventional membrane reactors are heated by external sources, leading to limitations due to thermal boundary layers from the reactor walls and membrane. This often results in poor catalyst utilization and energy efficiency.

We hypothesize that an electrifiable membrane can significantly enhance heat utilization and reaction performance. This would be achieved by serving as both a heating source and a separator within the membrane reactor, thereby eliminating the heat boundary layers. I have developed a method for synthesizing hydrogen-permeable carbon molecular sieve hollow fiber membranes with enhanced electrical conductivity. Procedures have also been established for the fabrication and assembly of these hollow fiber membranes for gas permeation tests. We continue to refine the synthesis procedure to obtain correlations between synthesis parameters and permeation results. Subsequently, we will synthesize a suitable catalyst for the NMC reaction and integrate it with the hollow fiber membrane. This will enable the creation of a novel electrified hollow fiber membrane reactor for NMC reaction tests. We will assess the NMC reaction performance of the reactor to determine catalyst activity, product selectivity,

and system stability. Finally, we will investigate the impact of gas flows and catalyst loading methods on the methane reaction rate and product selectivity.

## Bibliography

1. Zavyalova, U., Holena, M., Schlögl, R. & Baerns, M. Statistical analysis of past catalytic data on oxidative methane coupling for new insights into the composition of high - performance catalysts. *ChemCatChem* **3**, 1935-1947 (2011).
2. Calkins, W. H. & Bonifaz, C. Coal flash pyrolysis: 5. Pyrolysis in an atmosphere of methane. *Fuel* **63**, 1716-1719 (1984).
3. Hao, J. *et al.* Enhanced methane conversion to olefins and aromatics by h-donor molecules under nonoxidative condition. *ACS Catalysis* **9**, 9045-9050 (2019).
4. Sakbodin, M., Wu, Y., Oh, S. C., Wachsman, E. D. & Liu, D. Hydrogen-permeable tubular membrane reactor: Promoting conversion and product selectivity for non-oxidative activation of methane over an Fe@SiO<sub>2</sub> catalyst. *Angewandte Chemie International Edition* **55**, 16149-16152 (2016).
5. Šot, P. *et al.* Non - oxidative methane coupling over silica versus silica - supported iron (ii) single sites. *Chemistry - A European Journal* **26**, 8012-8016 (2020).
6. Wu, Y. *et al.* Overgrowth of lamellar silicalite-1 on mfi and bea zeolites and its consequences on non-oxidative methane aromatization reaction. *Microporous and Mesoporous Materials* **263**, 1-10 (2018).
7. Liu, L. *et al.* Methane dehydroaromatization on mo/hmcm-22 catalysts: Effect of sio<sub>2</sub>/al<sub>2</sub>o<sub>3</sub> ratio of hmcm-22 zeolite supports. *Catalysis letters* **108**, 25-30 (2006).
8. Bajec, D., Kostyniuk, A., Pohar, A. & Likozar, B. Micro-kinetics of non-oxidative methane coupling to ethylene over pt/ceo<sub>2</sub> catalyst. *Chemical Engineering Journal* **396**, 125182 (2020).
9. Xie, P. *et al.* Nanoceria-supported single-atom platinum catalysts for direct methane conversion. *Acs Catalysis* **8**, 4044-4048 (2018).
10. Xiao, Y. & Varma, A. Highly selective nonoxidative coupling of methane over pt-bi bimetallic catalysts. *ACS Catalysis* **8**, 2735-2740 (2018).
11. Berman, N. How does the u.S. Government use the strategic petroleum reserve? *Council on Foreign Relations* (2023).
12. Ha, L. T. Dynamic interlinkages between the crude oil and gold and stock during russia-ukraine war: Evidence from an extended tvp-var analysis. *Environmental Science and Pollution Research* **30**, 23110-23123 (2023).
13. Al-Aboosi, F. Y., El-Halwagi, M. M., Moore, M. & Nielsen, R. B. Renewable ammonia as an alternative fuel for the shipping industry. *Current Opinion in Chemical Engineering* **31**, 100670 (2021).
14. Atilhan, S. *et al.* Green hydrogen as an alternative fuel for the shipping industry. *Current Opinion in Chemical Engineering* **31**, 100668 (2021).
15. Lunsford, J. H. Catalytic conversion of methane to more useful chemicals and fuels: A challenge for the 21st century. *Catalysis Today* **63**, 165-174 (2000).
16. Use of natural gas. (U.S. Energy Information Administration, 2023).
17. Qun, L. *et al.* Progress and prospects of horizontal well fracturing technology for shale oil and gas reservoirs. *Petroleum Exploration and Development* **49**, 191-199 (2022).

18. Bank, T. W. Global gas flaring reduction partnership. *The World Bank Group* (2023).
19. Tollefson, J. Air sampling reveals high emissions from gas field. *Nature* **482**, 139-140 (2012).
20. Skytruth. (Earth Observation Group, 2023).
21. Horn, R. & Schlögl, R. Methane activation by heterogeneous catalysis. *Catalysis Letters* **145**, 23-39 (2015).
22. Ravi, M., Ranocchiari, M. & van Bokhoven, J. A. The direct catalytic oxidation of methane to methanol—a critical assessment. *Angewandte Chemie International Edition* **56**, 16464-16483 (2017).
23. Ren, T., Patel, M. K. & Blok, K. Steam cracking and methane to olefins: Energy use, co2 emissions and production costs. *Energy* **33**, 817-833 (2008).
24. Ge, X., Yang, L., Sheets, J. P., Yu, Z. & Li, Y. Biological conversion of methane to liquid fuels: Status and opportunities. *Biotechnology advances* **32**, 1460-1475 (2014).
25. Yuan, S. *et al.* Conversion of methane into liquid fuels—bridging thermal catalysis with electrocatalysis. *Advanced Energy Materials* **10**, 2002154 (2020).
26. Xu, L. T. & Dunning Jr, T. H. Orbital hybridization in modern valence bond wave functions: Methane, ethylene, and acetylene. *The Journal of Physical Chemistry A* **124**, 204-214 (2019).
27. Sousa-Aguiar, E. F., Noronha, F. B. & Faro Jr, A. The main catalytic challenges in gtl (gas-to-liquids) processes. *Catalysis Science & Technology* **1**, 698-713 (2011).
28. Khodakov, A. Y., Chu, W. & Fongarland, P. Advances in the development of novel cobalt fischer– tropesch catalysts for synthesis of long-chain hydrocarbons and clean fuels. *Chemical Reviews* **107**, 1692-1744 (2007).
29. Galadima, A. & Muraza, O. Revisiting the oxidative coupling of methane to ethylene in the golden period of shale gas: A review. *Journal of Industrial and Engineering Chemistry* **37**, 1-13 (2016).
30. Alvarez-Galvan, M. *et al.* Direct methane conversion routes to chemicals and fuels. *Catalysis today* **171**, 15-23 (2011).
31. Ismagilov, Z. R., Matus, E. V. & Tsikoza, L. T. Direct conversion of methane on mo/zsm-5 catalysts to produce benzene and hydrogen: Achievements and perspectives. *Energy & Environmental Science* **1**, 526-541 (2008).
32. York, A. P., Xiao, T. & Green, M. L. Brief overview of the partial oxidation of methane to synthesis gas. *Topics in Catalysis* **22**, 345-358 (2003).
33. Zhang, H., Sun, Z. & Hu, Y. H. Steam reforming of methane: Current states of catalyst design and process upgrading. *Renewable and Sustainable Energy Reviews* **149**, 111330 (2021).
34. Usman, M., Daud, W. W. & Abbas, H. F. Dry reforming of methane: Influence of process parameters—a review. *Renewable and Sustainable Energy Reviews* **45**, 710-744 (2015).
35. Yusuf, M., Bazli, L. & Abdullah, B. in *Artificial intelligence for renewable energy systems* 243-257 (Elsevier, 2022).

36. Sá, S., Silva, H., Brandão, L., Sousa, J. M. & Mendes, A. Catalysts for methanol steam reforming—a review. *Applied Catalysis B: Environmental* **99**, 43-57 (2010).
37. Huang, J., Ma, R., Huang, T., Zhang, A. & Huang, W. Carbon dioxide reforming of methane over ni/mo/sba-15-la<sub>2</sub>o<sub>3</sub> catalyst: Its characterization and catalytic performance. *Journal of Natural Gas Chemistry* **20**, 465-470 (2011).
38. Yu, M. *et al.* Carbon dioxide reforming of methane over promoted nixmg<sub>1-x</sub>o (1 1 1) platelet catalyst derived from solvothermal synthesis. *Applied Catalysis B: Environmental* **148**, 177-190 (2014).
39. Zhang, R.-J. *et al.* Effect of support on the performance of ni-based catalyst in methane dry reforming. *Journal of Fuel Chemistry and Technology* **43**, 1359-1365 (2015).
40. Aramouni, N. A. K., Touma, J. G., Tarboush, B. A., Zeaiter, J. & Ahmad, M. N. Catalyst design for dry reforming of methane: Analysis review. *Renewable and Sustainable Energy Reviews* **82**, 2570-2585 (2018).
41. Keller, G. & Bhasin, M. Synthesis of ethylene via oxidative coupling of methane: I. Determination of active catalysts. *Journal of Catalysis* **73**, 9-19 (1982).
42. Xu, Y., Bao, X. & Lin, L. Direct conversion of methane under nonoxidative conditions. *Journal of Catalysis* **216**, 386-395 (2003).
43. Wang, D., Lunsford, J. H. & Rosynek, M. P. Characterization of a mo/zsm-5 catalyst for the conversion of methane to benzene. *Journal of Catalysis* **169**, 347-358 (1997).
44. Weckhuysen, B. M., Wang, D., Rosynek, M. P. & Lunsford, J. H. Conversion of methane to benzene over transition metal ion zsm-5 zeolites: I. Catalytic characterization. *Journal of catalysis* **175**, 338-346 (1998).
45. Borry, R. W., Kim, Y. H., Huffsmith, A., Reimer, J. A. & Iglesia, E. Structure and density of mo and acid sites in mo-exchanged h-zsm5 catalysts for nonoxidative methane conversion. *The Journal of Physical Chemistry B* **103**, 5787-5796 (1999).
46. Kosinov, N. *et al.* Confined carbon mediating dehydroaromatization of methane over mo/zsm - 5. *Angewandte Chemie International Edition* **57**, 1016-1020 (2018).
47. Postma, R. S. & Lefferts, L. Influence of axial temperature profiles on fe/sio<sub>2</sub> catalyzed non-oxidative coupling of methane. *ChemCatChem* (2020).
48. Guo, X. *et al.* Direct, nonoxidative conversion of methane to ethylene, aromatics, and hydrogen. *Science* **344**, 616-619 (2014).
49. Oh, S. C. *et al.* Direct non - oxidative methane conversion in a millisecond catalytic wall reactor. *Angewandte Chemie International Edition* **58**, 7083-7086 (2019).
50. Lee, J. S. & Oyama, S. Oxidative coupling of methane to higher hydrocarbons. *Catalysis Reviews Science and Engineering* **30**, 249-280 (1988).
51. Vatani, A., Jabbari, E., Askarieh, M. & Torangi, M. A. Kinetic modeling of oxidative coupling of methane over li/mgo catalyst by genetic algorithm. *Journal of Natural Gas Science and Engineering* **20**, 347-356 (2014).
52. Tiemersma, T., Tuinier, M., Gallucci, F., Kuipers, J. & van Sint Annaland, M. A kinetics study for the oxidative coupling of methane on a mn/na<sub>2</sub>wo<sub>4</sub>/sio<sub>2</sub> catalyst. *Applied Catalysis A: General* **433**, 96-108 (2012).

53. Radaelli, G. Low-energy, low-cost production of ethylene by low temperature oxidative coupling of methane. (U.S. Department of Energy Office of Scientific and Technical Information, 2018).
54. Iliuta, M. C., Grandjean, B. P. A. & Larachi, F. Methane nonoxidative aromatization over ru-mo/hzsm-5 at temperatures up to 973 k in a palladium-silver/stainless steel membrane reactor. *Industrial & Engineering Chemistry Research* **42**, 323-330 (2003).
55. Abedin, M. A., Kanitkar, S., Bhattar, S. & Spivey, J. J. Promotional effect of cr in sulfated zirconia-based mo catalyst for methane dehydroaromatization. *Energy Technol-Ger* (2019).
56. Kosinov, N. *et al.* Methane dehydroaromatization by mo/hzsm-5: Mono-or bifunctional catalysis? *Acs Catalysis* **7**, 520-529 (2017).
57. Shu, Y., Ma, D., Xu, L., Xu, Y. & Bao, X. Methane dehydro - aromatization over mo/mcm - 22 catalysts: A highly selective catalyst for the formation of benzene. *Catalysis Letters* **70**, 67-73 (2000).
58. Ma, D. *et al.* Carbonaceous deposition on mo/hmcm-22 catalysts for methane aromatization: A tp technique investigation. *Journal of Catalysis* **208**, 260-269 (2002).
59. Liu, Z. *et al.* Direct non-oxidative methane coupling on vitreous silica supported iron catalysts. *Catalysis Today* **416**, 113873 (2023).
60. Zhang, T. Recent advances in heterogeneous catalysis for the nonoxidative conversion of methane. *Chemical Science* **12**, 12529-12545 (2021).
61. Wu, S., Wang, L. & Zhang, J. Photocatalytic non-oxidative coupling of methane: Recent progress and future. *Journal of Photochemistry and Photobiology C: Photochemistry Reviews* **46**, 100400 (2021).
62. Yuliati, L., Hattori, T., Itoh, H. & Yoshida, H. Photocatalytic nonoxidative coupling of methane on gallium oxide and silica-supported gallium oxide. *Journal of Catalysis* **257**, 396-402 (2008).
63. Kato, Y., Matsushita, N., Yoshida, H. & Hattori, T. Highly active silica-alumina-titania catalyst for photoinduced non-oxidative methane coupling. *Catalysis Communications* **3**, 99-103 (2002).
64. Li, L. *et al.* Efficient sunlight - driven dehydrogenative coupling of methane to ethane over a zn+ - modified zeolite. *Angewandte Chemie International Edition* **50**, 8299-8303 (2011).
65. Kolios, G. & Eigenberger, G. Styrene synthesis in a reverse-flow reactor. *Chemical engineering science* **54**, 2637-2646 (1999).
66. Kolios, G., Frauhammer, J. & Eigenberger, G. Autothermal fixed-bed reactor concepts. *Chemical Engineering Science* **55**, 5945-5967 (2000).
67. Sakbodin, M. *et al.* Direct nonoxidative methane conversion in an autothermal hydrogen-permeable membrane reactor. *Advanced Energy Materials* **11**, 2102782 (2021).
68. Wismann, S. T. *et al.* Electrified methane reforming: A compact approach to greener industrial hydrogen production. *Science* **364**, 756-759 (2019).
69. Seyyedmajid Sharifvaghefi, Y. Z. Microwave vs conventional heating in hydrogen production via catalytic dry reforming of methane. *Resources Chemicals and Materials* **1**, 290-307 (2022).

70. Spivey, J. J. & Hutchings, G. Catalytic aromatization of methane. *Chemical Society Reviews* **43**, 792-803 (2014).
71. Liu, Y. *et al.* Unravelling the enigma of nonoxidative conversion of methane on iron single-atom catalysts. *Angew Chem Int Ed Engl* **59**, 18586-18590 (2020).
72. Li, L., Borry, R. W. & Iglesia, E. Design and optimization of catalysts and membrane reactors for the non-oxidative conversion of methane. *Chemical Engineering Science* **57**, 4595-4604 (2002).
73. Morejudo, S. H. *et al.* Direct conversion of methane to aromatics in a catalytic co-ionic membrane reactor. *Science* **353**, 563-566 (2016).
74. Wang, L. *et al.* Dehydrogenation and aromatization of methane under non-oxidizing conditions. *Catalysis Letters* **21**, 35-41 (1993).
75. Natesakhawat, S. *et al.* Improved benzene production from methane dehydroaromatization over mo/hzsm-5 catalysts via hydrogen-permselective palladium membrane reactors. *Catalysis Science & Technology* **5**, 5023-5036 (2015).
76. Hamakawa, S., Li, L., Li, A. & Iglesia, E. Synthesis and hydrogen permeation properties of membranes based on dense srce0.95yb0.05o3- $\alpha$  thin films. *Solid State Ionics* **148**, 71-81 (2002).
77. Liu, Z., Li, L. & Iglesia, E. Catalytic pyrolysis of methane on mo/h-zsm5 with continuous hydrogen removal by permeation through dense oxide films. *Catalysis letters* **82**, 175-180 (2002).
78. Sakbodin, M. *et al.* Dual utilization of greenhouse gases to produce c2+ hydrocarbons and syngas in a hydrogen-permeable membrane reactor. *Journal of Membrane Science* **595**, 117557 (2020).
79. Sakbodin, M., Wu, Y., Oh, S. C., Wachsmann, E. D. & Liu, D. Hydrogen - permeable tubular membrane reactor: Promoting conversion and product selectivity for non - oxidative activation of methane over an fe<sup>0</sup> sio<sub>2</sub> catalyst. *Angewandte Chemie* **128**, 16383-16386 (2016).
80. Liu, Z., Nutt, M. A. & Iglesia, E. The effects of co<sub>2</sub>, co and h<sub>2</sub> co-reactants on methane reactions catalyzed by mo/h-zsm-5. *Catalysis letters* **81**, 271-279 (2002).
81. Ma, H., Ohnishi, R. & Ichikawa, M. Highly stable performance of methane dehydroaromatization on mo/hzsm-5 catalyst with a small amount of h<sub>2</sub> addition into methane feed. *Catalysis letters* **89**, 143-146 (2003).
82. Osawa, T., Nakano, I. & Takayasu, O. Dehydrogenation of methane over mo/zsm-5. Effects of additives in the methane stream. *Catalysis letters* **86**, 57-62 (2003).
83. Kojima, R., Kikuchi, S., Ma, H., Bai, J. & Ichikawa, M. Promotion effects of pt and rh on catalytic performances of mo/hzsm-5 and mo/hmcm-22 in selective methane-to-benzene reaction. *Catalysis letters* **110**, 15-21 (2006).
84. Aritani, H., Shibasaki, H., Orihara, H. & Nakahira, A. Methane dehydroaromatization over mo-modified h-mfi for gas to liquid catalysts. *Journal of Environmental Sciences* **21**, 736-740 (2009).
85. Ma, H., Kojima, R., Kikuchi, S. & Ichikawa, M. Effective coke removal in methane to benzene (mtb) reaction on mo/hzsm-5 catalyst by h<sub>2</sub> and h<sub>2</sub> o co-addition to methane. *Catalysis letters* **104**, 63-66 (2005).

86. Kreuer, K.-D. Proton-conducting oxides. *Annual Review of Materials Research* **33**, 333-359 (2003).
87. Phair, J. & Badwal, S. Review of proton conductors for hydrogen separation. *Ionics* **12**, 103-115 (2006).
88. Fabbri, E., Pergolesi, D. & Traversa, E. Materials challenges toward proton-conducting oxide fuel cells: A critical review. *Chemical Society Reviews* **39**, 4355-4369 (2010).
89. DeAngelis, M. T., Rondinone, A. J., Pawel, M. D., Labotka, T. C. & Anovitz, L. M. Sol-gel synthesis of nanocrystalline fayalite (Fe<sub>2</sub>SiO<sub>4</sub>). *American Mineralogist* **97**, 653-656 (2012).
90. Tang, C. *et al.* Surface heterogeneity of SiO<sub>2</sub> polymorphs: An XPS investigation of  $\alpha$ -quartz and  $\alpha$ -cristobalite. *The Journal of Physical Chemistry C* **118**, 26249-26257 (2014).
91. Zakaznova-Herzog, V. P. *et al.* High-resolution valence-band XPS spectra of the nonconductors quartz and olivine. *Physical Review B* **72**, 205113 (2005).
92. D. J. Miller, M. C. B. a. N. S. M. Interactions of CO<sub>2</sub> and CO at fractional atmosphere pressures with iron and iron oxide surfaces: One possible mechanism for surface contamination? *Surf. Interface Anal.* **33**, 299-305 (2002).
93. Dupin, J.-C., Gonbeau, D., Vinatier, P. & Levasseur, A. Systematic XPS studies of metal oxides, hydroxides and peroxides. *Physical Chemistry Chemical Physics* **2**, 1319-1324 (2000).
94. Wu, L. Q. *et al.* Method for estimating ionicities of oxides using O 1s photoelectron spectra. *AIP Advances* **5**, 097210 (2015).
95. Guo, X. *et al.* Direct, nonoxidative conversion of methane to ethylene, aromatics, and hydrogen. *Science* **344**, 616-619 (2014).
96. Toraman, H. E. *et al.* Ethylene production by direct conversion of methane over isolated single active centers. *Chemical Engineering Journal* **420**, 130493 (2021).
97. Olsvik, O. & Billaud, F. Modelling of the decomposition of methane at 1273 K in a plug flow reactor at low conversion. *Journal of analytical and applied pyrolysis* **25**, 395-405 (1993).
98. Olsvik, O. & Billaud, F. Thermal coupling of methane—a comparison between kinetic-model data and experimental-data. *Thermochimica Acta* **232**, 155-169 (1994).
99. Bare, S. R. *et al.* Characterization of coke on a Pt-Re/ $\gamma$ -Al<sub>2</sub>O<sub>3</sub> re-forming catalyst: Experimental and theoretical study. *ACS Catalysis* **7**, 1452-1461 (2017).
100. Espinat, D. *et al.* Characterization of the coke formed on reforming catalysts by laser Raman spectroscopy. *Applied Catalysis* **16**, 343-354 (1985).
101. Roeges, N. P. *Guide to the complete interpretation of infrared spectra of organic structures*. (Wiley, 1994).
102. Liu, H. M. *et al.* The chemical nature of carbonaceous deposits and their role in methane dehydro-aromatization on Mo/MCM-22 catalysts. *Appl Catal a-Gen* **236**, 263-280 (2002).
103. Song, Y., Xu, Y. B., Suzuki, Y., Nakagome, H. & Zhang, Z. G. A clue to exploration of the pathway of coke formation on Mo/HZSM-5 catalyst in the non-

- oxidative methane dehydroaromatization at 1073 k. *Appl Catal a-Gen* **482**, 387-396 (2014).
104. Abedin, M. A., Kanitkar, S., Bhattar, S. & Spivey, J. J. Sulfated hafnia as a support for mo oxide: A novel catalyst for methane dehydroaromatization. *Catalysis Today* (2019).
  105. Kanitkar, S., Abedin, M. A., Bhattar, S. & Spivey, J. J. Methane dehydroaromatization over molybdenum supported on sulfated zirconia catalysts. *Appl Catal a-Gen* **575**, 25-37 (2019).
  106. Gueret, C., Billaud, F., Fixari, B. & Leperchec, P. Thermal coupling of methane, experimental investigations on coke deposits. *Carbon* **33**, 159-170 (1995).
  107. Wang, S. *et al.* The pyrolysis of natural gas: A study of carbon deposition and the suitability of reactor materials. *Aiche J* **65**, 1035-1046 (2019).
  108. Vander Wal, R., Sengupta, A., Musselman, E. & Skoptsov, G. Microwave-driven plasma-mediated methane cracking: Product carbon characterization. *C-J Carbon Res* **4** (2018).
  109. Singh, M., Sengupta, A., Zeller, K., Skoptsov, G. & Vander Wal, R. L. Effect of hydrogen concentration on graphene synthesis using microwave-driven plasma-mediated methane cracking. *Carbon* **143**, 802-813 (2019).
  110. Budde, P. K., Singh, A. K. & Upadhyayula, S. Non-oxidative methane dehydroaromatization reaction over highly active  $\alpha$ -ZSM-5 derived from pretreatment. *Journal of Chemical Sciences* **130**, 1-16 (2018).
  111. Barr, T. L. & Seal, S. Nature of the use of adventitious carbon as a binding energy standard. *Journal of Vacuum Science & Technology A* **13**, 1239-1246 (1995).
  112. Dane, A., Demirok, U. K., Aydinli, A. & Suzer, S. X-ray photoelectron spectroscopic analysis of Si nanoclusters in SiO<sub>2</sub> matrix. *The Journal of Physical Chemistry B* **110**, 1137-1140 (2006).
  113. Reddy, B. M. *et al.* Raman and x-ray photoelectron spectroscopy study of CeO<sub>2</sub>-ZrO<sub>2</sub> and V<sub>2</sub>O<sub>5</sub>/CeO<sub>2</sub>-ZrO<sub>2</sub> catalysts. *Langmuir* **19**, 3025-3030 (2003).
  114. Silvestre-Albero, J., Rodríguez-Reinoso, F. & Sepúlveda-Escribano, A. Improved metal-support interaction in Pt/CeO<sub>2</sub>/SiO<sub>2</sub> catalysts after zinc addition. *Journal of Catalysis* **210**, 127-136 (2002).
  115. Burroughs, P., Hamnett, A., Orchard, A. F. & Thornton, G. Satellite structure in the x-ray photoelectron spectra of some binary and mixed oxides of lanthanum and cerium. *Journal of the Chemical Society, Dalton Transactions*, 1686-1698 (1976).
  116. Rayner Jr, G. B. *Spectroscopic investigation of local bonding in zirconium silicate high-k dielectric alloys for advanced microelectronic applications*. (North Carolina State University, 2002).
  117. Kosinov, N., Coumans, F. J., Uslamin, E., Kapteijn, F. & Hensen, E. J. Selective coke combustion by oxygen pulsing during Mo/ZSM-5 catalyzed methane dehydroaromatization. *Angewandte Chemie International Edition* **55**, 15086-15090 (2016).
  118. Kosinov, N. *et al.* Stable Mo/HZSM-5 methane dehydroaromatization catalysts optimized for high-temperature calcination-regeneration. *Journal of Catalysis* **346**, 125-133 (2017).

119. Kiani, D., Sourav, S., Tang, Y., Baltrusaitis, J. & Wachs, I. E. Methane activation by zsm-5-supported transition metal centers. *Chemical Society Reviews* **50**, 1251-1268 (2021).
120. Dean, A. M. Detailed kinetic modeling of autocatalysis in methane pyrolysis. *Journal of Physical Chemistry* **94**, 1432-1439 (1990).
121. Holmen, A., Olsvik, O. & Rokstad, O. Pyrolysis of natural gas: Chemistry and process concepts. *Fuel Processing Technology* **42**, 249-267 (1995).
122. Matheu, D. M., Dean, A. M., Grenda, J. M. & Green, W. H. Mechanism generation with integrated pressure dependence: A new model for methane pyrolysis. *The Journal of Physical Chemistry A* **107**, 8552-8565 (2003).
123. Olivos-Suarez, A. I. *et al.* Strategies for the direct catalytic valorization of methane using heterogeneous catalysis: Challenges and opportunities. *Acs Catalysis* **6**, 2965-2981 (2016).
124. Upham, D. C. *et al.* Catalytic molten metals for the direct conversion of methane to hydrogen and separable carbon. *Science* **358**, 917-921 (2017).
125. Sakbodin, M., Wachsman, E. D. & Liu, D. in *2019 North American Catalysis Society Meeting*. (NAM).
126. Brown, R. C. Process intensification through directly coupled autothermal operation of chemical reactors. *Joule* (2020).
127. Glöckler, B., Gritsch, A., Morillo, A., Kolios, G. & Eigenberger, G. Autothermal reactor concepts for endothermic fixed-bed reactions. *Chemical Engineering Research and Design* **82**, 148-159 (2004).
128. Razza, S. *et al.* Heat transfer performance of structured catalytic reactors packed with metal foam supports: Influence of wall coupling. *Catalysis Today* **273**, 187-195 (2016).
129. Han, S. J., Lee, S. W., Kim, H. W., Kim, S. K. & Kim, Y. T. Nonoxidative direct conversion of methane on silica-based iron catalysts: Effect of catalytic surface. *ACS Catalysis* **9**, 7984-7997 (2019).
130. Toraman, H. E. *et al.* Ethylene production by direct conversion of methane over isolated single active centers. *Chemical Engineering Journal*, 130493 (2021).
131. Venkataraman, K., Redenius, J. & Schmidt, L. Millisecond catalytic wall reactors: Dehydrogenation of ethane. *Chemical engineering science* **57**, 2335-2343 (2002).
132. Wanat, E., Venkataraman, K. & Schmidt, L. Steam reforming and water–gas shift of ethanol on rh and rh–ce catalysts in a catalytic wall reactor. *Applied Catalysis A: General* **276**, 155-162 (2004).
133. Venkataraman, K., Wanat, E. & Schmidt, L. Steam reforming of methane and water - gas shift in catalytic wall reactors. *AIChE Journal* **49**, 1277-1284 (2003).
134. Tonkovich, A. L. Y., Yang, B., Perry, S. T., Fitzgerald, S. P. & Wang, Y. From seconds to milliseconds to microseconds through tailored microchannel reactor design of a steam methane reformer. *Catalysis Today* **120**, 21-29 (2007).
135. Oh, S. C., Sakbodin, M. & Liu, D. in *Catalysis* 127-165 (2019).
136. Puente - Urbina, A. *et al.* Direct evidence on the mechanism of methane conversion under non - oxidative conditions over iron - modified silica: The

- role of propargyl radicals unveiled. *Angewandte Chemie* **133**, 24204-24209 (2021).
137. Reid, R. C., Prausnitz, J. M. & Poling, B. E. The properties of gases and liquids. (1987).
  138. Choudhary, V., Rajput, A. & Prabhakar, B. Low temperature oxidative conversion of methane to syngas over nio-cao catalyst. *Catalysis Letters* **15**, 363-370 (1992).
  139. Tsang, S., Claridge, J. & Green, M. Recent advances in the conversion of methane to synthesis gas. *Catalysis today* **23**, 3-15 (1995).
  140. Huang, K., Miller, J. B., Huber, G. W., Dumesic, J. A. & Maravelias, C. T. A general framework for the evaluation of direct nonoxidative methane conversion strategies. *Joule* **2**, 349-365 (2018).
  141. Kosinov, N. *et al.* Reversible nature of coke formation on mo/zsm - 5 methane dehydroaromatization catalysts. *Angewandte Chemie* **131**, 7142-7146 (2019).
  142. Sakbodin, M., Schulman, E., Pan, Y., Wachsman, E. D. & Liu, D. Methane-to-aromatics in a gas recycle methane reactor/hydrogen membrane separator. *Catalysis Today* **365**, 80-87 (2021).
  143. Dong, Q. *et al.* Programmable heating and quenching for efficient thermochemical synthesis. *Nature* **605**, 470-476 (2022).
  144. Sá, J. *et al.* Spacims: Spatial and temporal operando resolution of reactions within catalytic monoliths. *Analyst* **135**, 2260-2272 (2010).
  145. Chorkendorff, I. & Niemantsverdriet, J. W. *Concepts of modern catalysis and kinetics*. (John Wiley & Sons, 2017).
  146. Marin, G. B., Yablonsky, G. S. & Constales, D. *Kinetics of chemical reactions: Decoding complexity*. (John Wiley & Sons, 2019).
  147. Bailey, J. Periodic operation of chemical reactors: A review. *Chemical Engineering Communications* **1**, 111-124 (1974).
  148. Kevrekidis, I. G., Schmidt, L. D. & Aris, R. Some common features of periodically forced reacting systems. *Chemical engineering science* **41**, 1263-1276 (1986).
  149. Papathanasiou, A. G., Wolff, J., Kevrekidis, I. G., Rotermund, H. H. & Ertl, G. Some twists and turns in the path of improving surface activity. *Chemical physics letters* **358**, 407-412 (2002).
  150. Yao, Y. *et al.* Carbothermal shock synthesis of high-entropy-alloy nanoparticles. *Science* **359**, 1489-1494 (2018).
  151. Jacob, R. J., Kline, D. J. & Zachariah, M. R. High speed 2-dimensional temperature measurements of nanothermite composites: Probing thermal vs. Gas generation effects. *Journal of Applied Physics* **123** (2018).
  152. Mokhatab, S., Poe, W. A. & Mak, J. Y. *Handbook of natural gas transmission and processing: Principles and practices*. (Gulf professional publishing, 2018).
  153. Feizhou, Z. & Shanghe, L. A new function to represent the lightning return-stroke currents. *IEEE transactions on electromagnetic compatibility* **44**, 595-597 (2002).
  154. Bao, W. *et al.* Flexible, high temperature, planar lighting with large scale printable nanocarbon paper. *Advanced materials* **28**, 4684-4691 (2016).
  155. Van Geem, K. M., Galvita, V. V. & Marin, G. B. Making chemicals with electricity. *Science* **364**, 734-735 (2019).

156. Bai, Z., Chen, H., Li, B. & Li, W. Methane decomposition over ni loaded activated carbon for hydrogen production and the formation of filamentous carbon. *International journal of hydrogen energy* **32**, 32-37 (2007).
157. Gao, Z., Kobayashi, M., Wang, H., Onoe, K. & Yamaguchi, T. Methane conversion in thermal diffusion column reactor with carbon rod as pyrogen. *Fuel processing technology* **88**, 996-1001 (2007).
158. Hao, J. *et al.* Direct experimental detection of hydrogen radicals in non-oxidative methane catalytic reaction. *Journal of Energy Chemistry* **52**, 372-376 (2021).
159. Zhang, Y. *et al.* Promotional effects of in on non-oxidative methane transformation over mo-zsm-5. *Catalysis Letters* **146**, 1903-1909 (2016).
160. Aboul-Gheit, A. K., Awadallah, A. E., Aboul-Enein, A. A. & Mahmoud, A.-L. H. Molybdenum substitution by copper or zinc in h-zsm-5 zeolite for catalyzing the direct conversion of natural gas to petrochemicals under non-oxidative conditions. *Fuel* **90**, 3040-3046 (2011).
161. Frenklach, M. Reaction mechanism of soot formation in flames. *Physical chemistry chemical Physics* **4**, 2028-2037 (2002).
162. Yablonsky, G. S., Constales, D. & Marin, G. B. Equilibrium relationships for non-equilibrium chemical dependencies. *Chemical Engineering Science* **66**, 111-114 (2011).

## List of Publications

### Journals:

1. Qi Dong, Yonggang Yao, **Sichao Cheng** (co-first author); Konstantinos Alexopoulos, Jinlong Gao, Sanjana Srinivas, Yifan Wang, Yong Pei, Chaolun Zheng, Alexandra H. Brozena, Hao Zhao, Xizheng Wang, Hilal Ezgi Toraman, Bao Yang, Ioannis G. Kevrekidis, Yiguang Ju, Dionisios G. Vlachos, Dongxia Liu & Liangbing Hu. Programmable Heating and Quenching for Efficient Thermochemical Synthesis, **Nature**, 2022, 605, 470–476. doi: 10.1038/s41586-022-04568-6.
2. **Sichao Cheng** (first author), Su Cheun Oh, Mann Sakbodin, Limei Qiu, Yuxia Diao & Dongxia Liu. Understanding impact of hydrogen activation by SrCe<sub>0.8</sub>Zr<sub>0.2</sub>O<sub>3-δ</sub> perovskite membrane material on direct non-oxidative methane conversion. **Frontiers in Chemistry**, 2021, 9, 1119. doi: 10.3389/fchem.2021.806464.
3. **Sichao Cheng** (first author); Abhinav Malhotra, Zixiao Liu, Paul Albertus, Dionisios G. Vlachos & Dongxia Liu. Nonoxidative Methane Coupling in an Autothermal Millisecond Catalytic Wall Reactor. **Joule**, 2023. (Under revision)
4. Lu Liu, Antara Bhowmick, **Sichao Cheng** (co-first author), Borja Hernandez Blazquez, Ying Pan, Junyan Zhang, Yuan Zhang, Yuying Shu, Dat T. Tran, Yuqing Luo, Marianthi Ierapetritou, Chen Zhang & Dongxia Liu. Stable Alkane Dehydrogenation in Electrifiable Carbon Membrane Reactor. **Joule**, 2023. (Under revision)
5. **Sichao Cheng** (first author), Sashank Kasiraju, Rucha Railkar, Zixiao Liu, Dionisios G. Vlachos & Dongxia Liu. A spatially resolved analysis on selective nonoxidative coupling of methane in autothermal catalytic wall reactor. 2023. (Manuscript under preparation)
6. Qi Dong, Aditya Dilip Lele, Xinpeng Zhao, Shuke Li, **Sichao Cheng**, Yueqing Wang, Mingjin Cui, Miao Guo, Alexandra H. Brozena, Ying Lin, Tangyuan Li, Lin Xu, Aileen Qi, Ioannis G. Kevrekidis, Jianguo Mei, Xuejun Pan, Dongxia Liu, Yiguang Ju & Liangbing Hu Depolymerization of plastics by means of electrified spatiotemporal heating. **Nature**, 2023, 616, 488–494. doi:10.1038/s41586-023-05845-8.
7. Zixiao Liu, **Sichao Cheng**, Emily Schulman, Weiqi Chen, Dionisios G. Vlachos, Yuying Shu, Dat T. Tran & Dongxia Liu. Direct non-oxidative methane coupling on vitreous silica supported iron catalysts. **Catalysis Today**, 2023, 416, 113873. doi: 10.1016/j.cattod.2022.08.015.

8. Sampath Gunukula, Laleh Emdadi, Asher C. Leff, Sampath A. Karunaratne, **Sichao Cheng**, Wei Wu, Dongxia Liu & Dat T. Tran. Ex-situ catalytic fast pyrolysis of wood chips over lamellar MFI zeolite supported nickel catalyst. **Journal of Analytical and Applied Pyrolysis**, 2023, 169, 105821. doi: 10.1016/j.jaap.2022.105821.
9. Hilal Ezgi Toraman, Konstantinos Alexopoulos, Su Cheun Oh, **Sichao Cheng**, Dongxia Liu & Dionisios G. Vlachos. Ethylene Production by direct conversion of methane over isolated single active centers. **Chemical Engineering Journal**, 2021, 420, 3, 130493. doi: 10.1016/j.cej.2021.130493.
10. Junyan Zhang, Evan C. Wegener, Nohor River Samad, James W. Harris, Kinga A. Unocic, Lawrence F. Allard, Stephen Purdy, Shiba Adhikari, Michael J. Cordon, Jeffrey T. Miller, Theodore R. Krause, **Sichao Cheng**, Dongxia Liu, Meijun Li, Xiao Jiang, Zili Wu & Zhenglong Li. Isolated Metal Sites in Cu-Zn-Y/Beta for Direct and Selective Butene-Rich C<sub>3</sub>+ Olefin Formation from Ethanol. **ACS Catalysis**, 2021, 11, 15, 9885-9897. doi: 10.1021/acscatal.1c02177.
11. Wei Wu, Dat T. Tran, **Sichao Cheng**, Yuan Zhang, Na Li, Huiyong Chen, Ya-Huei (Cathy) Chin d, Libo Yao & Dongxia Liu. Local environment and catalytic property of Lewis acid sites in hierarchical lamellar titanium Silicalite-1 zeolites. **Microporous and Mesoporous Materials**, 2021, 311, 110710. doi: 10.1016/j.micromeso.2020.110710.
12. Mann Sakbodin, Emily Schulman, **Sichao Cheng**, Yi-Lin Huang, Ying Pan, Paul Albertus, Eric D. Wachsman & Dongxia Liu. Direct nonoxidative methane conversion in an autothermal hydrogen-permeable membrane reactor. **Advanced Energy Materials**, 2021, 11, 46, 2102782. doi: 10.1002/aenm.202102782.
13. Luther Mahoney, Laleh Emdadi, Asher C. Leff, Dat T. Tran, Wei Wu, **Sichao Cheng**, Dongxia Liu, Chi K. Nguyen, Ivan C. Lee. Influences of metal-modification and lamellar zeolite structure on ethylene to liquid aromatics conversion reaction using MFI catalysts. **Fuel**, 2019, 256, 115953. doi: 10.1016/j.fuel.2019.115953.

#### **Patents:**

1. Dongxia Liu, **Sichao Cheng**. "Self-sustaining Autothermal Millisecond Catalytic Wall Reactor and Methods of Nonoxidative Direct Methane Conversion," 63/373550 · Filed Aug 30, 2022.
2. Liangbing Hu; Dongxia Liu; **Sichao Cheng**; Dong Qi; Yiguang Ju; "Systems to Convert Synthetic Plastics, Natural Macromolecules, and Biomass to Value-added Chemicals via Spatiotemporal Heating," WO2023059622A1, Oct 2022.

### **Book Chapters:**

1. Su Cheun Oh, **Sichao Cheng**, Ying Pan, Emily Schulman, Dongxia Liu. Multifunctional reactors for direct Nonoxidative Methane Conversion. **Direct natural Gas Conversion to Value-Added Chemicals**, 2020, 305-330. ISBN: 9780429022852.

### **Presentations:**

1. **Sichao Cheng**, Dongxia Liu. "A Spatially Resolved Analysis on Selective Nonoxidative Coupling of Methane in an Autothermal Catalytic Wall Reactor." Spring Symposium, Catalysis Club of Philadelphia, Villanova, PA, June 2022
2. **Sichao Cheng**. "Self-sustaining Methane Upgrading Facility for Flaring Sites." ARPA-E Summit, Washington DC, May 2023
3. **Sichao Cheng**, Dongxia Liu. "Sharpening Spatial Temperature Profile of Catalytic Wall Reactor for Selective Nonoxidative Coupling of Methane." The 27th North American Catalysis Society, NY, May 2022.
4. **Sichao Cheng**, Su Cheun Oh, Dongxia Liu. "Understanding the impact of hydrogen activation by SrCe<sub>0.8</sub>Zr<sub>0.2</sub>O<sub>3-δ</sub> perovskite membrane material on direct non-oxidative methane conversion." The 27th North American Catalysis Society, NY, 2022.

### **Awards:**

1. The 2021 **Clark Doctoral Fellows Mid-Career Award** by A. James Clark School of engineering, an award given to engineer school graduate school students who has a record of high distinction in their academic studies and research as well as clear potential for continued excellence Engineering, recognizes his broadly impactful research.
2. The 2021 **Future Faculty Program**, a program by A. James Clark School of engineering, University of Maryland to prepare selected Clark School doctoral students to achieve career-long success in the academic world as teachers and researchers.
3. The 2020 & 2021 **Army Research Lab Journeyman Fellowship**, a fellowship designed to significantly increase the involvement of creative and highly trained scientists and engineers from academia and industry in scientific and technical areas of interest and relevance to the Army.